The interfacial reaction and analysis of W thin film on 6H-SiC annealed in vacuum, hydrogen and argon.

BY

THABSILE THEODORA THABETHE

Submitted in partial fulfilment of the requirements for the degree of

DOCTOR OF PHILOSOPHY (PhD) IN PHYSICS

In the Faculty of Natural and Agricultural Sciences

University of Pretoria

September 2017

Supervisor: Prof J.B. Malherbe

Co-Supervisor: Dr T.T. Hlatshwayo

Co-Supervisor: Dr E.G. Njoroge

DECLARATION

I, Thabsile Theodora Thabethe, declare that the thesis, which I hereby submit for the degree of Doctor of Philosophy in Physics at the University of Pretoria, is my own work and has not been previously submitted by me for a degree at this or any other tertiary institution.

Signature:

Date : 02/02/2018

Summary

SUMMARY

The Interfacial reaction and analysis of W thin film on 6H-SiC annealed in vacuum, hydrogen and argon.

BY

Thabsile Theodora Thabethe

Submitted in partial fulfilment of the requirements for the degree of (PhD) in Physics in the Faculty of Natural and Agricultural Science, University of Pretoria

Supervisor/Promoter: Prof. J. B. Malherbe

Co-Supervisor: Dr E. G. Njoroge

Co-Supervisor: Dr T. T. Hlatshwayo

Silicon carbide (SiC) is used as the main diffusion barrier to prevent the fission products (FPs) from escaping in high temperature reactors (HTRs). It retains most of the FPs quite effectively with the exception of silver, strontium and europium. There have also been reports on the reactions between some FPs and SiC, raising some concerns on the integrity of SiC as a coating layer and questioning the ability of SiC as the main diffusion barrier. An additional protective layer of tungsten (W) is proposed to cover the SiC and probably reduce the interaction of FPs with SiC. Coating of SiC layer with W will assist in improving the shielding effect, which will allow for high burn up and enrichment without degrading the SiC. W coatings on SiC are also used for device fabrication. (Thus this study will benefit both semiconductor and nuclear application.)

The study was conducted by sputter depositing W metal thin films on 6H-SiC at room temperature (RT). The effect of thermal annealing in vacuum, hydrogen (H_2) and argon (Ar) of the W thin film deposited on 6H-SiC was investigated as a function of annealing temperature. The resulting solid-state reactions, phase composition and surface structural modification were investigated using Rutherford backscattering spectrometry (RBS), grazing incidence X-ray diffraction (GIXRD), scanning electron microscopy (SEM) and atomic force microscopy (AFM). The thickness of the as-deposited layer obtained from RUMP simulations was about 73.8 nm and was composed of about 63.4 at.% W and 36.6 at.% O. The oxygen was in a form of tungsten oxide (WO_3) mixed in the W thin film. The SEM and AFM images of the as-deposited samples showed that the W thin film had a uniform surface with small grains. The surface roughness (R_{rms} value) of the as-deposited sample was 0.4 nm.

The samples where annealed from 700 °C to 1000 °C for 1h in vacuum, hydrogen (H_2), and argon (Ar). From the RBS results, the initial reaction for vacuum annealed samples occurred at 850 °C, for H_2 annealed samples it was 700 °C and the Ar annealed had an initial reaction at a temperature lower than 700 °C. In all the annealing atmospheres carbon (C) was found to diffuse faster than Si into the W metal. After this C diffusion reached equilibrium, Si also migrated into the W metal. A reduction of oxygen upon annealing was observed for the vacuum annealed samples. Removal of oxygen was observed for the H_2 annealed samples, while oxygen was seen to diffuse to the reaction zone (RZ) for the Ar annealed samples.

The phases observed from GIXRD at 700 °C for vacuum annealed samples were CW_3 and WC, for H_2 samples W_5Si_3 and WC and for Ar annealed samples W_5Si_3, WC, SiO_2 and W_2C. The formation of WSi_2 and W_2C was observed at 800 °C for H_2 samples and 900 °C for

vacuum samples. The segregation of Si towards the surface at 1000 °C for H_2 samples resulted in the formation of SiO_2. The results showed that annealing in different atmospheres reduces the initial reactions and phases formed.

SEM and AFM revealed that the samples annealed in Ar were rougher than the vacuum and H_2 samples, while the vacuum annealed samples were rougher than the H_2 annealed samples. The R_{rms} of the samples annealed in different atmosphere followed the order: Ar > Vacuum> H_2. From the SEM and AFM images, the H_2 annealed samples at 700 °C were composed of small granules which increased with annealing temperature resulting in the formation of distinct grain boundaries. The samples annealed in Ar at 700 °C were composed of big crystals which were randomly orientated. Increase in annealing temperature for the Ar samples resulted in the parasitic growth of the crystals, which is in line with Wulf's law. The samples annealed in vacuum at 700 °C formed tungsten oxide nanowires on the W metal surface, with the W metal in a form of granules. Annealing at high temperatures resulted in the removal of the tungsten oxide nanowires on the W metal surface and parasitic growth of the crystals. The difference in the crystal growth observed during the vacuum, H_2 and Ar is explained by a crystal growth model.

ACKNOWLEDGEMENTS

I will like to acknowledge the following people for their support and valuable contribution in the success of my study.

- My supervisor, Prof. J.B. Malherbe, my co-supervisor Dr. T.T. Hlatshwayo, and co-supervisor Dr. E.G. Njoroge and the head of the department Prof. C.C. Theron for their guidance, support, discussion during the course of this study.
- The late Dr N. van der Berg for the assistance with the scanning electron microcopy part of my research.
- Mr T. Ntsoane from NECSA for the assistance with XRD measurements and guidance.
- All the staff and fellow students in the Physics department, especially Dr Julien Danbegnon, Dr Damilola Momodu for all their help, encouragement and moral support. Most especially
- All my friends for the love and support.
- My family, mostly my mother- Thandiwe Thabethe, grandmother- Nomalungelo Thabethe, Katlego Thabethe, Ntando Shongwe, Ephraim Shongwe and Luyanda Thabethe-Momodu for their prayers, endless love, support and encouragement throughout my studies and life.

  Ngiyabonga boThabethe, mkholo lonsundu nyawo ezimhlophe. Bengingete ngafinyelela ngaphendle kwenu.
- The financial assistance of the NRF is hereby acknowledged. Opinions expressed and conclusions arrived at, are those of the author and not to be necessarily attributed to the NRF.
- Lastly God Almighty for giving me strength.

A special thank you to my lovely daughter Luyanda Amina Thabethe-Momodu for providing me with the strength and courage to finish my PhD. Mommy loves you very much baby. You and only you are the queen of my heart.

TABLE OF CONTENTS

ABBREVIATIONS

AFM	Atomic Force Microscopy
CM	Ceramic/Metal
FP	Fission Products
GIXRD	Grazing incident X-ray Diffraction
HTGR	High Temperature Gas Cooled Reactors
PBMR	Pebble Bed Modular Reactor
RZ	Reaction Zone
RBS	Rutherford Backscattering Spectrometry
RUMP	Rutherford Universal Manipulation Program
SEM	Scanning Electron Microscopy
TRISO	Tri-structural Isotropic
XRD	X-ray Diffraction

Chapter 1 : Introduction

1.1 High temperature gas cooled reactors

The shortage of electricity, constant decrease in fossil fuel supply and increase in energy demands around the world require alternative methods of electricity generation. One of these alternative methods is the use of high temperature gas cooled reactors (HTGRs) for generating electricity. In a nuclear reactor, a slow neutron (n) reacts with uranium (U^{235}) to form U^{236} which is unstable. The unstable U^{236} fissions to two fission products, three neutrons and release a lot of energy. Some of the neutrons formed will further reacts with the other U^{235} causing them to fission (forming more FPs, 3n and releasing more energy). Basically one fission will trigger others, which triggers more until there is a chain reaction. Rods are inserted amongst the tubes which are holding the uranium fuel to control the nuclear reaction. The control rods, inserted or withdrawn may slow down or accelerate the reaction [1]. Water separates fuel tubes in the reactor. The water is turned into steam by the heat produced via fission. The steam drives a turbine, which spins a generator to create the electricity.

The HTGRs, such as the pebble bed modular reactor (PBMR), uses coated fuel particles shown the schematic diagram in figure.1-1. Uranium oxide or uranium carbide kernels are used as nuclear fuels. The fuel kernel is a small spherical ball covered with four layers and is called the tristructural isotropic (TRISO) particle. The four layers are: low-density pyrolytic carbon i.e. the buffer layer, inner high-density pyrolytic carbon (IPyC), silicon carbide (SiC) and outer high-density pyrolytic carbon (OPyC), as illustrated in figure 1-1. The fuel kernel is 0.5 mm in diameter, the buffer layer is 95 μm thick, IPyC and OPyC are each 40 μm thick and the SiC is 35μm thick [2].

The low-density pyrolytic carbon buffer acts as voids for the gaseous fission products (FPs) and carbon monoxide produced and protect the IPyC from damage by reducing the fission recoils and accommodate the deformation of the fuel kernel during burn-up. The IPyC layer acts as a diffusion barrier for gaseous FPs. The laminar structures of the carbon sphere in both the buffer and IPyC layers also have stress and gas storage function [3]. The SiC layer is the main barrier for FPs release and the OPyC protects the SiC mechanically.

Most of the HTGR operates at a temperature of about 950 °C [4][5]. Under this normal operation conditions of the reactor, SiC is a reliable diffusion barrier for most of the FPs. The release of some key FPs (silver (Ag), europium (Eu) and strontium (Sr)) and the reaction of SiC with other FPs during reactor operating [6][7], raised some concerns on the integrity of SiC as a coating layer [8][9] and the ability of SiC to act as the main diffusion barrier. Reports have shown that the interaction of palladium (Pd) with SiC enhances the migration of silver [10]–[13]. The interaction between high yield FP such as zirconium (Zr) and SiC has also been reported [14][15]. Due to these problems a solution to stop the migration of FPs, and reaction of FPs with the SiC has to be investigated. Tungsten is suggested as a solution to assist SiC as a diffusion barrier for the TRISO particle.

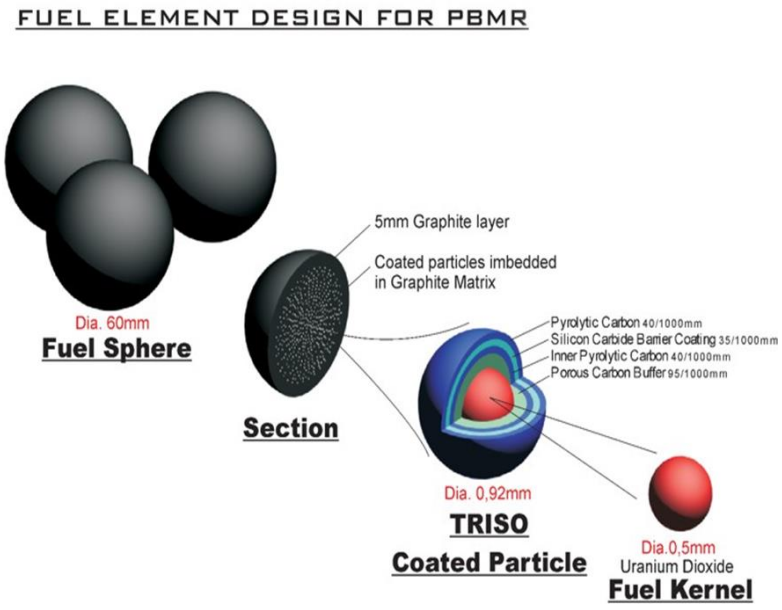

Figure 1-1: *The schematic diagram of the fuel for a Pebble Bed Modular Reactor (PBMR) taken from [2].*

1.2 Silicon Carbide

SiC is a binary compound with the same number of Si and C atoms. The structural unit of SiC is considered to be covalently bonded, with an ionic contribution of about 12%, due to the difference in valency of Si (positively charged) and C (negatively charged), making the Si and C bonds to be nearly pure covalent. The basic structural unit of SiC is a tetrahedron, and is either SiC_4 or CSi_4 as shown in figure 1-2.

SiC has chemical and physical properties like: extreme hardness, high thermal conductivity, small neutron capture cross-sections, high temperature stability, radiation resistance, etc. [16]–[18]. It is a wide-bandgap semiconductor 2.4-3.4 eV [19] that has a good potential for electronic and optoelectronic applications in advance devices such as LEDs, lasers, microwave power, etc. [20]. It has a Mohs hardness of 9.5 making it one of the hardest

naturally occurring material known. The bond length between Si and C atom is 1.89 Å which results in excellent hardness and high bond strength [21]. SiC is a good abrasive with high corrosion resistance and it has high thermal conductivity allowing for high operation temperatures. It also has good dimensional stability (its ability to be able to maintain or keep its shape over a long period of time, and also under specific conditions) under neutron radiation. The sublimation temperature of SiC is around 2800 °C and decomposes at temperatures above 1600 °C [22]–[24].

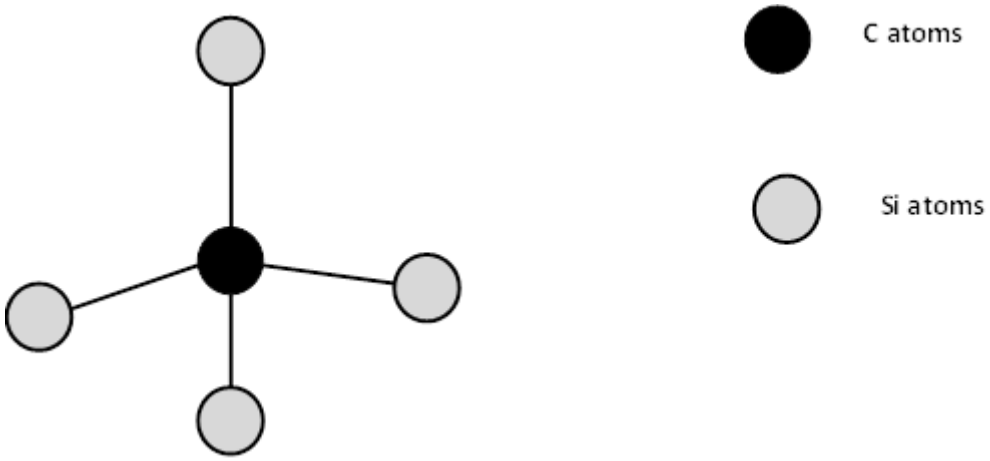

Figure 1-2: *Tetrahedral silicon carbide structure.*

SiC comes in a different number of crystal structures, called polytypes. All the polytypes of SiC chemically consist of 50% of C atoms and 50% of Si covalently bonded. SiC has more than 200 polytypes which have been identified [19][25]. All the polytypes have different electrical properties [26]. The most common polytypes of SiC are the cubic 3C-SiC, hexagonal 4H-SiC, 6H-SiC, and rhombohedral 15R-SiC (shown in figure 1-3). The difference in polytypes is characterized by the stacking sequence of the bi-atom layers of the SiC structure.

Figure 1-2 shows SiC layer structure with the tetrahedrally bonded carbon atom connected to three Si atoms within the double layer and having a single bond connected to a Si atom in the layer below. A hexagonal structure is formed if one considers the location of the carbon atom within a bilayer labelled “A” in figure 1-4. The following layer can position the carbon atom in B or C lattice site. This stacking sequence determines the material polytype of SiC.

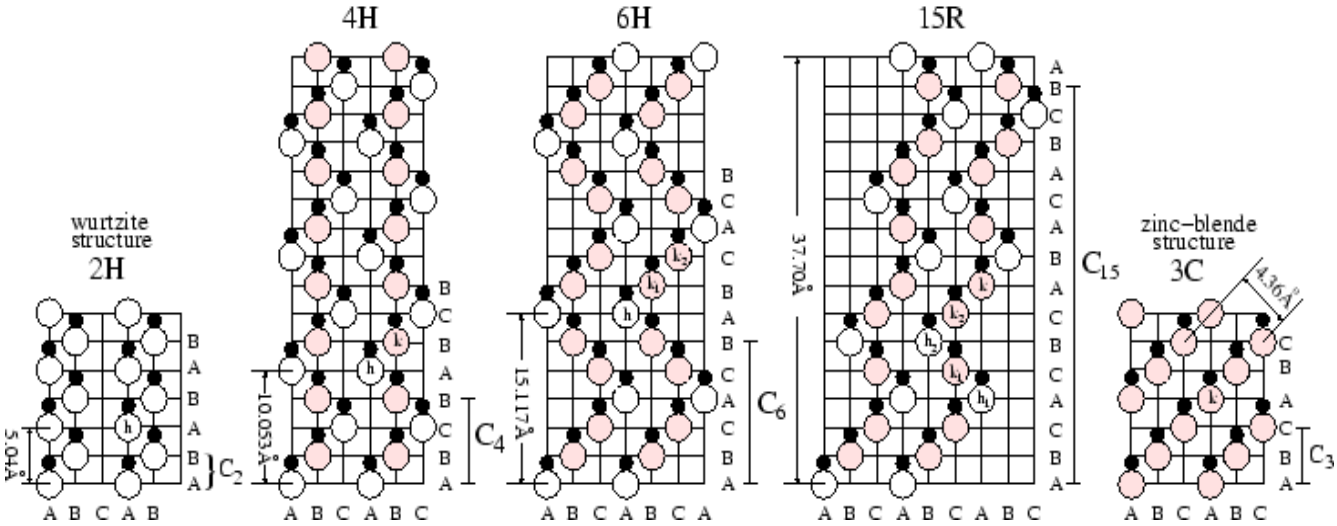

Figure 1-3: *The different stacking sequences for SiC polytypes in the [1120] plane taken from [22].*

To describe the different polytypes the following notation (the Ramsdell notation) is used: The cubic zinc blende SiC structure is used as the basis where the first layer is named A and the second is named B and the other C (they are placed according to a close-packed structure) as shown in figure 1-3. In the Ramsdell notation the number of layers in the stacking direction, before repeating the sequence, is combined with the letter representing the Bravais lattice type: cubic (C), hexagonal (H) or rhombohedral (R).

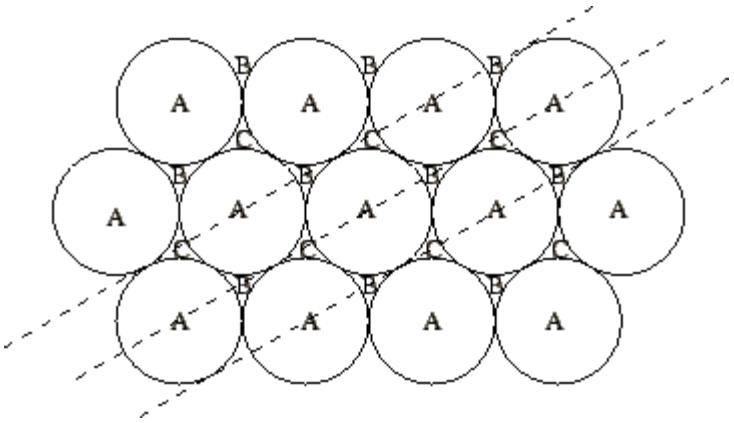

Figure 1-4: *SiC [0001] bilayer stacking sequence, showing the ABC.... sequence taken from [14].*

The only form of a cubic crystal lattice structure is 3C-SiC. Each SiC bilayer can be oriented into only three possible positions with respect to the lattice while the tetrahedral bonding is maintained. If these three layers are arbitrarily denoted A, B and C and the stacking sequence is ABCABC ..., then the crystallographic structure is cubic (zinc-blende) [27][28].

The stacking of the double layer for 2H-SiC layer is ABAB ..., the symmetry is hexagonal (wurtzite). All the other SiC polytypes are a mixture of the zinc-blende and wurtzite bonding. The 4H-SiC has a stacking sequence of ABCB…, it has an equal number of cubic and hexagonal bonds, while ABCACB…, is the stacking sequence for 6H-SiC polytype (which was used in this study) made of two-thirds cubic bonds and one-third hexagonal bonds. 15R-SiC is a rhombohedral crystal structure composed of three-fifth cubic bonds and two-fifth hexagonal bonds. Table 1.1 shows a summary of five common stacking sequences for SiC polytypes.

In this thesis 6H-SiC was used, which produce similar results to the chemical vapour deposited (CVD) SiC used in the TRISO and in device fabrication. Since the only difference

in this SiC is the stacking sequence, the atomic arrangement remains the same, which does not affect the SiC properties.

Table 1-1: SiC polytypes stacking sequence [28].

	Stacking sequence	No. Hexagonal (h) bonds	No. Cubic (k) bonds
2H	AB	1	0
3C	ABC	0	1
4H	ABCB	1	1
6H	ABCACB	1	2
15R	ABCACBCABACABCB	2	3

1.3 Tungsten

Tungsten (W) is an element with atomic number 74 and atomic weight of 183.85 g/mol. It is normally found in chemical compounds namely wolframite iron-manganese tungstate (Fe, Mn)WO_4, ferberite $FeWO_4$, hübnerite ($MnWO_4$) and Scheelite [calcium tungstate ($CaWO_4$)] [29][30]. It is a metal found under group VI d, with a Mohs hardness of 7.5. Tungsten is easily oxidized; that is, it combines with oxygen to form tungsten oxide, (WO_3.). Tungsten occurs naturally and has five isotopes with half-lives which are long and can be considered as stable [31][32]. In theory, all five are considered to be able to decay to form isotopes of hafnium by alpha emission [33].

There are two main crystal forms of tungsten, that is, the α-phase and β-phase [34]. The α-phase is body centred cubic (BCC) structure and is the most stable [35]. The β-phase

structure is metastable and is called A15 [36]. It should be noted that this β-phase can coexist with the α-phase at ambient conditions due to non-equilibrium synthesis by impurities [35]. The α-phase is stable, and crystallizes to an isometric grain, while the β-phase form displays a columnar pattern. The α-phase has one third of the electrical resistivity and a much lower superconducting transition temperature (T_C) relative to the β-phase: ca. 0.015 K vs. 1–4 K; mixing the two phases allows obtaining intermediate T_C values [35].

Tungsten is an extraordinary element known for its properties such as; robustness, high melting point, high density, low coefficient of thermal expansion compared with other metals, highly conductive, chemical resistant, excellent corrosion and abrasion resistance, etc. [37]–[39]. Its physical and electrical properties make it to be a desired material in different industries. Table 1.2 gives a summary of W physical and electrical properties.

Tungsten is used in many applications such as light bulb filaments, electrodes, X-ray tube (as both the filament and target), welding applications, super alloys, and radiation shielding (because of its electronic structure), vacuum tube filaments, heating elements, and rocket engine nozzles [36][40]. The high melting point permits tungsten to be suitable for use in aerospace and high-temperature use such as electrical, heating, and welding applications. It is also used in nuclear applications, electrodes, and in emitter tips in electron-beam instruments that use field emission guns, such as electron microscopes owing to its conductive and chemical inertness properties.

Table 1-2: Physical and Electrical Properties of Tungsten [41][42].

Atomic Radius	1.37Å
Ionic radius	2.10 Å
Melting point	3422 °C
Boiling point	3700 °C
Density	19.25 g/cm^3
Specific heat	135 $J.Kg^{-1}.K^{-1}$
Thermal conductivity (25 °C)	173 W/(m·K)
Coefficient of Thermal expansion (25 °C)	$(4.32 – 4.68) \times 10\text{-}6\ K^{-1}$
Electrical Resistivity	5.28 μΩ

1.4 W coating on SiC (Metal-ceramic composites)

SiC's mechanical and thermal properties can be improved by coating it with a refractory metal [43]. The metal-SiC strength depends on the adhesion of the metal-SiC interface. Stable interface between the metal and SiC is important for the structural integrity of the composite [44]. At high temperatures, reactions can take place during the production/use of metal-ceramic products resulting in different reactions products. This is due to the fact that some of the metals and ceramic (SiC) are not in thermodynamic equilibrium [45].

Due to its excellent properties, tungsten can be coated on SiC [37]. Addition of tungsten on SiC greatly enhances its structural properties, and improves their applications in electrical contact [46][47].

W-SiC composites are considered in a fusion nuclear reactor (power plant) as a structural diverter (Tungsten as a protection shield for SiC) [48]. Tungsten will be the armour used to protect the SiC from the high temperature and erosion by the energetic ions and neutral atoms escaping from the plasma [39][48][49] [50]. SiC (due to its high melting point, low erosion rate, low tritium retention and acceptably low radio-activation) is a candidate structural material for the first wall of blanket and diverter in fusion reactor. SiC is also a candidate for a cladding tube in helium gas-cooled fast reactor (fission reactor). Tungsten will be used for the upper-end plug of the fuel pin (see figure 1-5) [51]. The reason for considering tungsten as the armour or protection layer for SiC (reactor fuel) is due to the problems mentioned in section 1.1 i.e. escape of FPs from the SiC and reaction of FPs with the SiC which deteriorate the SiC structure. If studies can show that W-SiC composite gives good outcome/results, then adding W as a coating layer on SiC will serve as a solution in preventing the degrading of SiC as a protective layer.

Figure 1-5: *Joint of Nano-powder Infiltration and Transition Eutectoid (NITE)-SiC/SiC composite tube and tungsten cap on the fuel pin taken from [51].*

1.5 Research Motivation

The study of thin film material (thickness is in nanometres) is very important, because most of the application requires this order of thickness for electronic device fabrication and other

applications. These nano-films have distinctive properties different from bulk materials as a result of their geometry, physical dimensions and non-equilibrium microstructure [44]. They are made by physical vapour deposition (PVD) or chemical vapour deposition (CVD). The phases formed in thin films differ from the bulk materials [44]. Understanding the differences in bulk and thin film is important, especially in W-SiC thin film. Most device fabrication uses thin film coating to improve the device performance.

The problems encountered with SiC as a cladding material in fission reactors require some investigations on to how to prevent the escape of FPs from the SiC. As mention above, some of the escape of FPs through SiC, and the attack of SiC by palladium and zirconium have raised concerns on the integrity of SiC as the main diffusion barrier. Several studies have focused on the migration behaviour of FPs, interaction of some FPs with SiC and possibly replacement of the SiC by another material.

Coating the SiC by tungsten is a possible alternative. This will enhance the SiC properties and possibly assist in the retaining the FPs. Literature review for bulk W-SiC reaction material is available [39][48][49] [50], but there is limited information on W-SiC thin film reactions and structural changes.

Solid-state reactions of composites result in different microstructures and reaction products. Not all the reaction and structural changes are desired or good for the applications they are meant for. Knowledge of surface structural changes, compounds formed at the reaction zone and changes in the reaction zone between W and SiC are necessary. Solid-state reactions occurring at the W-SiC interface and the resulting structures at the interface are important

performance determining factors in W-SiC contacts. It is therefore essential to understand the mechanism of material stability and reactivity at this interface.

It is important to investigate the effect of W-SiC in different annealing atmospheres because this would assist in determining the lowest temperature at which the material will start reacting. It will also help to determine the temperature required to cause degradation of the material and get a deeper understanding of W-SiC structure. Since the use of W-SiC composite is not limited to annealing atmosphere, its thermal behaviour under different atmospheres needs to be investigated.

1.6 Research Objective

The aim of this thesis is to gain more insight in the solid-state interaction between W thin films deposited on 6H-SiC substrate at elevated temperatures using different annealing atmospheres. This involves investigating the temperature at which reaction(s) starts to occur, to identify the initial phases formed and observe the surface structural changes with each annealing temperature. This study focuses on investigating the effect of annealing W-SiC in vacuum, hydrogen gas and argon gas. This includes studying the surface structural behaviour upon annealing and how it is affected. It also includes studying how the reaction zone, initial reaction temperature and initial phases formed are affected by annealing in different atmospheres. This will assist in coming up with a model to explain how W-SiC behaves after annealing in different atmospheres.

1.7 Thesis outline

In this study, the interaction of W thin film deposited on SiC together with the surface morphology analysis were investigated using Rutherford backscattering spectrometry (RBS), grazing incidence X-ray diffraction (GIXRD), scanning electron microscopy (SEM) and atomic force microscopy (AFM).

This thesis is composed of 8 chapters and is outlined as follows: Chapter 1 is the introduction which includes the details of W and SiC together with the motivation of the study (which has already being discussed). Chapter 2 discusses diffusion theory in solids. Chapter 3 deals with thermodynamics, chapter 4 deals with metal-SiC reactions, chapter 5 reviews the work done on W-SiC by other researchers; chapter 6 is the experimental procedure. Chapter 7 discusses my results while chapter 8 summarizes/concludes what was done in the study.

1.8 References

[1] R. Elder and R. Allen, “Nuclear heat for hydrogen production: Coupling a very high/high temperature reactor to a hydrogen production plant,” *Prog. Nucl. Energy*, vol. 51, no. 3, pp. 500–525, 2009.

[2] “Ghosts of Pelindaba nuclear site break-in return to haunt South Africa | Neutron Bytes.” [Online]. Available: https://neutronbytes.com/2015/03/01/ghosts-of-pelindaba-nuclear-site-break-in-return-to-haunt-south-africa/.[Accessed 07-Sep-2016].

[3] N. G. van der Berg, J. B. Malherbe, A. J. Botha, and E. Friedland, “SEM analysis of the microstructure of the layers in triple-coated isotropic (TRISO) particles,” *Surf. Interface Anal.*, vol. 42, no. 6–7, pp. 1156–1159, Apr. 2010.

[4] K. Sawa, S. Ueta, and T. Iyoku, “Research and development program of HTGR fuel in Japan,” 2000.

[5] K. Verfondern, “HTGR Fuel Overview,” IEK-6, Res. Cent. Jülich, Ger. IAEA Train. Course HTGR Technol. Beijing, China, p. 1, 2011.

[6] K. Verfondern, “Fuel performance and fission product behaviour in gas cooled reactors,” Vienne, Austria, 1997.

[7] J. B. Malherbe, “Diffusion of fission products and radiation damage in SiC,” *J. Phys. D. Appl. Phys.*, vol. 46, no. 47, p. 473001, 2013.

[8] E. Friedland, J. B. Malherbe, N. G. van der Berg, T. T. Hlatshwayo, A. J. Botha, E. Wendler, and W. Wesch, “Study of silver diffusion in silicon carbide,” *J. Nucl. Mater.*, vol. 389, no. 2, pp. 326–331, 2009.

[9] T. T. Hlatshwayo, J. B. Malherbe, N. G. van der Berg, L. C. Prinsloo, A. J. Botha, E. Wendler, and W. Wesch, “Annealing of silver implanted 6H-SiC and the diffusion of the

silver," *Nucl. Instruments Methods Phys. Res. Sect. B Beam Interact. with Mater. Atoms*, vol. 274, pp. 120–125, 2012.

[10] J. H. O'Connell and J. H. Neethling, "Palladium and ruthenium supported silver migration in 3C–silicon carbide," *J. Nucl. Mater.*, vol. 456, pp. 436–441, 2015.

[11] J. H. Neethling, J. H. O'Connell, and E. J. Olivier, "Palladium assisted silver transport in polycrystalline SiC," *Nucl. Eng. Des.*, vol. 251, pp. 230–234, 2012.

[12] J. Y. Veuillen, T. A. Nguyen Tan, I. Tsiaoussis, N. Frangis, M. Brunel, and R. Gunnella, "Reaction of palladium thin films with an Si-rich 6H-SiC(0001)(3×3) surface," *Diam. Relat. Mater.*, vol. 8, no. 2–5, pp. 352–356, 1999.

[13] I. Tsiaoussis, N. Frangis, C. Manolikas, and T. A. Nguyen Tan, "The growth of Pd thin films on a 6H-SiC(0001) substrate," *J. Cryst. Growth*, vol. 300, no. 2, pp. 368–373, 2007.

[14] E. G. Njoroge, C. C. Theron, J. B. Malherbe, and O. M. Ndwandwe, "Kinetics of solid-state reactions between zirconium thin film and silicon carbide at elevated temperatures," *Nucl. Instruments Methods Phys. Res. Sect. B Beam Interact. with Mater. Atoms*, vol. 332, pp. 138–142, 2014.

[15] D. A. Petti, J. Buongiorno, J. T. Maki, R. R. Hobbins, and G. K. Miller, "Key differences in the fabrication, irradiation and high temperature accident testing of US and German TRISO-coated particle fuel, and their implications on fuel performance," *Nucl. Eng. Des.*, vol. 222, no. 2–3 SPEC, pp. 281–297, 2003.

[16] K. Fukuda and K. Iwamoto, "Xenon diffusion behaviour in pyrolytic SiC," *J. Mater. Sci.*, vol. 11, pp. 522–528, 1976.

[17] T. Bus, A. Van Veen, A. Shiryaev, A. V. Fedorov, H. Schut, F. D. Tichelaar, and J. Sietsma, "Thermal recovery of amorphous zones in 6H-SiC and 3C-SiC induced by low

fluence 420 keV Xe irradiation," *Mater. Sci. Eng. B Solid-State Mater. Adv. Technol.*, vol. 102, no. 1–3, pp. 269–276, 2003.

[18] E. Wendler, A. Heft, and W. Wesch, "Ion-beam induced damage and annealing behaviour in SiC," *Nucl. Instruments Methods Phys. Res. Sect. B Beam Interact. with Mater. Atoms*, vol. 141, no. 1–4, pp. 105–117, 1998.

[19] A. Qteish, V. Heine, and R. J. Needs, "Polarization, Structural and electronic properties of SiC polytypes," *Comput. Mater. Sci.*, vol. 2, pp. 389–394, 1994.

[20] C. Raynaud, "Silica films on silicon carbide: a review of electrical properties and device applications," *J. Non. Cryst. Solids*, vol. 280, pp. 1–31, 2001.

[21] Z. Zolnai, "Irradiation-induced crystal defects in silicon carbide," Budapest University of Technology and Economics, 2005.

[22] T. T. Hlatshwayo, "Diffusion of silver in 6H-SiC," University of Pretoria, 2010.

[23] E. L. Corral, "Ultra-high temperature ceramic coatings," *Adv. Mater. Process.*, vol. 166, pp. 30–32, 2008.

[24] K. Shimoda, N. Eiza, J. Park, T. Hinoki, A. Kohyama, and S. Kondo, "High-Temperature Mechanical Property Improvements of SiC Ceramics by NITE Process," *Mater. Trans.*, vol. 47, no. 4, pp. 1204–1208, 2006.

[25] R. Devanathan and W. J. Weber, "Displacement energy surface in 3C and 6H SiC," *J. Nucl. Mater.*, vol. 278, no. 2, pp. 258–265, 2000.

[26] A. Qteish, V. Heine, and R. J. Needs, "Structural and electronic properties of SiC polytypes," *Phys. B Condens. Matter*, vol. 185, pp. 366–378, 1993.

[27] U. Starke, "Atomic Structure of Hexagonal SiC Surfaces," *Phys. Status Solidi*, vol. 202, no. 1, pp. 475–499, 1997.

[28] J. B. Casady and R. W. Johnson, “Status of silicon carbide (SiC) as a wide-bandgap semiconductor for high-temperature applications: A review,” *Solid. State. Electron.*, vol. 39, no. 10, pp. 1409–1422, 1996.

[29] P. Pitfield and T. Brown, “Tungsten - Commodity Profile,” *Br. Geol. Surv.*, p. 34, 2011.

[30] W. Graham, “Tin-Tungsten ore,” *quartz-wolframite-(cassiterite-arsenopyrite) veins in greisen from Cligga Head, north Cornwall, England*, 2014. [Online]. Available: http://www.turnstone.ca/rom152co.htm. [Accessed: 07-Sep-2016].

[31] “Tungsten, Chemical Element - uses, elements, metal, gas, number, name, symbol, mass.” [Online]. Available: http://www.chemistryexplained.com/elements/T-Z/Tungsten.html. [Accessed: 09-Sep-2016].

[32] “Tungsten Isotopes - W Isotopes - Stable Tungsten Isotopes Supplier.” [Online]. Available: http://www.tracesciences.com/w.htm. [Accessed: 07-Sep-2016].

[33] “Tungstent Isotopes.” [Online]. Available: http://www.ctia.com.cn/TungstenNews/Print.asp?ArticleID=136353. [Accessed: 07-Sep-2016].

[34] L. Jeong-Seop, C. Jaehun, and Y. Chun-Yeol, “Growth and characterization of α and β-phase tungsten films on various substrates,” *J. Vac. Sci. Technol. A Vacuum, Surfaces, Film.*, vol. 34, no. 2, p. 21502, 2015.

[35] T. Karabacak, P. I. Wang, G. C. Wang, and T. M. Lu, “Phase transformation of single crystal β-tungsten nanorods at elevated temperatures,” *Thin Solid Films*, vol. 493, no. 1–2, pp. 293–296, 2005.

[36] T. Karabacak, P. I. Wang, G. C. Wang, and T. M. Lu, “Growth of Single Crystal Tungsten Nanorods by Oblique Angle Sputter Deposition,” *MRS Proc.*, vol. 788, p. L12.8, 2011.

[37] S. J. Son, K. H. Park, Y. Katoh, and A. Kohyama, “Interfacial reactions and mechanical properties of W–SiC in-situ joints for plasma facing components,” *J. Nucl. Mater.*, vol. 329–333, pp. 1549–1552, 2004.

[38] W. Tang and H. Zhang, “Status of Silicon Carbide Micromachining , Circuits and Sensing Devices,” pp. 1–10, 2011.

[39] J. Tan, Z. Zhou, M. Zhong, X. Zhu, M. Lei, W. Liu, and C. Ge, “Annealing behaviour and transient high-heat loading performance of different grade fine-grained tungsten,” *Phys. Scr.*, vol. T145, p. 14055, 2011.

[40] J. Christian, R.P. Singh Gaur, T. Wolfe, and J.R.L. Transorras, *Tungsten chemicals and their applications*. Towanda,PA,USA: Global Tungsten and Powders Corp., 2011.

[41] “Tungsten (W) - Chemical & Physical Properties.” [Online]. Available: http://www.tungsten.com/materials/tungsten/. [Accessed: 09-Sep-2016].

[42] “Tungsten Properties | International Tungsten Industry Association (ITIA),” 2011. [Online]. Available: http://www.itia.info/tungsten-properties.html. [Accessed: 09-Sep-2016].

[43] T. Ganne, J. Crépin, S. Serror, and A. Zaoui, “Cracking behaviour of PVD tungsten coatings deposited on steel substrates,” *Acta Mater.*, vol. 50, no. 16, pp. 4149–4163, 2002.

[44] E. G. Njoroge, “Solide-state interaction between Zr thin films and SiC,” University of Pretoria, 2014.

[45] A. Joshi, H. S. Hu, L. Jesion, J. J. Stephens, and J. Wadsworth, “High-Temperature Interactions of Refractory Metal Matrices with Selected Ceramic Reinforcements,” vol. 21, pp. 2829–2837, 1990.

[46] F. Goesmann and R. Schmid-Fetzer, “Stability of W as electrical contact on 6H-SiC: phase relations and interface reactions in the ternary system W-Si-C,” *Mater. Sci. Eng. B*, vol. 34, no. 2–3, pp. 224–231, 1995.

[47] J. Rogowski and A. Kubiak, “Effects of annealing temperature on the structure and electrical properties of tungsten contacts to n-type silicon carbide,” *Mater. Sci. Eng. B*, vol. 191, pp. 57–65, 2015.

[48] G. Matsuo, T. Shibayama, H. Kishimoto, K. Hamada, and S. Watanabe, “Micro-chemical analysis of diffusion bonded W-SiC joint,” *J. Nucl. Mater.*, vol. 417, no. 1–3, pp. 391–394, 2011.

[49] T. Hinoki, Y. Katoh, L. L. Snead, H. C. Jung, K. Ozawa, H. Katsui, Z.-H. Zhong, S. Kondo, Y. H. Park, C. Shih, C. M. Parish, R. A. Meisner, and A. Hasegawa, “Silicon Carbide and Silicon Carbide Composites for Fusion Reactor Application,” *Mater. Trans.*, vol. 54, no. 4, pp. 472–476, 2013.

[50] H. Kishimoto, T. Shibayama, K. Shimoda, T. Kobayashi, and A. Kohyama, “Microstructural and mechanical characterization of W/SiC bonding for structural material in fusion,” *J. Nucl. Mater.*, vol. 417, no. 1–3, pp. 387–390, 2011.

[51] H. Kishimoto, T. Shibayama, T. Abe, K. Shimoda, S. Kawamura, and A. Kohyama, “Diffusion Bonding Technology of Tungsten and SiC/SiC Composites for Nuclear Applications,” *IOP Conf. Ser. Mater. Sci. Eng.*, vol. 18, no. 16, p. 162015, 2011.

Chapter 2 : Diffusion

This chapter looks at the transport mechanism of atoms in solids. This mechanism is called diffusion and is usually observed when atoms move from a region of high concentration to a region of low concentration. In metal-SiC atoms are seen to move towards (interdiffuse) each other. In cases were a reaction is possible the diffusion will prompt a reaction resulting in the formation of new compounds. Changes in the metal-SiC crystal structure will also take place following a particular order.

In this study W was deposited on SiC and annealed at elevated temperatures to investigate the interaction between W and SiC. The reactions observed between the W and SiC are influenced by diffusion between this atoms. That is, when the atoms have enough energy to overcome the bonds holding them together, the atoms will be able to move (diffuse). Diffusion is the movement of particle in a solid from a region of high concentration to a region of low concentration as a result of random molecular motion. The net flux results from the random movement of atoms. There is a greater number of particles moving in random motion in a high concentration region than in low concentration region. This random motion is a result of the particles interacting (colliding).

Diffusion causes change in the structure of the material which eventually influences the physical and mechanical properties of the material [1]. The movement of the atoms is influenced by the temperature of the environment, and diffusion species. Diffusion acts as a mechanism which assists reactions which occur during deposition and after annealing

between the metal and substrate. In this chapter three diffusion mechanisms which occur in solids are discussed.

2.1 Diffusion Mechanism

There are several mechanisms that can lead to the movements of atoms in solid materials. This chapter focuses on the mechanisms that play a role in the diffusion between W and SiC. These mechanisms are: vacancy diffusion, interstitial diffusion and grain boundary diffusion. The movement of atoms in solids leads to chemical reactions and microstructural changes of the two materials at the interface. Diffusion takes place due to the presence of defects such as point defects and grain boundaries. Point defects include interstitial defects and vacancies which are responsible for volume diffusion. In general, grain boundary diffusion mechanism has lower activation energies than lattice diffusion. Thus it is dominant at low temperatures in solids. Point defects are dominant in solids at high temperatures which leads to an increase in lattice/volume diffusion supressing grain boundary diffusion [2].

2.1.1 Vacancy Mechanism

In solids crystals there are unoccupied lattice sites called vacancies which play a role in the diffusion of atoms [3]. The empty lattice sites will exchange positions with the neighbouring atoms leaving an empty site behind [1]. This process is called vacancy diffusion. The atom moves by jumping into the vacancy. The direction which the atom moves will be opposite that of the vacancy (as it will seem as though the vacancy is also moving) as shown in figure 2-1. This type of mechanism is favoured if the diffusing atom is adjacent to the vacancy.

Vacancies occur naturally in all crystal since they are imperfect. They are formed during solidification because of the vibrations of atoms and local rearrangement of atoms.

The probability for any atom in a solid to move is the product of the probability of finding a vacancy in an adjacent lattice site:

$$N_v = N\ exp\left(-\frac{E_v}{k_B T}\right) \qquad (2.1)$$

N_v is the number of vacancies per unit volume, N is the total number of atomic sites, E_v is the energy required to move the atoms from a lattice site within the solid crystal to the vacancy, k_B is the Boltzmann constant and T denotes the absolute temperature in Kelvin. From equation 2.1 it is quite clear that an increase in temperature leads to an increase in vacancies in a solid crystal material.

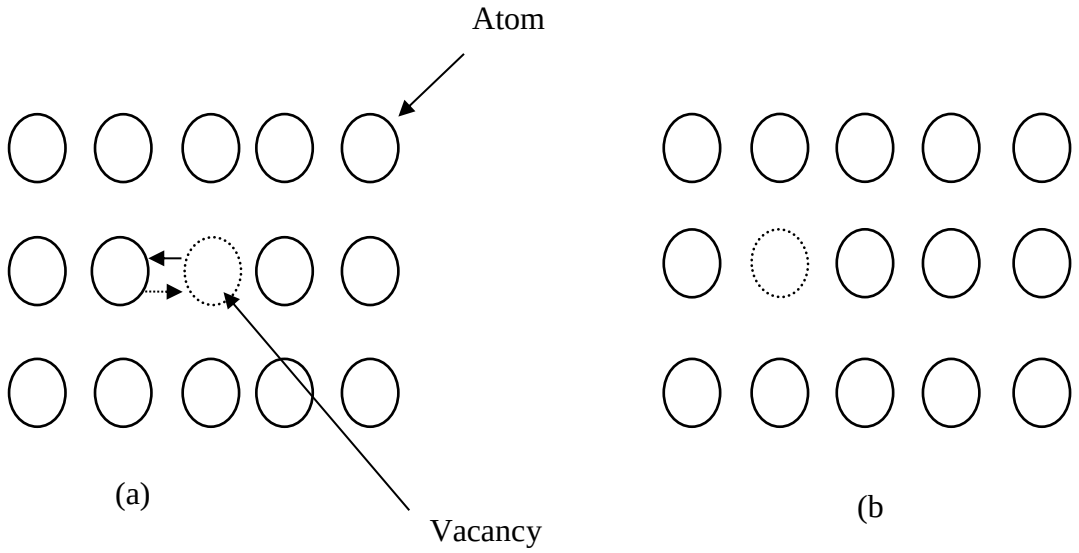

Figure 2-1: *Schematic representation of the vacancy diffusion mechanism, with (a) and (b) representing the position of the vacancy before and after diffusion. The dotted circle represents the vacancy.*

2.1.2 Interstitial and Interstitialcy Mechanism

In solid crystals, there are atoms located on the unoccupied sites in the crystal structure not on their regular position these atoms are called interstitial atoms. Interstitial atoms can be bigger or smaller than the atoms of the host material. Since there are more interstitial sites in solids than vacancies, the probability of interstitial diffusion to take place is higher than vacancy diffusion. Small interstitial atoms can readily diffuse by meandering in the interstices [4] and it is faster than vacancy diffusion [3]. In interstitial diffusion, the interstitial atoms jump from their interstitial sites to the neighbouring sites which are empty as shown in figure 2-2. There are other variations of interstitial diffusion that involve displacing a neighbouring atom to an interstitial position, termed interstitialcy or kickout mechanism [5].

Figure 2-2*: Interstitial mechanism, (a) before and (b) after interstitial diffusion took place.*

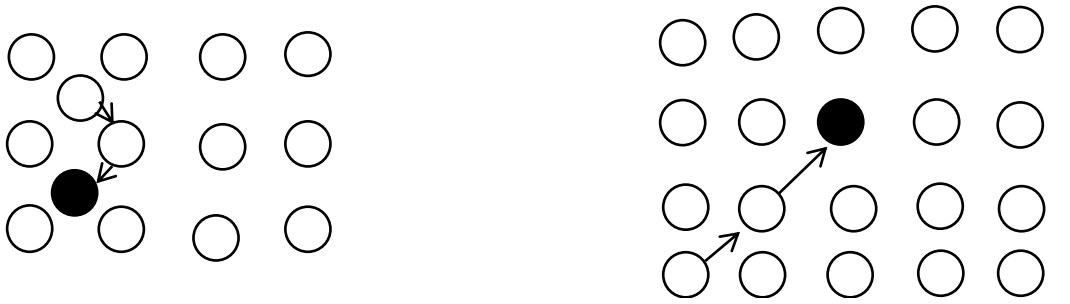

Figure 2-3: *The interstitialcy mechanism, (a) before and (b) after interstitialcy diffusion.*

In interstitialcy there are two types of movement that can take place. Collinear movement is when the atom pushes in the same direction as the motion of the interstitial atom as illustrated in figure 2-3 (b). In the non-collinear movement the atom pushes in the direction non-linear to the direction of the motion of the interstitial atom, see figure 2-3 (a).

2.1.3 Grain boundary Diffusion and Dislocation

Point defects are not the only type of diffusion mechanisms in crystals; there are other types of defects which influences the movement of atoms, such as grain boundaries and dislocations. Grain boundary diffusion is the diffusion of the diffusing specimen along the grain boundaries in a polycrystalline solid. Dislocation diffusion takes place when adjacent sub-units of a cluster move in a row by row manner through displacement of a dislocation.

Metal films are mostly prepared by physical vapour deposition (PVD) such as sputtering and evaporation and chemical vapour deposition (CVD) which results in polycrystalline structures. These kinds of film generally have high dislocation densities. Grain boundary and dislocation mechanisms have smaller activation energies as compared to lattice diffusion at low temperatures. The rate of diffusion will be relatively higher via grain boundaries than in lattice diffusion [4]. Atoms are less bound along a grain boundary as a result the atoms in a grain boundary will have higher energy state than atoms in a normal lattice position[3].

2.2 References

[1] P. Shewmon, *Diffuion in Solids*, Second. USA: The Mineral, Metals and Society, 1989.

[2] E. G. Njoroge, “Solide-state interaction between Zr thin films and SiC,” University of Pretoria, 2014.

[3] W. D. Callister, *Materials Science and Engineering*. New York, USA: John Wiley and Aons, 2007.

[4] D. Gupta, Diffusion processes in advanced technological materials. USA: William Andrew, 2004.

[5] D. Gupta and P. S. Ho, “Diffusion Processes in Thin Films.,” *Thin Solid Films*, vol. 72, no. 3, pp. 399–418, 1980.

Chapter 3 : Thermodynamics

In this study, the interaction between W thin film and SiC were investigated. W-SiC samples were annealed in vacuum, hydrogen and argon. To understand the nature and mechanism of the interaction between W and SiC, the thermodynamics of this system has to be understood. This chapter discusses the thermodynamics of metal-SiC in order to understand the driving force which promotes chemical reaction to take place. These include the discussion of Gibbs free energy, enthalpy, entropy and heat capacity of elements. The compounds in systems such as binary and ternary phase diagrams will also be discussed.

Phase diagrams are used to represents chemical equilibrium conditions for systems as a function of temperature, pressure and composition. This study only focuses at solid state interaction between W and SiC (W-SiC) which has three compositional elements. Hence, understanding the application of a ternary diagrams is very important.

3.1 Mass Action Law

According to the mass action law, the rate at which a substance reacts is proportional to its active mass, (Rate $\propto$ Reactant). When a reaction takes place in a closed system, the ratio of the reactant and products should be constant for chemical equilibrium to be reached. Chemical equilibrium is meet when there is a fixed relationship between the activities of the following components: pressure, temperature, and the period of time required (for the system to reach equilibrium). The mass action law can be introduced by using a general chemical

reaction equation in which reactants A and B react at elevated temperatures to give product C and D [1]:

$$aA + bB \rightarrow cC + dD \qquad (3.1)$$

where *a, b, c, d* are the coefficients for a balanced chemical equation. A numerical value can be assigned to the equilibrium state (mass action expression K_{eq}) of a reaction by the mass action law. For a system in equilibrium, there must be fixed relationship between activities of the components. The mass action law states that if the system is at equilibrium at a given temperature, then the following ratio is a constant [1][2] :

$$K_{eq} = \frac{[C]^c[D]^d}{[A]^a[B]^b} \qquad (3.2)$$

K_{eq} is the equilibrium constant for the reaction in (3.1) and the square brackets "[ ]" around the chemical species represent their concentration, A and B are the reactants, C and D are the products.

3.2 Gibbs Free Energy

Gibbs free energy is a thermodynamic quantity that measures the maximum or reversible work that may be performed by a thermodynamic system at a constant temperature, *T* and pressure, *p*. A change in Gibbs free energy (ΔG) is required for a chemical reaction to take place. The change in Gibbs free energy determines whether a chemical reaction will be spontaneous ($\Delta G < 0$) or non-spontaneous ($\Delta G > 0$) [3][4]. Under normal circumstances a continuous decrease in the reactants concentration will take place with progressive increase in

the product concentration, until the reaction attains its state of equilibrium and there is no longer a change in concentration. ΔG at chemical equilibrium is zero with constant pressure (p) and temperature (T). Gibbs free energy (G) is a quantity that combines enthalpy and entropy at absolute temperature and is defined as follows [3][4]:

$$G = H - TS \tag{3.3}$$

where G is the Gibbs free energy, H the enthalpy, T temperature and S the entropy. For a process taking place at constant T and p, the change in Gibbs free energy is:

$$\Delta G = \Delta U + p\Delta V - T\Delta S = \Delta H - T\Delta S \tag{3.4}$$

where U is the internal energy, p the pressure, V the volume, T the temperature, S the entropy and H the enthalpy of the system. By adding the Gibbs free energy formation ΔG_f^o of the products and subtracting from the reactants using Hess's principle, the change in Gibbs free energy can be calculated [5]. The change in Gibbs free energy (ΔG) for a chemical reaction can also be deduce from the partial molar Gibbs free energy or chemical potentials of the participating species [3]. The change in Gibbs free energy can predict whether or not a reaction will take place and the products formed at the interface during the reaction can be predicted [6]. ΔG represents Gibbs free energy change for a reaction when the reactants and products are present in any arbitrary thermodynamic state, while ΔG^o denotes the Gibbs free energy change for the same reaction when all the reactants and products are in their standard state [3]. Standard state is a reference point which is used to calculate the properties of the material under different conditions. ΔG^o is the standard free energy of reaction which can be calculated from equation (3.4) using standard entropy and enthalpy for reaction:

$$\Delta G^o = \Delta H_f^o - T\Delta S^o \quad (3.5)$$

where $H_f°$ is the heat of formation (enthalpy) of the material and $S°$ entropy of the material. The standard Gibbs free energy of reaction can be calculated using ΔH_f^o and S^o values from the thermodynamic tables (to first calculate ΔH^o and ΔS^o) [7]. Enthalpies of formation and entropies can be calculated if the change in heat capacity of the reactants and products is known at constant pressure. The Gibbs free energy of reaction can also be calculated from the values of standard free energy of formation ΔG_f^o [8]. ΔG_f^o is the change in Gibbs free energy when one mole of a substance is formed from elements in their standard state.

$$\Delta G^o = \sum \Delta G_f^o(products) - \sum \Delta G_f^o(reactants) \quad (3.6)$$

In most cases when ΔG^o is zero, the value for ΔH_f^o is also zero for elements.

Since the heat capacity of reactants and products are almost the same, the change in the heat capacities is always nearly zero ($\Delta C_p \approx 0$) for solid state reactions. This is called the Neumann-Kopp rule [9]. In equation (3.5) the values for ΔH^o and ΔS^o are functions of the change in heat capacity (ΔC_p) at constant pressure as illustrated in the equations below:

$$\Delta H^o(T) = \Delta H^o(298) + \int_{298}^{T} \Delta C_p dT \quad (3.7)$$

$$\Delta S^o(T) = \Delta S^o(298) + \int_{298}^{T} \frac{\Delta C_p}{T} dT \quad (3.8)$$

For good approximation in solid state reactions, equation (3.5) can be rewritten as [10]:

$$\Delta G^o(T) = \Delta H^o_{298} - T\Delta S^o_{298} \quad (3.9)$$

In reactions whereby the annealing temperatures are below the melting points of the reactants and products (and the volume changes are negligibly small), the change in entropy contribution is small ($\Delta S \approx 0$). Equation (3.9) can be reduced to (3.10) below when $T\Delta S^o_{298}$ is small relative to ΔH^o_{298} [9]:

$$\Delta G^o_T \approx \Delta H^o_{298} \quad (3.10)$$

Thus for experimental temperatures below the melting point of reactants and products, the standard values (at T = 298 K) of enthalpy and entropy can be used for thermodynamics calculations. The change in Gibbs free energy can also be approximated by the standard enthalpy only, when the change in entropy is considered to be zero.

3.3 Phase Diagrams

Phase diagrams are graphs representing the physical states of a substance under different conditions such as temperature, composition and pressure. The pressure and composition are normally represented on the x-axis and temperature on the y-axis. Two states of the substance coexist in equilibrium on the lines or curves. A phase diagram allows us to find out precisely what phases are present at any given temperature and pressure.

3.3.1 Tungsten-Carbon Binary phase diagram

The W-C phase diagram in figure 3-1 represent temperature range of 1250 to about 3750 ºC, the melting point of W is above 3500 ºC. When tungsten is combined with carbon (deposited then heated at high temperatures) it reacts to form two different tungsten carbides. These two tungsten carbide phases that are formed are WC and W_2C. The W-C phases formed have: hexagonal W_2C which crystallizes in three modifications, the PbO_2, Fe_2N and CdI_2 types structures denoted by β, β', and β" respectively, the cubic sub-carbide WC_{1-x} is found to crystallize in the NaCl type structure represented by γ, and the hexagonal WC denoted δ [11]. From figure 3-1 W + δ-WC exist at the temperature below 1523 K. The β"-W_2C phase is a euctectoid results of the reaction between W and δ-WC at 1523 K. During the γ-WC production, the W_2C stoichiometry phases are attained as intermediate products. A eutectoid reaction between β-W_2C and δ-WC at 2789 K gives rise to γ-phase which melts at approximately 2993 K. The δ-WC is the only binary phase stable at room temperature and has almost no solid solubility up to 2657 K but may become carbon deficient between this temperature and its incongruent melting point [11]–[13].

A cubic phase γ-WC_{1-x} exist in the composition range between the lower tungsten carbide β-W_2C and the higher carbide δ-WC. This single-phase γ-WC_{1-x} exists in a varying composition from $WC_{0.58}$ to $WC_{0.65}$ at temperatures above 2790 – 3028 K [14]–[16]. The γ-WC_{1-x} may exist in equilibrium with β-W_2C or δ-WC [12]. Rudy and Hoffman [14] showed that the cubic phase γ-WC_{1-x} forms readily from melting, but direct solid transformation from δ-WC → γ-WC_{1-x} requires that the temperature be changed slowly near transformation temperature.

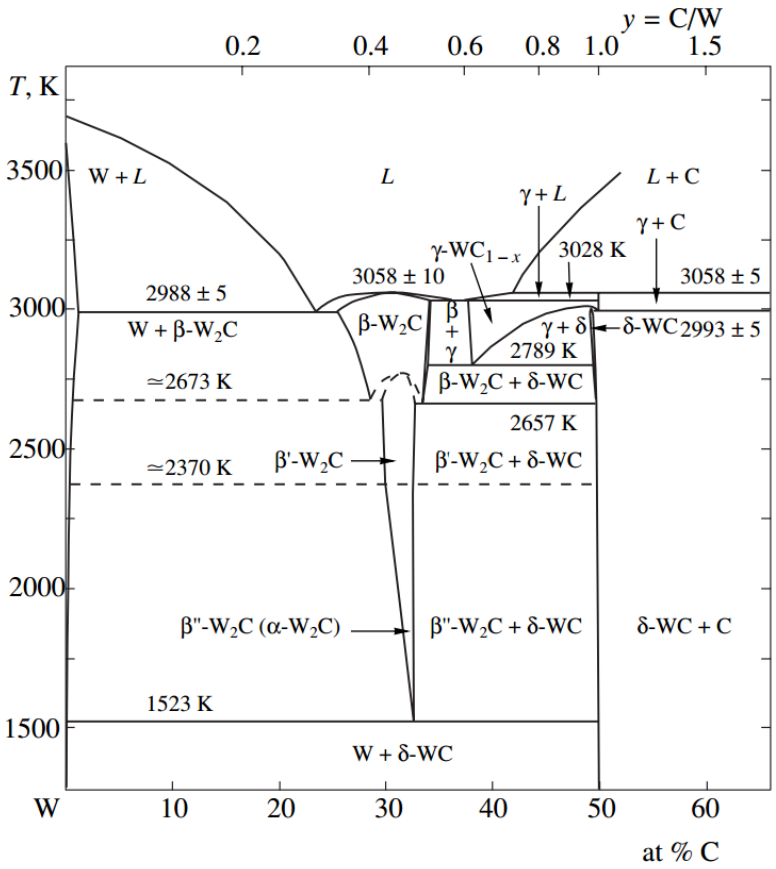

Figure 3-1: *W-C binary diagram obtained from Kurlov-Gusev [12].*

3.3.2 Tungsten-Silicon binary phase diagram

The W-Si binary diagram give rise to two silicide phases and they are stable phases [17][18]. These phases which form are WSi_2 and W_5Si_3 as indicated in figure 3-2 below. The diagram indicates that the melting point of WSi_2 is 2184 °C at 34 at. % of Si. WSi_2 exists at temperatures of 1382 °C. The mixture of WSi_2 and W_5Si_3 is found to exist between 35.5 at. % of Si and 64.5 at. % of W at 2013 °C and they have a melting point of 2324 °C. W_5Si_3 has a melting point above 2400 °C at 10 at. % of W. Both the tungsten silicides have tetragonal phases.

The W_5Si_3 and WSi_2 at eutectic point 2013 °C are known as daltonide phases [17]. These mean that the ratio of atoms for metal-W and ceramic-Si at constant temperature intervals of solid phases existence as: (5:3) for W_5Si_3 and (1:2) WSi_2.

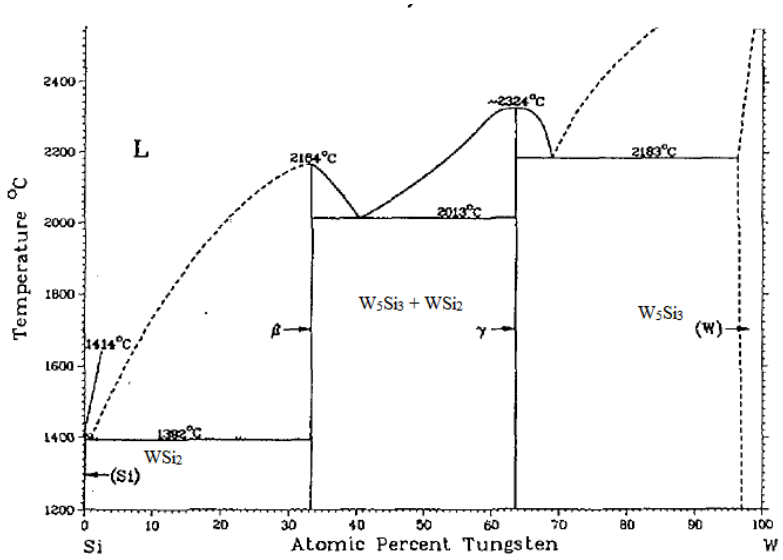

Figure 3-2: *W-Si binary diagram obtained from [17].*

3.3.3 Ternary phase diagram for W-Si-C

The two ternary phase diagrams represented in figure 3-3 below were calculated using Gibbs free energy from the thermodynamic data in Table 3.1 [18]. Phase diagrams are equilibrium diagrams indicating the equilibrium states of a system [5]. The W-Si-C ternary phase diagram shows all the compounds present in the systems. It also informs us whether equilibrium exists between the phases formed [19]. The compounds and elements that react chemically with each other are shown by lines with arrows connecting them. The tie-lines show the equilibrium states of the compounds and elements.

Table 3-1: The enthalpy (ΔH) and entropy (TΔS) terms comprising the Gibbs energy of formation (ΔG) of binary compounds in the W-Si-C system at 300 K and 2200 K [18].

Compound	T (K)	ΔH (kJ/mol)	TΔS (kJ/mol)	ΔG (kJ/mol)
WC	300	-40.16	1.80	-38.56
WC	2200	-38.40	5.53	-32.80
W_5Si_3	300	-135.20	-8.25	-143.56
W_5Si_3	2200	-276.93	126.36	-150.56
WSi_2	300	-93.00	1.88	-91.11
WSi_2	2200	-194.60	149.21	-45.39
W_2C	300	-26.32	4.46	-21.86
W_2C	2200	16.23	-66.51	-50.19
SiC	300	-73.22	2.38	-70.83
SiC	2200	-122.17	81.20	-40.97

Figure 3-3 (a) shows the possible diffusion path indicted by the solid lines with arrows and the broken lies show the tie-lines. The tie-lines tell us which compounds are in equilibrium with each other. SiC and WC are the two compounds on the Si-C and W-C ternary diagram side that form a phase with (1:1) stoichiometry. W-C side also gives rise to a tungsten rich phase W_2C. The W-Si side also results to two stable phases, one which is tungsten rich W_5Si_3 and the other which is silicon rich WSi_2. These carbides and silicides formed are found to be stable and coexist in equilibrium at temperature range $300 < T < 2200$ K. At the temperature range of $300\ K < T < 970\ K$ WSi_2 is stable with WC and SiC. It can be seen from that diffusion path that WSi_2 and WC will be the first two phases to form after the initial reaction between W and SiC.

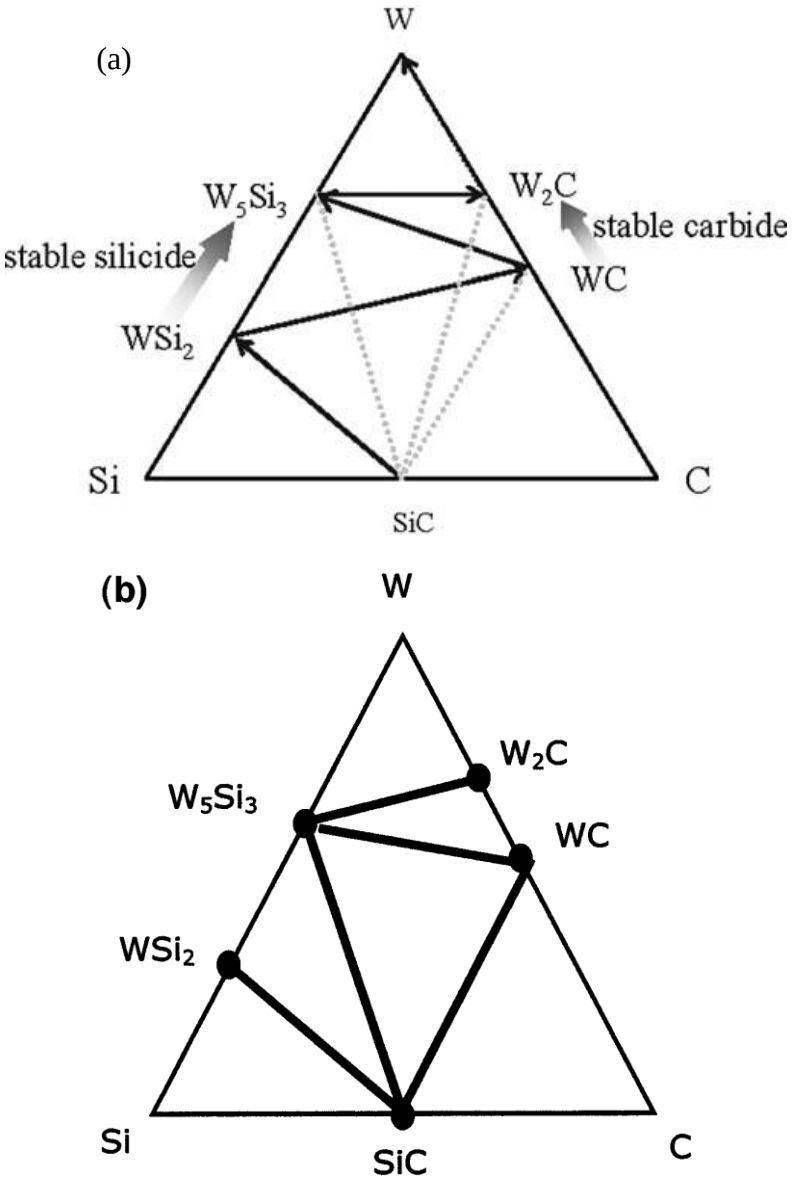

Figure 3-3: *A schematic diagram of (a) the ternary diagram of W-Si-C at elevated temperatures (300 K < T < 2200 K)taken from [20]. (b)Ternary diagrams of W-Si-C ternary diagram for temperature at 970 K < T < 2140 K, taken from [18].*

In figure 3-3 (b) with a temperature range of 970 K < T < 2140 K, W_5Si_3 becomes stable with WC and SiC. The WSi_2 phase is still present but only stable with SiC and is no longer the dominant silicide. At temperatures of 2140 K < T < 2200 K W_2C appears and it is stable with W_5Si_3 and SiC. W_5Si_3 becomes dominant silicide; in some instances is the only silicide present [20]. W_2C becomes the dominant carbide though both the carbide coexists. The

stability and existence of this carbides and silicides changes with temperature, and this trend of stability is not always followed when experiments are conducted [18]–[20]. An extensive discussion with regards to ref [19] is found in chapter 5.

3.4 References

[1] K. J. Mysels, “Textbook errors: VII: The laws of reaction rates and of equilibrium,” *J. Chem. Educ.*, vol. 33, no. 4, pp. 178–179, 1956.

[2] E. A. Guggenheim, “Textbook errors: Guest column. IX: More about the laws of reaction rates and of equilibrium,” *J. Chem. Educ.*, vol. 33, no. 11, pp. 544–545, Nov. 1956.

[3] Y. K. Rao, *Stoichiometry and Thermodynamics of Metallurgical Processes*. New York: Cambridge University Press, 1985.

[4] L. Ryan and R. Norris, *Cambridge International AS and A level Level Chemistry Coursebook*, Second. United Kindom: Cambridge University Press, 2014.

[5] E. G. Njoroge, “Solide-state interaction between Zr thin films and SiC,” University of Pretoria, 2014.

[6] D. Gupta, Diffusion processes in advanced technological materials. USA: William Andrew, 2004.

[7] E. S. T. Brown, E. H. LeMay, B. E. Bursten, C. Murphy, P. Woodward, *Chemistry: The central Science*, 13th ed. USA: Prentice Hall, 2014.

[8] L. D. Reger, S. R. Goode, and D. W. Ball, *Chemistry: Principles and Practice*, 3rd ed. Belmont, USA: Brooks/Cole, 2009.

[9] R. Pretorius, T. K. Marais, and C. C. Theron, “Thin film compound phase formation sequence: An effective heat of formation model,” *Mater. Sci. Reports*, vol. 10, no. 1–2, pp. 1–83, 1993.

[10] L. Brewer and O. Krikorian, “Reactions of Refractory Silicides with Carbon and Nitrogen,” *J. Electrochem. Soc.*, vol. 103, no. 1, p. 38, 1956.

[11] “Tungsten Carbide Metals: Part One :: Total Materia Article.” [Online]. Available: http://www.totalmateria.com/page.aspx?ID=CheckArticle&site=ktn&NM=364. [Accessed: 14-Mar-2016].

[12] A. S. Kurlov and A. I. Gusev, “Tungsten carbides and W-C phase diagram,” *Inorg. Mater.*, vol. 42, no. 2, pp. 121–127, 2006.

[13] M. D. Demetriou, N. M. Ghoniem, and A. S. Lavine, “Modeling of graphitization kinetics during peritectic melting of tungsten carbide,” *Acta Mater.*, vol. 50, no. 20, pp. 4995–5004, 2002.

[14] Rudy, E. and Hoffman, J.R., “Phasengleichgewichte im Bereich der kubischen Karbidphase im System Wolfram–Kohlenstoff,” *Planseeber. Pulvermetall*, vol. 15, no. 3, pp. 174–178, 1967.

[15] E. Rudy, “Ternary phase equilibria in transition metal-boron-carbon-silicon systems. Part 5. Compendium of phase diagram data,” Ohio, 1969.

[16] E. Rudy, S. Windisch, and J. R. Hoffman, “W–C System: Supplemental Information on the Mo–C System. Ternary Phase Equilibria in Transition Metal–Boron– Carbon–Silicon Systems (Part I. Related Binary Systems, vol. VI),” Ohio, 1966.

[17] B. A. Gnesin, P. A. Gurjiyants, and E. B. Borisenko, “Eutectics Me_5Si-$MeSi_2$ in a triple system Mo-W-Si,” *15'" Int. Plansee Semin. Eds. G. Kneringer, P. Rddhammer H. Wildner, Plansee Hold. AG, Reutte*, vol. 1, pp. 420–434, 2001.

[18] W. F. Seng and P. A. Barnes, “Calculations of tungsten silicide and carbide formation on SiC using the Gibbs free energy,” *Mater. Sci. Eng. B*, vol. 72, pp. 13–18, 2000.

[19] F. Goesmann and R. Schmid-Fetzer, “Metals on 6H-SiC: contact formation from the materials science point of view,” *Mater. Sci. Eng. B*, vol. 46, no. 1–3, pp. 357–362, 1997.

[20] S. J. Son, K. H. Park, Y. Katoh, and A. Kohyama, “Interfacial reactions and mechanical properties of W–SiC in-situ joints for plasma facing components,” *J. Nucl. Mater.*, vol. 329–333, pp. 1549–1552, Aug. 2004.

Chapter 4 : Metal-SiC reaction

4.1 Metal-SiC Reactions

Due to the vast load of technological applications of metal-SiC, it is important to study their interactions and structural changes. Understanding the mechanism of the material stability, reaction and sensitivity in different annealing conditions is also important. This will help gain a much better understanding of what is happening at the interface and how it will affect the metal-SiC composite. Since an interface reaction between metal-SiC leads to structural instability and may deteriorate its mechanical properties.

A reaction between SiC and certain metals occurs when they are brought into contact at a sufficiently high temperature. This results in a change in the structure of the material creating new interfaces [1]. The reaction may lead to a formation of meta-stable or stable interfacial structures and formation of new phases. The reactivity, reaction products formed, sequence and interface morphology in the metal-SiC are dependent on the contact material [2]. In most cases the reaction takes place during sample fabrication and application stages or high temperature consolidation processes.

Studies done in the past years involving metal-SiC interfaces have investigated solid state reactions, interface morphology, microstructure and thermal capabilities [3]–[8]. Most of these studies have been concentrating primarily on the determination of reaction products of metal/SiC reactions, and the growth kinetics of reaction layers [9].

When solid state reaction between metal and SiC occurs the formation of new phases due to mass transfer of constituent elements at the interface takes place. These reactions are normally governed by thermodynamics and reaction kinetics of the metal-SiC system. The The kinetics factors also determine the quantity in which the phase can be formed [10]. The leading driving forces for phase formation in solid-state reaction are usually the Gibbs free energy and the enthalpy of formation [11]. The reduction of the Gibbs free energy due to reaction determines if a metal-SiC reaction will arise at elevated temperatures.

A chemical reaction occurs when SiC dissociates into Si and C which reacts with the metal. Si and C will diffuse toward the metal, while the metal diffuses towards the SiC across the interface to form new phases. The dissociation of SiC at elevated temperatures is influenced by the affinity of Si and C for the metals and vice versa [12]. Not all metals react with SiC, thus the reaction between metal and SiC can be classified into reactive and non-reactive metal-SiC [13].

4.1.1 Non-reactive metal-SiC system

A non-reactive system usually does not allow a reaction between metal and SiC to take place. Mass transfer occurs along the SiC surface leading to a two-phase region between SiC and the metal [14]. The interdiffusion between the metal and SiC take place but no reaction occurs. Under experimental conditions no chemical reaction between metal and SiC occurs and the materials tend to have large solubility regions. Some of the metals which do not react with SiC are: Au [15], Sn, Cu [16], Pb, Ge [17], Ag [18].

4.1.2 Reactive Metal-SiC systems

In a reactive system, SiC will decompose to Si and C first, then interdiffusion between the metal and SiC will occur. A reaction zone (RZ) at the interface where the metal and SiC have reacted will be formed. Metal silicides, metal carbides or ternary carbosilicides will form at the RZ. The reaction follows [2][19]:

$$M + C \rightarrow \text{M-Carbide} \quad (4.1)$$

$$M + Si \rightarrow \text{M-Silicide} \quad (4.2)$$

$$M + Si + C \rightarrow \text{Ternary Phase} \quad (4.3)$$

$$M + Si + C \rightarrow \text{M-Silicide + graphite} \quad (4.4)$$

The metal-SiC reactions can be categorized into three types [2][20] and figure 4-1 shows a schematic diagram of the reaction types:

$$M + SiC \rightarrow \text{M-Silicide + C} \quad \text{Type I}$$

$$M + SiC \rightarrow \text{M-Silicide + M-Carbide} \quad \text{Type II}$$

where M represents metal taking part in the reaction.

In Type I reaction, the metal reacts with silicon to form stable silicide phases leaving free carbon at the reaction zone. Compounds are not formed between the metal and carbon. Either

Si or both Si and C will diffuse into the metal only to form silicides [21], and free carbon will exist [2]. In order to satisfy the mass balance requirement in this system, silicides are produced with existence of free carbon. Some of the metals which will only react with Si in the SiC system such as: Co [8], Fe [6], Ni [22], Pd [23].

In type III reactions, the formation of free silicon and metal-carbide phases occurs. Both the Si and C will diffuse into the metal, but only carbon will react [21].

$$M + SiC \rightarrow Si + M - Carbide \qquad \text{Type III}$$

The type III reaction is rarely observed [12] and they are commonly observed to take place with reaction type II [20]. One of the examples of the metal which react with SiC to form only a carbide is Al. It forms Al_4C_3 at temperatures of 1373K, this is not understood from the thermodynamic stability point of view [20]. Since the free energy change of the reaction is positive the reaction does not spontaneously proceed [24].

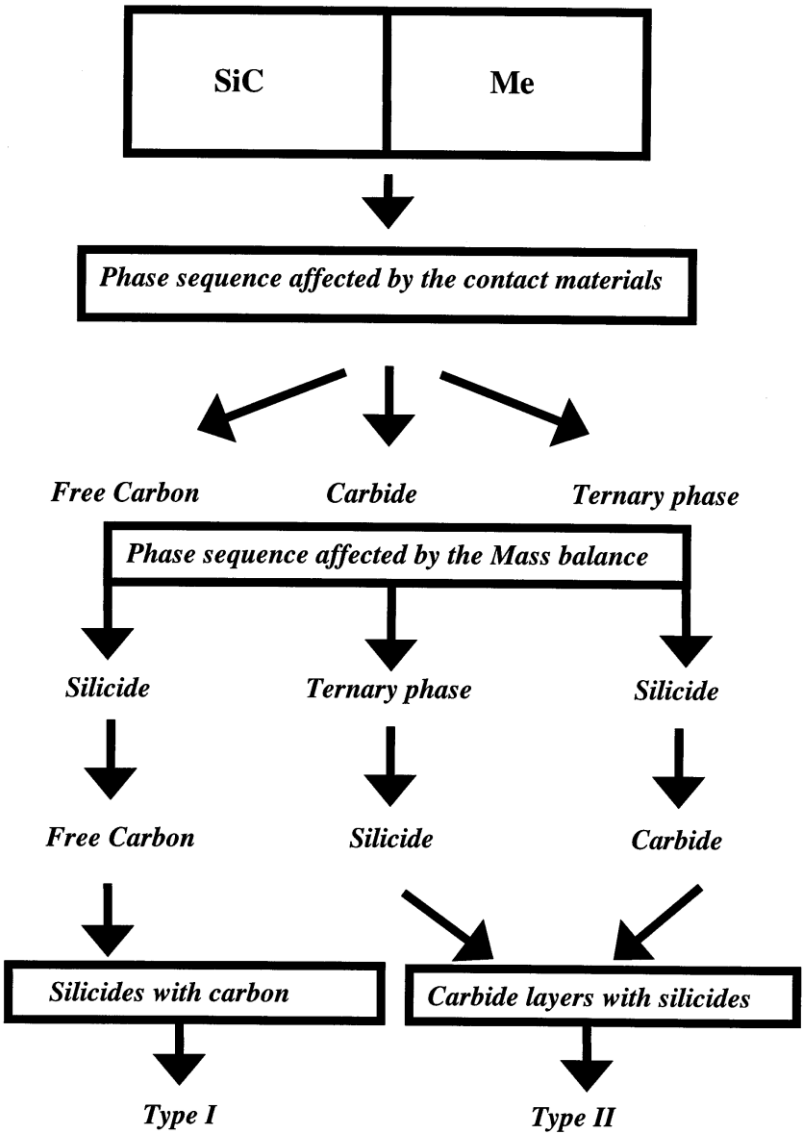

Figure 4-1: *Schematic diagram representing metal-SiC expected reactions after heat treatment, taken from [2].*

The degree of reactivity between metal and SiC can be obtained from the magnitude in the changes of the standard free energies of formation of silicides and carbides. The thermodynamic data provides information of the reaction products to be formed. This knowledge enables prediction of the kinds of reaction products to be expected.

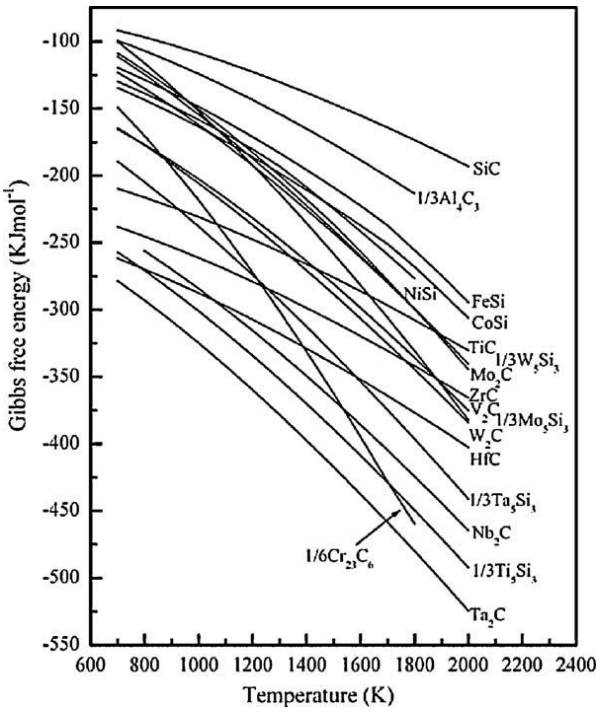

Figure 4-2: *Gibbs Free energies of the formation of SiC, carbides and Silicides, taken from [21].*

The Gibbs free energies of formation of SiC and of the main carbides and silicides are given figure 4-2. The reactivity of Al, Fe, Ni and Co with SiC is said to be low because of the small differences of the Gibbs free energy of formation between the silicides, carbides and SiC [21]. Metals such as Hf, Ti, Cr, Zr, etc. have high reactivity when they are brought into contact with SiC to form both silicides and carbides. The difference in Gibbs free energy of formation between SiC, silicides and carbides (of these metals) is greater than that those of metals which do not form carbides [21].

For Type II reaction, a layer containing both silicides and carbides is created at the interface with a mutual diffusion between the metal and SiC. In this case carbon acts as a dominant component compared to the other elements (metal affinity of carbon is high) [2]. In type II reaction there will not be any free silicon because Si also reacts with the metal. The product

which is formed next to SiC is a ternary phase or carbide phase subject to component diffusion kinetics. Reaction products such as metal-silicides and metal-carbides are produced due to mass balance requirements (equilibrium) [2]. Some of the metals which react to form silicide and carbides are Zr [25], Mo, Ta [26], Cr [27], Ti [28].

4.2 References

[1] Z. C. Feng, *SiC Power Material Devices And Application*. New York: Springer-Verlag Berline Heidelberg, 2004.

[2] J. S. Park, K. Landry, and J. H. Perepezko, "Kinetic control of silicon carbide/metal reactions," *Mater. Sci. Eng. A*, vol. 259, pp. 279–286, 1999.

[3] M Backhaus-ricoult, "Interfaces between SiC and Metals," *J. Phys. Colloq.*, vol. 51, no. C1, pp. 769–774, 1990.

[4] T. C. Chou, "Interfacial debonding by solid-state reactions of SiC with Ni and Co," *Scr. Mater.*, vol. 29, pp. 255–260, 1993.

[5] R. C. J. Schiepers, J. A. van Beek, F. J. J. van Loo, and G. de With, "The interaction between SiC and Ni, Fe, (Fe,Ni) and steel: Morphology and kinetics," *J. Eur. Ceram. Soc.*, vol. 11, no. 3, pp. 211–218, 1993.

[6] W. M. Tang, Z. X. Zheng, H. F. Ding, and Z. H. Jin, "A study of the solid state reaction between silicon carbide and iron," *Mater. Chem. Phys.*, vol. 74, no. 3, pp. 258–264, 2002.

[7] J. Pelleg, "Reactions in the matrix and interface of the Fe–SiC metal matrix composite system," *Mater. Sci. Eng. A*, vol. 269, pp. 225–241, 1999.

[8] S. W. Park, Y. I. Kim, J. S. Kwak, and H. K. Baik, "Investigation of Co/SiC Interface Reaction," *J. Electron. Mater.*, vol. 26, no. 3, pp. 172–177, 1997.

[9] T. C. Chou, "High temperature interfacial reactions of SiC with metals," *J. Vac. Sci. Technol. A Vacuum, Surfaces, Film.*, vol. 9, no. 3, p. 1525, 1991.

[10] F. J. J. van Loo and A A. Kodentsov, "Interfacial chemistry: reactions in inorganic systems," *Pure Appl. Chem.*, vol. 70, no. 2, pp. 501–508, 1998.

[11] J. C. Schuster, “Physical Chemistry of Ceramic-Metal Interface Formation,” *Trans. JWRI*, vol. 23, no. 2, pp. 142–147, 1994.

[12] E. G. Njoroge, “Solide-state interaction between Zr thin films and SiC,” University of Pretoria, 2014.

[13] M. L. Hattali, S. Valette, F. Ropital, G. Stremsdoerfer, N. Mesrati, and D. Tréheux, “Study of SiC-nickel alloy bonding for high temperature applications,” *J. Eur. Ceram. Soc.*, vol. 29, no. 4, pp. 813–819, 2009.

[14] R. Warren and C. H. Andersson, “Silicon Carbide Fibres and their Potential for use in Composite Materials . Part II,” *Compos. Part A Appl. Sci. Manuf.*, vol. 15, pp. 101–111, 1984.

[15] B. Drevet, S. Kalogeropoulou, and N. Eustathopoulos, “Wettability and interfcacial bonding in Au-Si/SiC system,” *Acta Met. mater.*, vol. 41, no. 11, pp. 3119–3126, 1993.

[16] P. Nikolopoulos, S. Agathopoulos, and G. N. Angelopoulos, “Wettability and interfacial energies in SiC-liquid metal systems,” *J. Mater. Sci.*, vol. 27, pp. 139–145, 1992.

[17] B. K. Nogi and K. Ogino, “Wettability of SiC by Liquid Pure Metals,” *Trans. Japan Inst. Met.*, vol. 29, no. 9, pp. 742–747, 1988.

[18] C. Rado, S. Kalogeropoulou, and N. Eustathopoulos, “Bonding and wetting in non-reactive metal/SiC systems: weak or strong interfaces?,” *Mater. Sci. Eng. A*, vol. 276, no. 1–2, pp. 195–202, 2000.

[19] M. Naka, T. Fukai, and J. C. Schuster, “Interfacial structures and diffusion path in SiC-metal couples,” *Surfaces, Interfaces Sci. Ceram. Join.*, vol. 158, pp. 19–27, 2006.

[20] T. Okamoto, “Interfacial structure of metal-ceramic joints.,” *ISIJ Int.*, vol. 30, no. 12, pp. 1033–1040, 1990.

[21] G. W. Liu, M. L. Muolo, F. Valenza, and A. Passerone, “Survey on wetting of SiC by molten metals,” *Ceram. Int.*, vol. 36, no. 4, pp. 1177–1188, 2010.

[22] T. C. Chou, A. Joshi, and J. Wadsworth, “Solid state reactions of SiC with Co, Ni, and Pt,” *J. Mater. Res.*, vol. 6, no. 4, pp. 796–809, 1991.

[23] I. Tsiaoussis, N. Frangis, C. Manolikas, and T. A. Nguyen Tan, “The growth of Pd thin films on a 6H-SiC(0001) substrate,” *J. Cryst. Growth*, vol. 300, no. 2, pp. 368–373, 2007.

[24] T. Iseki, T. Kameda, and T. Maruyama, “Interfacial reactions between SiC and aluminium during joining,” *J. Mater. Sci.*, vol. 19, no. 5, pp. 1692–1698, 1984.

[25] E. G. Njoroge, C. C. Theron, J. B. Malherbe, and O. M. Ndwandwe, “Kinetics of solid-state reactions between zirconium thin film and silicon carbide at elevated temperatures,” *Nucl. Instruments Methods Phys. Res. Sect. B Beam Interact. with Mater. Atoms*, vol. 332, pp. 138–142, 2014.

[26] K. M. Geib, C. Wilson, R. G. Long, and C. W. Wilmsen, “Reaction between SiC and W, Mo, and Ta at elevated temperatures,” *J. Appl. Phys.*, vol. 68, no. 6, pp. 2796–2800, 1990.

[27] K. Bhanumurthy and R. Schmid-Fetzer, “Interface reactions between silicon carbide and metals (Ni, Cr, Pd, Zr),” *Compos. Part A Appl. Sci. Manuf.*, vol. 32, no. 3–4, pp. 569–574, 2001.

[28] F. Goesmann and R. Schmid-Fetzer, “Metals on 6H-SiC: contact formation from the materials science point of view,” *Mater. Sci. Eng. B*, vol. 46, no. 1–3, pp. 357–362, 1997.

Chapter 5 : Previous studies on W-SiC

Numerous studies have been conducted to study the interaction between W and SiC for different applications such as, in nuclear reactors [1], in the semiconductor industry W is used as electrical contacts in SiC [2], to improve material strength [3], etc. All the studies conducted have contributed significant improvement in different fields of application. Before discussing the findings of this study, a brief review of previous studies is highlighted in this chapter.

Goesmann and Schmid-Fetzer [4] investigated the stability of W electrical contacts on 6H-SiC by looking at interface reactions and interface microstructure. They used DC-sputtering to deposit W thin film of 150 nm on 6H-SiC. The samples were then vacuum annealed for 4 – 29 days and analysed using scanning electron microscopy (SEM), energy dispersive X-ray analysis (EDX) and X-ray diffraction (XRD). The XRD results showed that the as-deposited samples contained mainly W_5Si_3 with some traces of W_2C, WSi_2 and WC indicating that W-SiC reacted during deposition. No changes in the phases present were observed after annealing the as-deposited samples at 1000 °C. Annealing at 1300 °C led to an increase of WSi_2 and WC phases at the interface, which resulted in the decrease of the W_5Si_3 phase composition at the interface.

A smooth layer was observed from the SEM image after annealing at 1000 °C. The W thin film layer after annealing the samples grew in a cellular morphology fashion. This caused the

W thin film contact during annealing (above 1200 °C) to break into small islands. The carbides formed next to SiC while the silicides formed next to the W ($W/W_5Si_3/WC/SiC$).

Goesmann and Schmid-Fetzer [5] repeated the study done in ref [4], using the same conditions. The study indicated that W only started to react with SiC at temperatures above 1200 °C with adhesion problems and islands formation at the surface at 1200 °C. In ref [4] the as-deposited samples had already reacted to form silicides and carbides. Annealing at 1000 °C indicated no change in the samples (the samples were still the same as the as-deposited sample). A change (reaction) was only observed after annealing at 1300 °C. The cause of the discrepancies might have been the way the samples were handled (prepared) during the two studies.

Baud *et al*. [2] deposited W (500 nm) thin film on β-SiC using CVD. They used XRD, Rutherford backscattering spectrometry (RBS) and secondary ion mass spectrometry (SIMS) to analyse the samples. Their focus was on finding the temperature at which W-SiC is stable, for contact usage. For this purpose the as-deposited samples were annealed at 600 °C,700 °C, 850 °C, 950 °C and 1100 °C in vacuum for 1 h. A reaction between W and SiC was observed to take place at the interface at 950 °C (as shown in the RBS results indicated in figure 5-1). Annealing at 1100 °C resulted in the full reaction of the W film. The phases observed were W_5Si_3 and W_2C. From SIMS, it was observed that C firstly diffused into W to form carbides followed by the formation of silicides. The thermodynamic studies (ternary phase diagram) of similar investigation showed that the two phases were not stable at 950 ° and 1100 ° temperatures. W did not react with SiC at the temperature of 800 °C and below when vacuum annealed for 1 h.

Lundberg and Östling [6] conducted a similar study to Baud *et al*., whereby W thin films of 162 nm and 125 nm were deposited on SiC using CVD. The samples were then vacuum annealed and analysed with XRD, RBS, X-ray photoelectron spectroscopy (XPS) and transmission electron microscopy (TEM). No reaction took place after annealing the sample at 800 °C and these results are in agreement with the Baud *et al*. results.

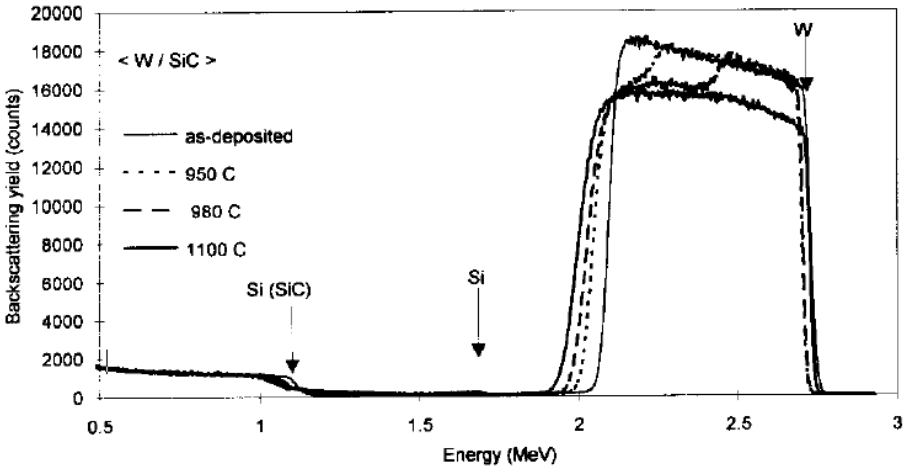

Figure 5-1: *The RBS spectra of the before and after annealing of a W thin film deposited on β-SiC, taken from [2].*

Geib *et al*. [7] also investigated the stability of W-SiC contacts at elevated temperatures. They sputter deposited W (50 nm) on SiC and the samples were annealed in vacuum for 30 min. Auger sputter depth profiling was used to analyse the samples. The as-deposited samples contained a thin interface reaction zone which was composed of WC and WSi_2. After annealing from 800 to 850 °C for 30 min, an increase in the quantity of silicides was observed as seen in figure 5-2. The surfaces of the samples remained the same before and after annealing.

The observed reactions in the deposited samples were speculated to be due to the damage in on the surface area caused by the ion milling of the SiC substrate, making the bonds weak

between Si and C and allowing reactions at very low temperature. Seng and Barnes [8] suggested that the type of deposition used (electron beam deposition) by Geib *et al*. might have been the cause of the seen reactions between W and SiC on the as-deposited samples. It has been observed that different reactions between layers deposited by sputter deposition and those deposited by thermal heating deposition. The explanation is that this is due to the slightly higher arrival energy of the atoms in sputter deposition compared to thermal heating deposition. The reaction of W with SiC on the as-deposited samples was also observed by Goesmann and Schmid-Fetzer [4].

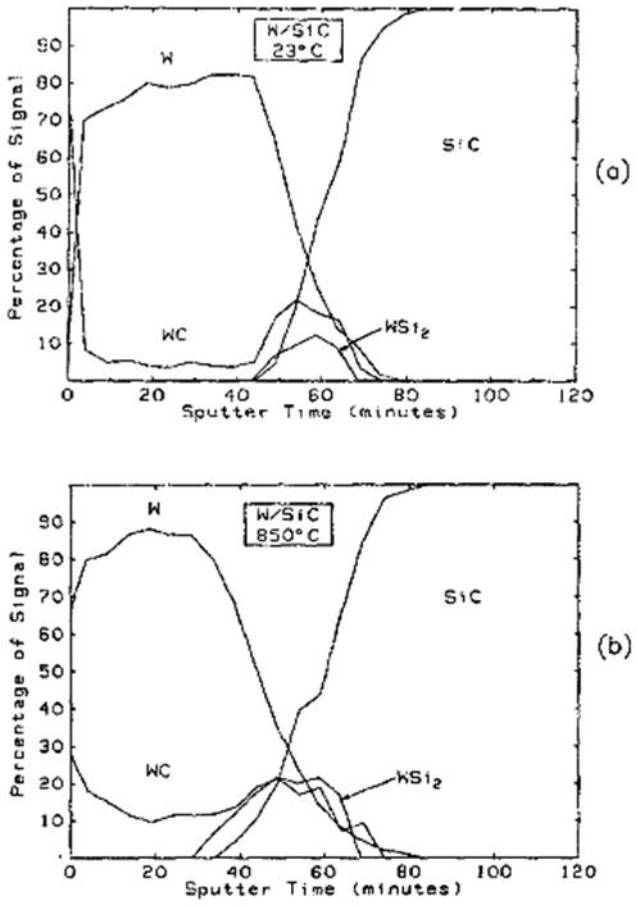

Figure 5-2: *The Auger depth profiles of W thin films sputter deposited on β-SiC (a) as-deposited and (b) after vacuum annealing at 850 °C for 30 min, taken from [7].*

Rogowski and Kubiak [9] investigated the dependence of electrical properties of W contacts deposited on SiC (using magnetron sputter deposition). They looked at the structural changes and chemical composition of the contacts at the interface after annealing. XRD, SEM and SIMS were used to analyse the deposited samples before and after annealing. The samples were annealed in an Ar atmosphere from 700 °C to 1600 °C for 10 min. The resulting phases after annealing at 700 °C were W_5Si_3 and WSi_2. The appearance of WC at 1400 °C at the expense of WSi_2 was also observed. A smooth surface layer with a well-defined (clearly distinguishable) continuous W layer was observed on the as-deposited samples and the samples annealed up to 1200 °C. While a rough surface (non-uniform) with the formation of pores was observed at 1400 °C, see figure 5-3.

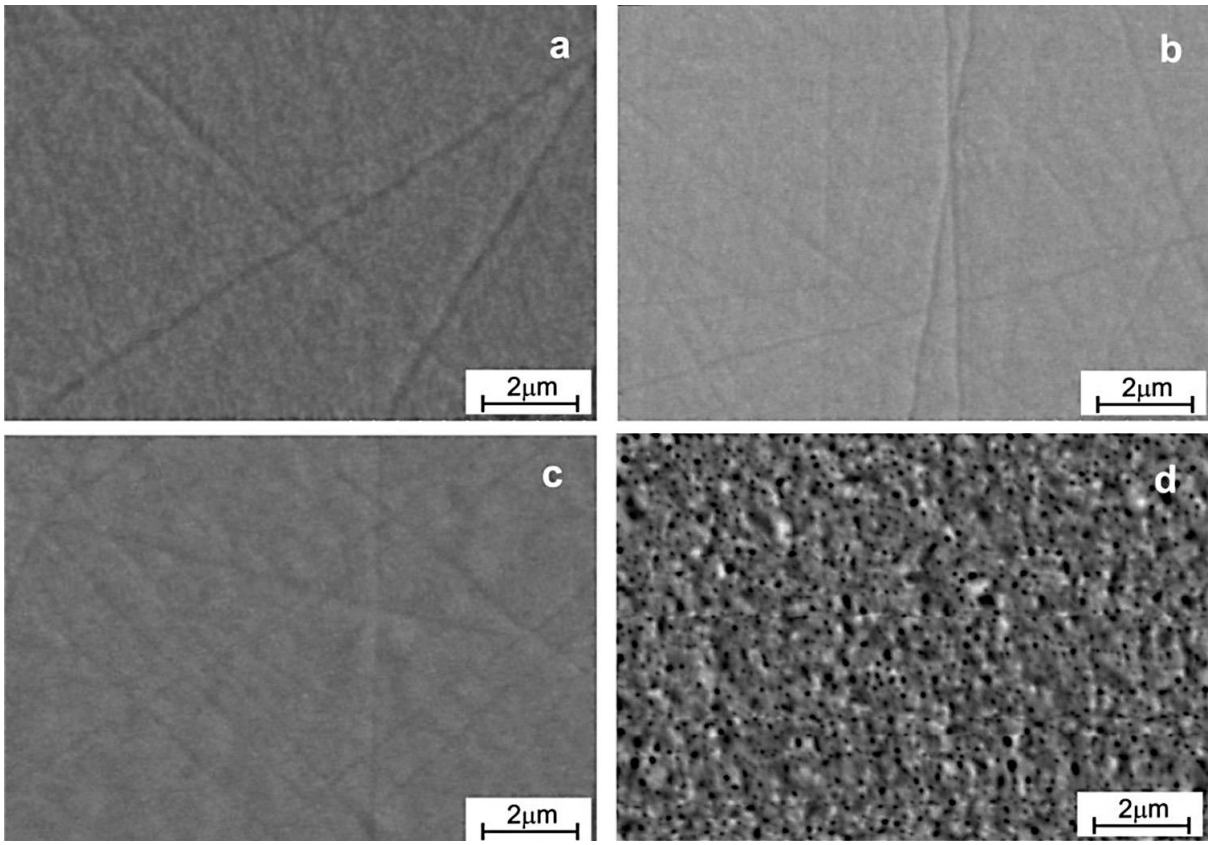

***Figure 5-3**: SEM images of W-SiC (a) as-deposited, (b) 1000 °C, (c) 1200 °C and (d) 1400 °C, taken from [9].*

Guo *et al*. [10] reported on the microstructure characterization of W-SiC by mainly focusing on the W-SiC interface and the change in the different sublayers. The W was chemically vapour deposited on the SiC. SEM cross section and TEM were used to analyse the deposited samples. A reaction zone (RZ) consisting of W_2C, W_5Si_3 and WC was observed (see figure 5-4 (a)) after deposition. The formation of the W_2C was explained to be due to the diffusion of C from the carbon coating layer. As shown in figure 5-4 (b), there was a C coating layer on the surface of the SiC sheath.

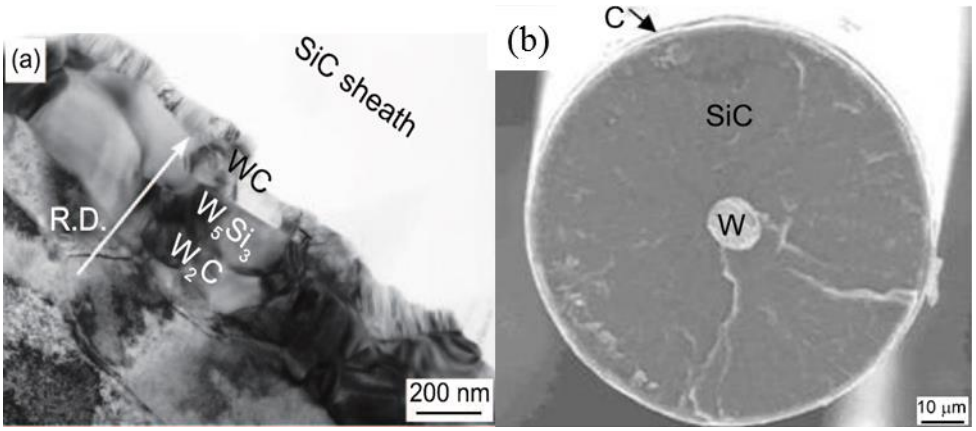

Figure 5-4: *(a) TEM image of the W-SiC displaying the interfacial reaction zone and the phases present (b) SEM cross sectional image of the W-SiC sample image. [10]*.

Toplišek *et al*. [3] conducted a study on the interaction between W deposited on 6H-SiC. Their aim was to study the potential interaction between the W and SiC fibers. They wanted to see if the W-SiC will improve thermal conductivity of SiC-SiC composites. They conducted the study by using SEM, energy-dispersive X-ray spectroscopy (EDXS) and TEM in order to monitor the microstructural changes and possible phases formed. The samples were annealed at 1600 °C in an Ar atmosphere for 3 hours. The as-prepared sample was composed of W in a form of nano-size grains and the interface between W and SiC was smooth. After annealing the samples, a rough W-SiC interface with large circular pores and traces of oxygen and calcium were observed using SEM/EDXS. The phases formed after

annealing were reported to be W_3Si, W_5Si_3 and W_2C (see Figure 5-5). The phases were identified using EDX, electron diffraction and the W-Si-C ternary phase diagram (1800 °C).

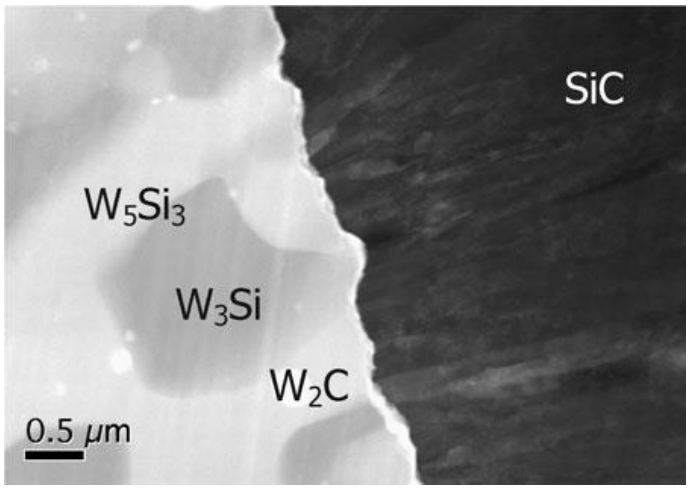

Figure 5-5: *STEM/HAADF (Z-contrast) micrograph of W/SiC interface after annealing in Ar at 1600 °C for 3 h, taken from [3].*

Burykina *et al*. [11] investigated the interaction of silicon carbide with refractory metals, tungsten being one of the metals, compacted with SiC. In this study they annealed the samples in vacuum for 2h at temperatures ranging from 1200 °C to 2000 °C. The initial reaction was reported to be at 1500 °C. The reactions at these annealing temperatures increased the reaction zone width. The interface became brittle and porous due to the increase in annealing temperature and the reaction at the W-SiC interface to form new phases).

Son *et al.* [12] investigated the solid state reaction of hot pressed (1700-1900 °C) W-SiC (in situ joining of W-SiC) for plasma facing components. Figure 5-6 taken from their results, shows the cross-sectional SEM images. A reaction zone (called reaction layer in Figure 5-6) was observed and its thickness increased with processing temperature. The W grain size also increased with the increase in temperature. The RZ at 1700 °C consisted of WSi_2, WC and W_2C as the initial phases formed. At 1780 °C WSi_2 had completely disappeared with the formation of W_5Si_3. W_2C and W_5Si_3 were the dominant and stable phases (1780-1900 °C).

WC was observed to be decreasing in quantity with the increase in processing temperature. The phase arrangement between SiC and W observed along the reaction zone was $SiC/WSi_2/WC/W_5Si_3/W_2C/W$.

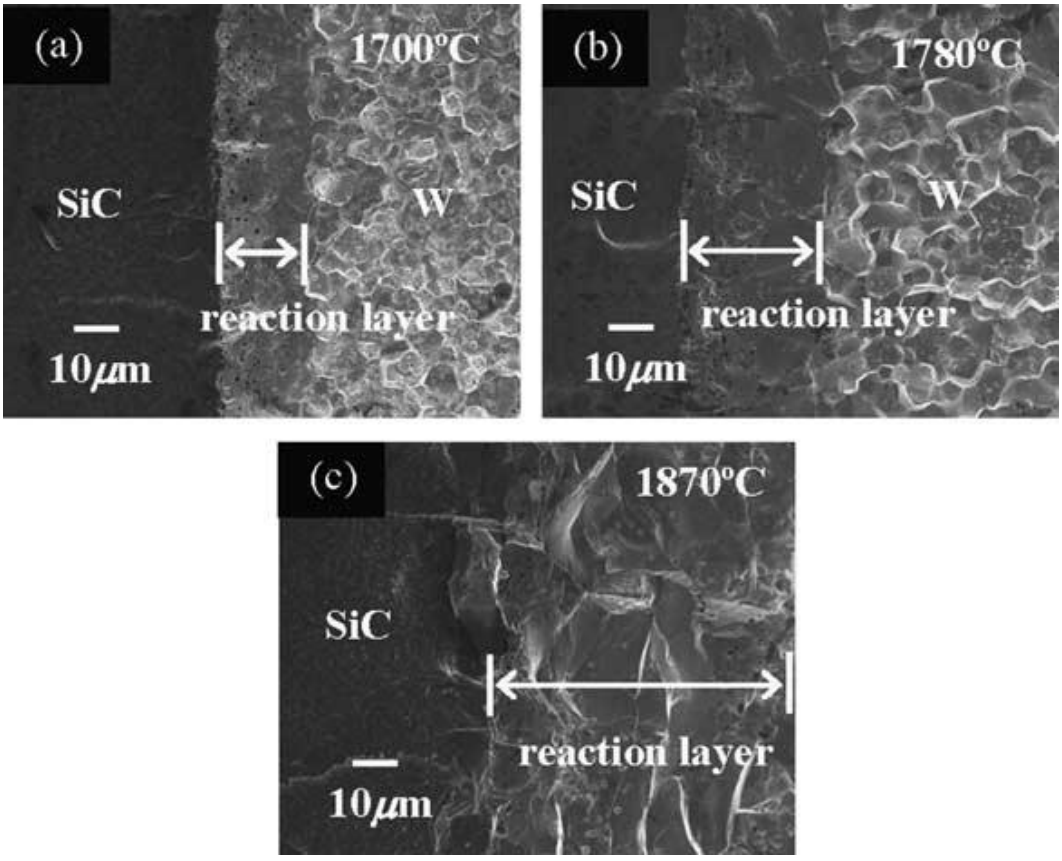

Figure 5-6: *SEM cross-section of the processed W-SiC at different temperatures [12].*

Lee *et al*. [13] studied the effect of adding SiC nanowires with W powder to form composites and investigated the interface microstructure and mechanical properties. The SiC nanowires and W powder were fused by a spark plasma sintering process and heated at 1700 °C for 3 min to form composites under vacuum. XRD and TEM were used to analyse the samples. W_2C and W_5Si_3 phases (detected by XRD) were formed by the reaction between SiC and W during the sintering process.

Gao *et al*. [14] reported on the dependence of fracture toughness and bending strength on the thickness of the SiC-W materials. W was sprayed on SiC and the W-SiC was hot pressed at 1700 °C for 2h to another W-SiC sample. Using XRD, WC and W_5Si_3 were detected on these hot pressed samples. The fracture toughness increased with the increase in thickness of the W metal, while the bending strength was reduced.

Kishimoto *et al.* [15] also investigated the bonding strength between W and SiC for use in gas-cooled fast fission reactors (GFR). Tungsten was chosen to protect the SiC ceramic, which is used for the cladding tubes in the GFR. In their research W was hot pressed to SiC at 1600 °C for 1h. The joining of W and SiC was explained to be possible due to the diffusion taking place between W and SiC. A uniform reaction layer was formed, with carbon, yttrium, aluminium and oxides affecting the bonding between W-SiC. They suggested that the presence of oxides produced the bonding strength of W-SiC joint.

Kishimoto *et al*. [1] repeated the study of the bonding strength of between W and SiC further. In this study they used three different bonding methods to evaluate the W-SiC microstructure of diffusion and sinter bonding between W and SiC. SEM, TEM, EDX and electron probe micro analyzer (EPMA) were used for analysis. Diffusion bonding (1600 °C, 10h) resulted in the formation of columnar phase tungsten silicide being formed due to volume diffusion at the interface and the interface was crystalline. The second method was sinter bonded W-SiC joints. The interface in this case was composed of uniform silicon oxide layer. And it was believed to be formed by a volume diffusion mechanism. The oxygen was speculated to be from tungsten oxide. They stated that the presence of the oxide layer compromises the W-SiC, allowing easy reactions to take place between W and SiC. The third method was: liquid phase sinter, were Ni was added on the W powder. The bonded W-SiC

resulted in the formation of 4 different layers which were not amorphous. They believed that the 4 layers existed because Si was bonded with oxygen and the Ni bonded with oxygen (Ni was present in the W layer). Similar results were also obtained by obtained by Matsuo *et al.* [16].

Seng and Barns [8] carried out a theoretical study to investigate the stability of W-SiC in ternary systems. In general, when calculating Gibbs free energy (ΔG) for phase diagrams from the expression $\Delta G = \Delta H - T\Delta S$ an assumption that ΔG is equal to the enthalpy (ΔH) [$\Delta G \approx \Delta H$] is made. This assumption is correct at low temperatures. But at high temperatures entropy (ΔS) can cause a change in the ΔG. Thus the expected reaction via enthalpic consideration only, will be different from the observed ones. Hence Seng and Barns decided to take ΔS into account when calculating ΔG. They plotted the phase diagrams from their ΔG calculation and reported on the phases to be expected at different temperatures. Their ternary phase diagram indicated that at low temperatures (300 K < T < 970 K) WSi_2 and WC are stable with SiC. They are expected to be the initial phases which form due to favourable kinetics. Increasing the temperature (970 K < T < 2140 K) changed the stable silicide with SiC to W_5Si_3, resulting in W_5Si_3 and WC phases. At temperatures of 2140 K < T < 2200K WC changed to W_2C, making W_5Si_3 and W_2C to be stable with SiC.

The Ellingham diagram of the reactions between W and SiC (labelled 1 to 6) are represented in figure 5-7 below. The diagrams show the possible reactions expected at a given temperature, and also indicate the silicide and carbide stable with SiC in each reaction. For example, the reaction labelled 1 and 2 in figure 5-7 (a) have positive ΔG at temperatures below 1700 K and 950 K respectively. The reactions are not expected to occur below these temperatures. At temperatures from 300 to 2200 K, W reacts with SiC. In the reaction

labelled 3 in figure 5-7 (a), a reaction between W and SiC producing WSi_2 and WC is observed.

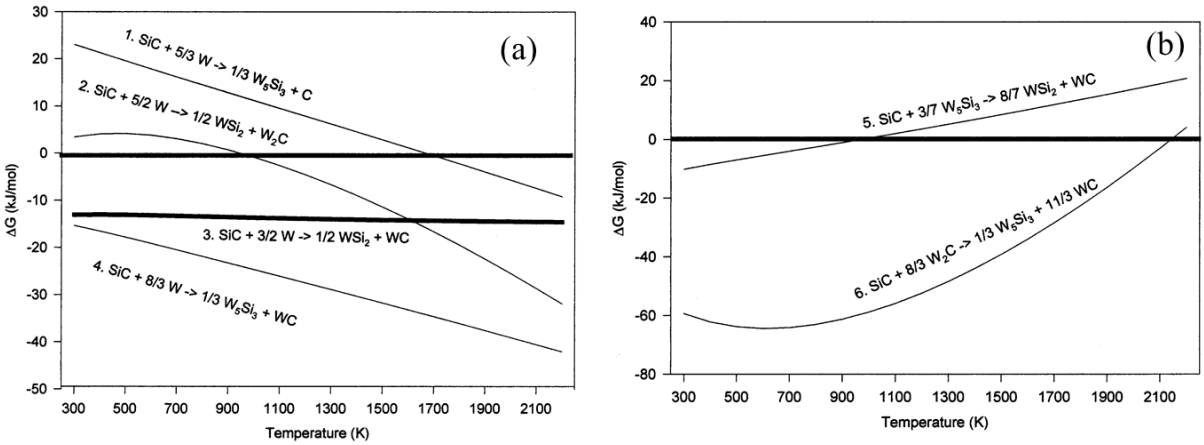

Figure 5-7: *Ellingham diagrams of reactions between new products at elevated temperatures W-SiC (a), reactions leading to formation of new phases (b) critical reactions that change the stable phases as a function of temperature, taken from [8].*

The reaction labelled as 4 indicates that W reacts with SiC to form W_5Si_3 and WC. Reaction 4 is the most likely reaction to occur (from reaction of W and SiC directly) as indicated by the decrease in ΔG with increase in annealing temperatures. The transition state theory states that when comparing similar reactions, the reaction with the lowest ΔG is kinetically more favourable. Thus reaction 4 will be the favourable reaction from the reactions labelled 1 to 4. The reaction labelled 5 in figure 5-7 (b) indicates that W_5Si_3 reacts with SiC to form WSi_2 and WC. The ΔG becomes positive at temperature above 970 K, which means W_5Si_3 reacts with SiC until 2140 K. This reaction is responsible for the change in the silicide (WSi_2 to W_5Si_3) stable with SiC at 970 K (in the W-Si-C ternary diagram). The formation of the carbide as a function of temperature is governed mainly by reaction labelled 6 (figure 5-7 (b)). From the figure 5-7 W_2C reacts with SiC to form WC, until 2140 K (where ΔG is

positive). This equation is that responsible for the change in stable carbide from WC to W_2C at 2140 K .

Different researchers as stated above studied the reaction between W and SiC and reported on their findings. Geib's [7] results indicated a reaction taking place between W and SiC during room temperature deposition to form WSi_2 and WC. The phases observed by Geib are in agreement with the ternary phase diagram reported by Seng and Barnes [8]. The expected phases from room temperature to 700 °C are WSi_2 and WC which are stable with SiC. Rogowski [9] after annealing in Ar at 700 °C observed only silicides (WSi_2 and W_5Si_2) as initial phases no carbide present. Baud [2] and Goesman [5] both annealed in vacuum but observed reactions at different temperatures. Baud observed the initial reaction at 950 °C resulting in the formation of W_5Si_3 and W_2C. Goesman et al. [4], [5] reported the initial reaction to be at 1300 °C with the formation of WSi_2 and WC. These results indicate that one should expect the initial reaction to take place at a lower temperature in Ar annealed samples than in vacuum annealed samples. The silicide (W_5Si_3) observed by Baud [2] and Rogowski [9] (at the annealing temperatures which were reported) are in agreement with the W-Si-C ternary phase diagram at 970 K < T < 2140 K. The carbide (WC) reported by Goesman [4], [5] and Rogowski et. al. [9] are in agreement with the ternary phase diagram for 970 K < T < 2140 K.

5.1 References

[1] H. Kishimoto, T. Shibayama, K. Shimoda, T. Kobayashi, and A. Kohyama, "Microstructural and mechanical characterization of W/SiC bonding for structural material in fusion," *J. Nucl. Mater.*, vol. 417, no. 1–3, pp. 387–390, 2011.

[2] L. Baud, C. Jaussaud, R. Madar, C. Bernard, J. S. Chen, and M. A. Nicolet, "Interfacial reactions of W thin film on single-crystal (001) β-SiC," *Mater. Sci. Eng. B*, vol. 29, no. 1–3, pp. 126–130, Jan. 1995.

[3] T. Toplisek, M. Gec, A. Ivekovic, S. Novak, S. Kobe, and G. Drazic, "Analytical Electron Microscopy of W-Core b-SiC Fibers for Use in an SiC-Based Composite Material for Fusion Applications," *Microsc. Microanal.*, vol. 19, no. S5, pp. 136–139, 2013.

[4] F. Goesmann and R. Schmid-Fetzer, "Stability of W as electrical contact on 6H-SiC: phase relations and interface reactions in the ternary system W-Si-C," *Mater. Sci. Eng. B*, vol. 34, no. 2–3, pp. 224–231, 1995.

[5] F. Goesmann and R. Schmid-Fetzer, "Metals on 6H-SiC: contact formation from the materials science point of view," *Mater. Sci. Eng. B*, vol. 46, no. 1–3, pp. 357–362, 1997.

[6] N. Lundberg and M. Ôstling, "Chemical Vapor Deposition of Tungsten Schottky Diodes to 6H-SiC," *J. Electrochem. Soc. Act.*, vol. 143, no. 5, pp. 1662–1667, 1996.

[7] K. M. Geib, C. Wilson, R. G. Long, and C. W. Wilmsen, "Reaction between SiC and W , Mo , and Ta at elevated temperatures," *J. Appl. Phys.*, vol. 68, no. 6, pp. 2796–2800, 1990.

[8] W. F. Seng and P. A. Barnes, "Calculations of tungsten silicide and carbide formation on SiC using the Gibbs free energy," *Mater. Sci. Eng. B*, vol. 72, pp. 13–18, 2000.

[9] J. Rogowski and A. Kubiak, “Effects of annealing temperature on the structure and electrical properties of tungsten contacts to n-type silicon carbide,” *Mater. Sci. Eng. B*, vol. 191, pp. 57–65, Jan. 2015.

[10] C. Guo, C. Zhang, L. He, B. Jin, and N. Shi, “Microstructure Characterization of Long W Core SiC Fiber,” *J. Mater. Sci. Technol.*, vol. 23, no. 5, pp. 677–684, 2007.

[11] A. L. Burykina, L. V. Strashinskaya, and T. M. Evtushok, “Investigation of the interaction of silicon carbide with refractory metals and oxides,” *Sov. Mater. Sci.*, vol. 4, no. 3, pp. 220–223, 1970.

[12] S. J. Son, K. H. Park, Y. Katoh, and A. Kohyama, “Interfacial reactions and mechanical properties of W–SiC in-situ joints for plasma facing components,” *J. Nucl. Mater.*, vol. 329–333, pp. 1549–1552, Aug. 2004.

[13] D. Lee, H. Park, H. Ryu, S. Jeon, and S. Hong, “Microstructure and mechanical properties of SiC-nanowire-augmented tungsten composites,” *J. Alloys Compd.*, vol. 509, no. 37, pp. 9060–9064, 2011.

[14] Y. Gao, S. Zheng, and K. Zhu, “Analysis of mechanical properties and SEM for laminated SiC/W composites,” *Mater. Lett.*, vol. 50, no. 5–6, pp. 358–363, Sep. 2001.

[15] H. Kishimoto, T. Shibayama, T. Abe, K. Shimoda, S. Kawamura, and A. Kohyama, “Diffusion Bonding Technology of Tungsten and SiC/SiC Composites for Nuclear Applications,” *IOP Conf. Ser. Mater. Sci. Eng.*, vol. 18, no. 16, p. 162015, Oct. 2011.

[16] G. Matsuo, T. Shibayama, H. Kishimoto, K. Hamada, and S. Watanabe, “Micro-chemical analysis of diffusion bonded W-SiC joint,” *J. Nucl. Mater.*, vol. 417, no. 1–3, pp. 391–394, 2011.

Chapter 6 : Experimental Procedure

6.1 Samples Preparation.

The material used in this study was single crystalline 6H-SiC purchased from *Pam-Xiamen*, China. The bulk semi-insulating wafers were single-face polished with Si epiready, 2 inch diameter, 330 μm thick, with a micropipe density of < 30 cm^{-2} and a root mean square (RMS) surface roughness of < 0.5 nm. Before deposition, the samples were cleaned in an ultrasonic bath using trichloroethylene (10 min), 10 % of hydrochloric acid (5 min), and hydrofluoric (HF) acid (10 min), after each step the sample were rinsed in de-ionised water. Finally the water was blown with nitrogen gas. The cleaning was done to remove contaminations and oxides present on the surface. W metal purchased from *AJA international Inc*., Scituate, Massachusetts was deposited on the samples. The W metal was in the form of a sputtering target which was 2 inches in diameter and 0.25 inches thick with 99.95 % purity. After deposition the wafer was cut into smaller samples roughly 5 × 5 mm^2 size using a diamond scriber. The process of sample preparation and analysis is illustrated in figure 6-1.

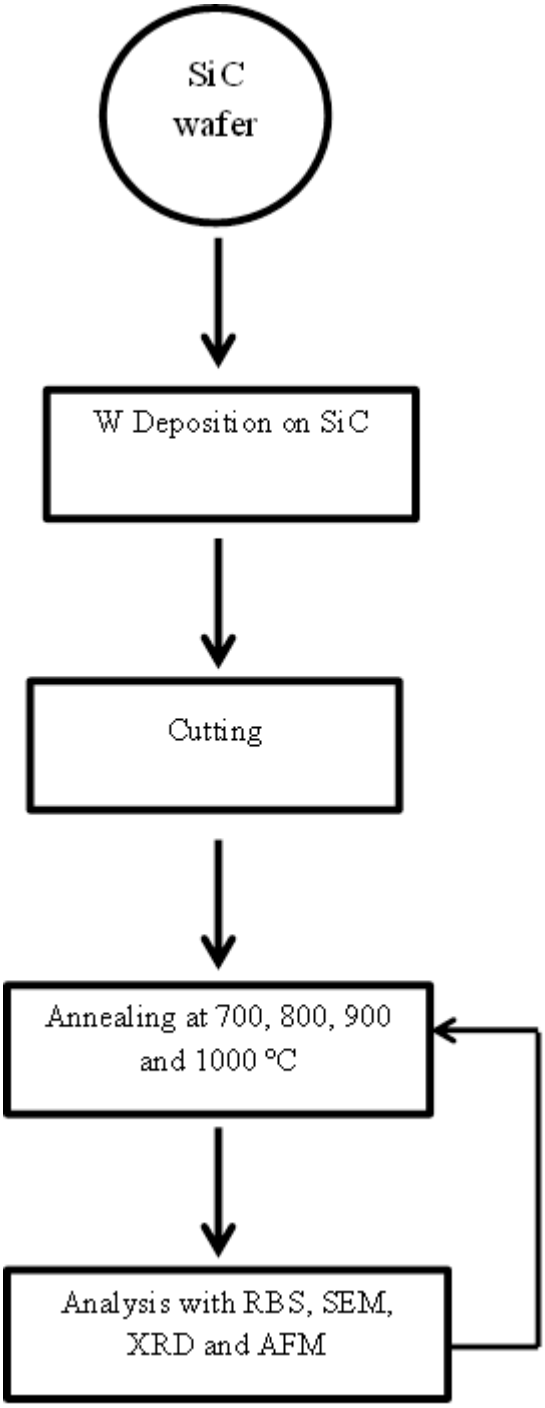

Figure 6-1: *A schematic diagram of sample preparation and analysis technique.*

6.1.1 Sputter Deposition

A deposited film is formed by atoms which are directly transported from source to the substrate through gaseous phase during the deposition process [1]. The film must be vaporized from its

solid form in order to be able to deposit. One of the common forms of physical vapour deposition (PVD) deposition techniques is sputtering. The common use of sputter deposition is owing to the good adhesion to the substrate, smoother surface at low deposition temperatures and results in uniform deposited layer.

Sputter deposition occurs when atoms are dislodged from the surface of a material (target) as a result of collision with high-energy particles (fast moving Ar^+ gas bombarding the target) as can be seen in figure 6-2. Atoms are ejected from a target material by the high-energy particle bombardment. The ejected atoms can condense on a substrate covering the whole surface of the substrate as a thin film. Sputtering is also used for cleaning of the surface because it involves etching of surface atoms.

The process of sputtering is categorized into direct current (DC), radio frequency (RF), magnetron and reactive sputtering. The characteristic of the target material determines which process can be used between DC and RF sputtering. DC diode (see figure 6-2) is used for electrically conductive materials, such as metals. In this configuration, a cathode (target) is needed to sustain the glow discharge and is made of the material to be deposited. It is normally placed at a negative potential relative to an anode. The anode contains the substrate and it is connected to the ground.

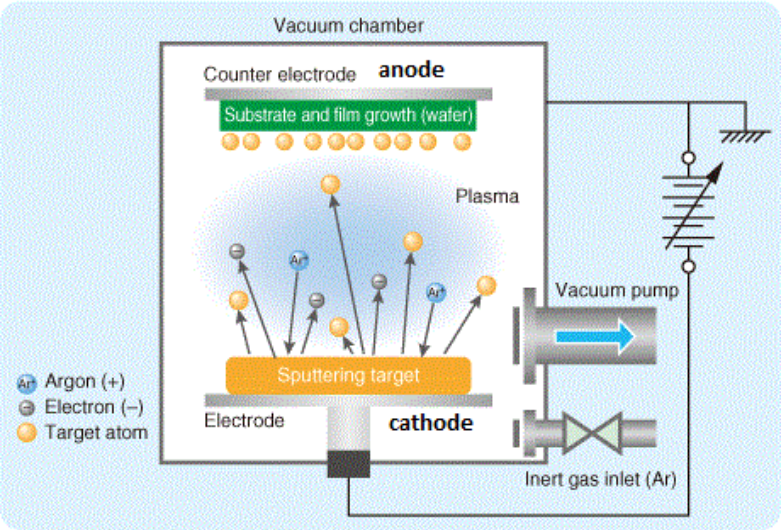

Figure 6-2: *Schematic diagram of a DC sputter deposition, taken from [2].*

The disadvantage of DC sputtering is that it cannot be used to sputter non-conducting targets. In the case of insulators and semiconductors, accumulation of the surface charge occurs at the target which cannot be electrically conducted away and prevents ion bombardment [3]. RF sputtering is a technique that uses the application of an AC voltage to the electrodes so that the replacement of the lost electrons to the insulator surface is possible [4][5]. This makes sputter deposition of insulators and semiconductors possible. With the RF sputtering setup, a potential is capacitively coupled to an electrode and the power supply is operated at high frequency, typically around 13.56 MHz or multiples of 2 or 3 of it [1][4]. The cathode and anode terminal polarities are electrically reversed for a fraction of the RF cycle; this is done to eliminate the charge build up [6].

In this study, the AJA Inc. Orion 5 sputtering system (Figure. 6-3) was used to deposit the W thin on a 6H-SiC wafer. A rotating sample holder was used to mount the SiC wafer to make sure that a uniform deposition layer was obtained. The target to substrate distance was set at 34 mm. To remove gasses, water vapor and metallic contaminates from the chamber, it was

degassed. The degassing was achieved by heating the chamber to about 500 ºC for 1 hour while evacuating. After degassing, the chamber was pumped down to a base pressure of 10^{-6} Torr. At this pressure, the chamber was filled with Ar gas to a pressure of about 10^{-3} Torr. The Ar flow rate was 10 SCCM. The cathode voltage was 382 V and the current was 0.26 A during the W target sputtering.

The W target and SiC substrate *in-situ* cleaning was done inside the sputtering chamber to prevent recontamination between the cleaning and deposition processes. The cleaning was done for 10 min using Ar plasma for the W target (DC sputtering) and the SiC substrate (RF sputtering) before the RT deposition was performed. The in-situ cleaning was done to remove any present contamination (oxides, metallic or organic contaminants) on the SiC substrate and W target, since W reacts easily with oxygen to form tungsten oxides. The W thin film sputter deposition on SiC was performed for 15 min and the thickness of the W layer was calculated to be 73.8 nm.

Figure 6-3: *Images of AJA Inc. Orion 5 sputtering system at the University of Zululand.*

6.1.2 Annealing

In the study of solid-state reactions, annealing plays an important role which activates and accelerates the intermixing and reaction processes. Annealing also enables us to study structural modification and interfacial reaction. The deposited W-SiC sample was heated at a particular temperature for certain duration of time.

Isochronal annealing was done in this study. The samples were placed in a vacuum tube furnace with a maximum annealing temperature of 1000 °C. A schematic diagram of the annealing system is shown in figure 6-4. The sample is placed in a quartz tube close to the thermocouple, which is connected to the data acquisition, in order to measure and monitor its temperature. After inserting the sample, the quartz tube was evacuated to 10^{-3} mbar by the fore pump, and then the turbo pump system was turned on. The turbo pump provides high vacuum of approximately 10^{-8} mbar during annealing.

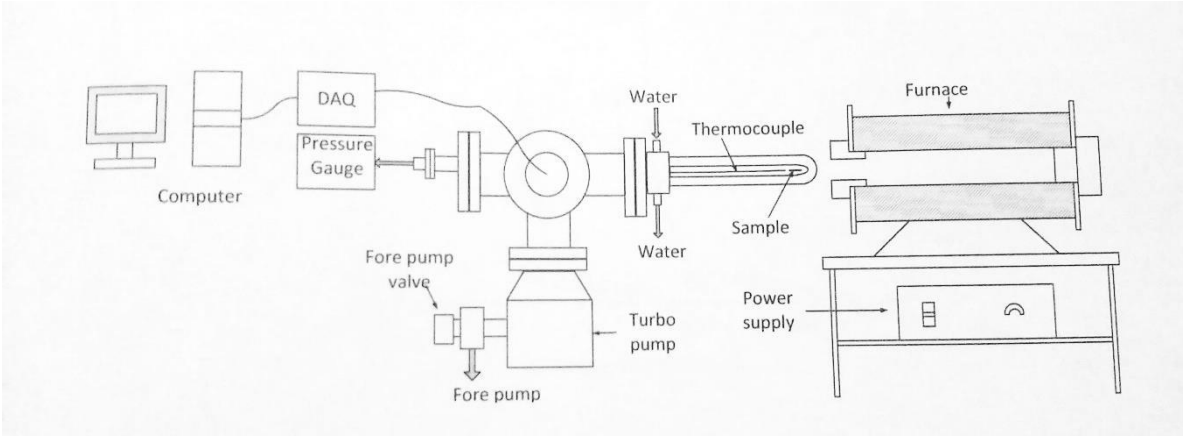

Figure 6-4: *A schematic diagram of the tube furnace annealing system, taken from [3].*

The annealing temperature was pre-set to the desired temperature, and the furnace was switched on and left to reach and stabilize at the desired temperature. The furnace was then pulled to cover

the quartz tube and to quickly heat the sample, while the data acquisition program connected to the computer was running. After the annealing was done the furnace was pulled away to allow the quartz tube to quickly cool down to RT. The samples were annealed at 500 °C, 600 °C, 700 ºC, 800 ºC, 900 ºC and 1000 ºC for 1 hour.

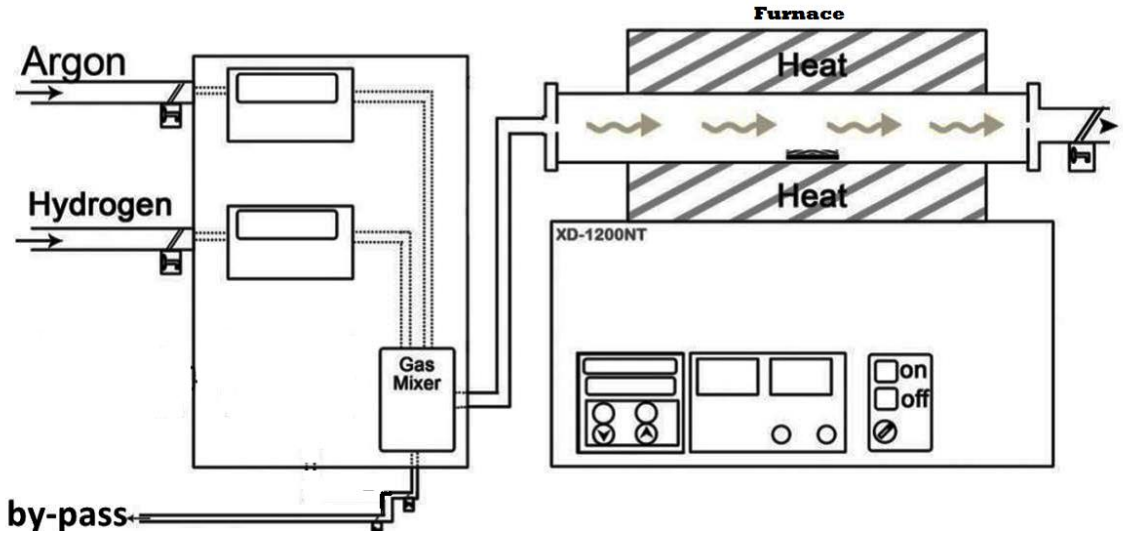

Figure 6-5: *Schematic diagram the second annealing system using argon and hydrogen gas.*

A different set of samples were annealed in argon and hydrogen at temperatures of 500 °C, 600 °C, 700 ºC, 800 ºC, 900 ºC and 1000 ºC for 60 min. The system used for annealing is illustrated in figure 6-5. The samples were placed in quartz tube which was connected to a flow meter of different gas supplies (that is Ar 99.99 % and H_2 99.99 % purity). The flow rate of H_2 was 250 SCCM and for Ar was 350 SCCM. Ar is a carrier gas and its role is to create an inert environment while H_2 (reactive gas) is used to remove most of the impurities present in the material. Annealing parameters are pre-set, to the desired annealing temperature and time (annealing takes place at atmospheric pressure), afterwards the furnace was switched and annealing to took place. A graph showing the annealing curve at 900 ºC is shown in Figure 6-6.

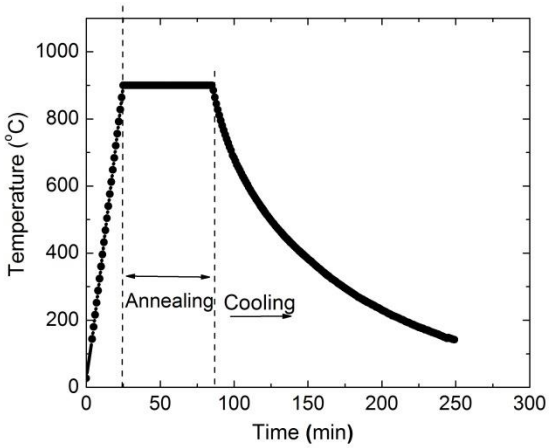

Figure 6-6: *Annealing curve for a sample annealed in H_2 for 60 min.*

6.2 Analysis Techniques

6.2.1 Rutherford Backscattering Spectrometry (RBS)

Rutherford Backscattering Spectrometry (RBS) is an ion beam analysis technique which is used for quantitative composition analysis of layers or near surface regions of solids. RBS allows non-destructive analysis of materials structure and multi-element depth profiles. It is suited for measuring heavy elements on light substrate. It can also determine the composition of the material and give information about the diffusion, interface formation and phase changes. The RBS technique is based on the principle where a mono-energetic ion beam typically $^4He^+$ of 1 to 3 MeV is projected towards a target and followed by the detection of the backscattered ions from the target at a particular angle.

When the mono-energetic ions are shot into a high vacuum scattering chamber where the target is placed, the ions will penetrate the target material and gradually slowed down. However, some of the ions undergo close collisions with target atoms resulting in a large scattering and energy transfers. From there, the projectiles are scattered back and they leave the target. The

energy of the backscattered ions is then measured from the scattering events occurring at the surface and at particular depths.

The backscattered particles will be detected by the detector, depending on the angle in which they backscattered. The detector is normally placed at an angle greater than 90^o and less than 180^o with respect to the incoming beam (as shown in figure 6-7). From these detected backscattered particles different information of the target can be deduced: possible reactions which are taking place, mass and depth distributions of the target elements, etc.

6.2.1.1 Kinematic Factor

The most important quality of RBS is its ability to determine material composition. This is due to the nature of the backscattering events where ions backscattered from atoms of different masses at the same position will possess different energies. The information about the composition of the material and masses of the atoms is obtained from the kinematic factor (*K*). The kinematic factor is a ratio of the backscattered ion/alpha particle's energy E_1 (after collision) and incident energy E_o (before the collision). If the collision is consider to be elastic, the energy of the backscattered particle (E_1) can be calculated using the principle of conversion of energy and momentum [7]–[10]:

$$E_1 = KE_0 = \left[\frac{M_1 cos\theta \pm \sqrt{M_2^2 - M_1^2 sin^2\theta}}{M_1 + M_2}\right]^2 E_0 \qquad (6.1)$$

where M_1 and M_2 are atomic masses of the projectile ion (He^+ and H^+) and target atom respectively, E_o and E_1 are the energies of the incident and backscattered particle respectively

and θ is the backscattered angle (as shown in figure 6-7). When $M_1 < M_2$ the plus sign is used in equation (6.1), while the minus sign is used when $M_1 > M_2$. In this case the plus sign is applicable because the mass of the target atom is greater than that of the alpha particles and the angle, θ, is fixed at 165º.

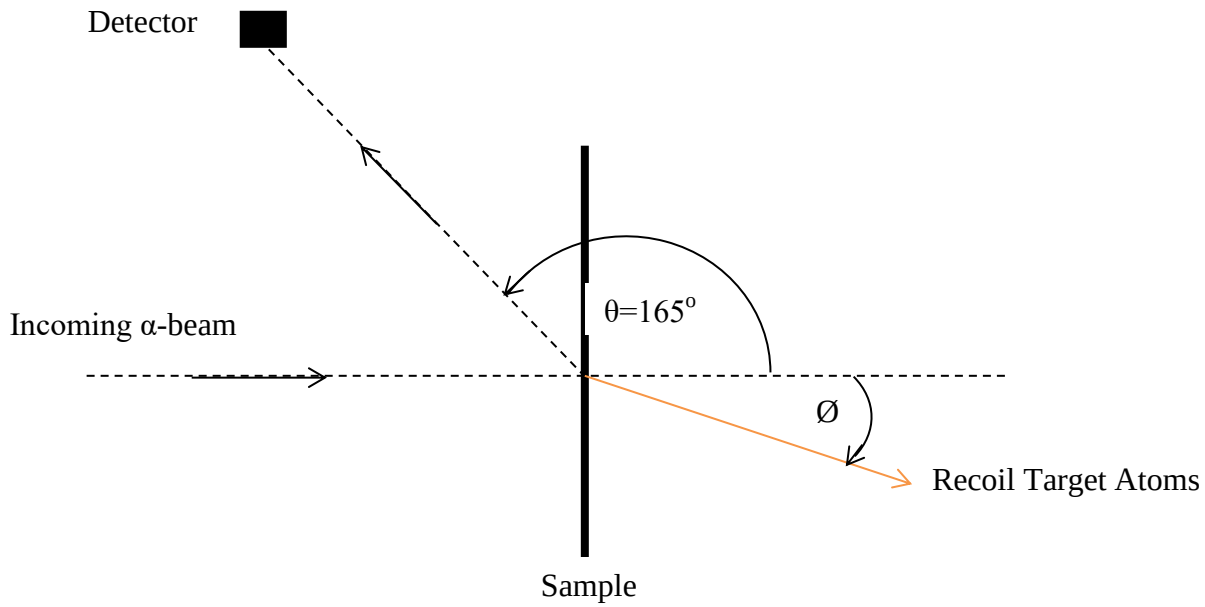

Figure 6-7: *A schematic diagram showing the RBS experimental setup at the University of Pretoria and the backscattering angle θ.*

6.2.1.2 Differential Cross Section

A small fraction of the incident beam is usually backscattered from the target atoms into the detector. The probability of the scattering to occur at the solid angle is determined by the concept differential cross section. The differential cross section for scattering ($d\sigma/d\Omega$) is defined as the number of particles backscattered into a solid angle $d\Omega$ per number of incident particles per unit area. The differential cross section for the scattering angle of a projectile into a solid angle $d\Omega$ centered around an angle θ in the laboratory coordinate system is given as [7][9][11].

$$\left(\frac{d\sigma}{d\Omega}\right)_{projectile} = \left(\frac{Z_1 Z_2 e^2}{4E_o}\right)^2 \frac{4\left(M_2 cos\theta + \sqrt{M_2^2 - M_1^2 sin^2\theta}\right)^2}{M_2 sin^4\theta \sqrt{M_2^2 - M_1^2 sin^2\theta}} \quad (6.2)$$

where Z_1 is the atomic number of the projectile with mass M_1, Z_2 is the atomic number of the target with mass M_2, E_o is the energy of the projectile before scattering, e is the electron charge and θ is the back scattering angle.

The differential cross section is directly proportional to Z_2^2 and inversely proportional to E_o, this means the RBS is more sensitive to targets with heavy elements as compared to light elements. The inverse proportionality of E_o to the differential cross section, means one would expect more counts if they are working at low energy as compared to high energies. The total number of backscattered and detected particles is given by:

$$A = \sigma \Omega Q N \quad (6.3)$$

where Ω is the detector solid angle, N the total number of atoms per unit area, Q is the total number for incident projectiles, σ is the differential cross section averaged over the surface of the detector. From equation (6.3) we can see that if $A, \sigma, \Omega \; and \; Q$ are known we can obtain N.

6.2.1.3 Depth Profiling

The backscattered particles (He^+ in this study) have different energies when scattering at different depths within the target atom. The incident particle with energy E_o backscattering at the surface, have the energy KE_o as illustrated in figure 6-9. Some of the incident particles with energy E_o lose some of their energy as they penetrate (inward) the target material. Their energy

E will not be the same as the energy E_o just before backscattering at depth x (shown in figure 6-8) [7]. The particles backscattered at depth x lose energy on their way out of the material and emerge from the surface with energy E_1 which is less than E.

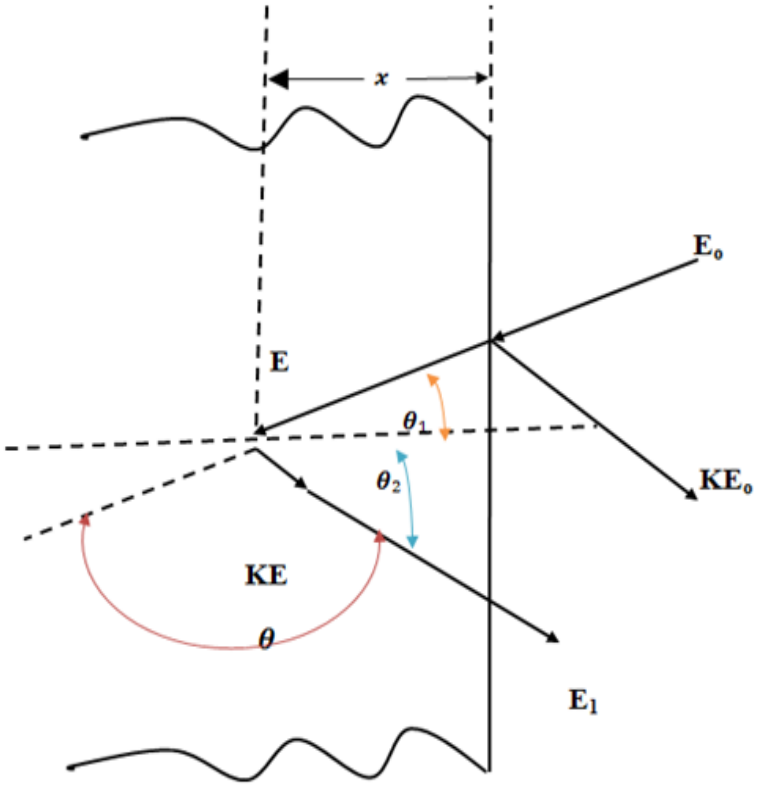

Figure 6-8: *A schematic diagram illustrating the backscattering event of alpha particles and energy loss from depth x [12].*

From figure 6-8, the inward path where the ions losses energy is given by $x/\cos\theta_1$ and the outward path (ions that backscattered at x and continue to loss energy when exiting) is given by $x/\cos\theta_2$.

The total energy loss of the particles backscattered at the surface and depth x has be derived by assuming that dE/dx has a constant value along the inward and outward paths [7][9]:

$$KE_o - E_1 = \left[\frac{K}{cos\theta_1}\frac{dE}{dx}\Big|_{in} + \frac{1}{cos\theta_2}\frac{dE}{dx}\Big|_{out}\right]x \quad (6.4)$$

where KE_o is the energy of the backscattered particles at the surface atoms of the target and E_1 is the energy of the backscattered alpha particle from the atom at depth x.

If we take ΔE to be the energy difference between E_1 and KE_o i.e.

$$\Delta E = KE_o - E_1 \quad (6.5)$$

Then equation (6.4) can be written as:

$$\Delta E = [S]x \quad (6.6)$$

Where

$$[S] = \left[\frac{K}{cos\theta_1}\frac{dE}{dx}\Big|_{in} + \frac{1}{cos\theta_2}\frac{dE}{dx}\Big|_{out}\right] \quad (6.7)$$

$[S]$ is called the energy loss factor which contains the relationship between the energy and the depth information. This means a measured energy spectrum can therefore be directly converted into a depth scale.

The stopping cross section ε, is another important quantity in RBS defined as the energy loss per unit area density:

$$\varepsilon = -\frac{1}{N}\left(\frac{dE}{dx}\right) \quad (6.8)$$

N is the atomic density, in atoms/cm^3, stopping cross sections respectively with the common unit of eV·cm^2/(10^{15} atoms). The amount of energy loss per physical thickness is related to the stopping cross section [13].

If a target has two or more elements, the interaction process between the ion and component target are to a first order independent. The stopping cross section for a compound A_mB_n is written as:

$$\varepsilon^{A_mB_n} = m\varepsilon^A + n\varepsilon^B \quad (6.9)$$

where ε^A and ε^B are the stopping cross-sections of element A and B respectively and equation (6.9) is known as Bragg's rule [9][14].

6.2.1.4 RBS experimental setup

The RBS technique is based on the backscattering of the energetic particles in any given solid material [15]. In this study a Van de Graaff accelerator is used to generate these energetic particles. The Van de Graaff accelerator is a high-voltage electrostatic generator. It consists of a belt made of high dielectric material, two electrodes and metal pulleys with an ion source (figure 6-9). A diagram representing the Van de Graaff accelerator is shown in figure 6-9.

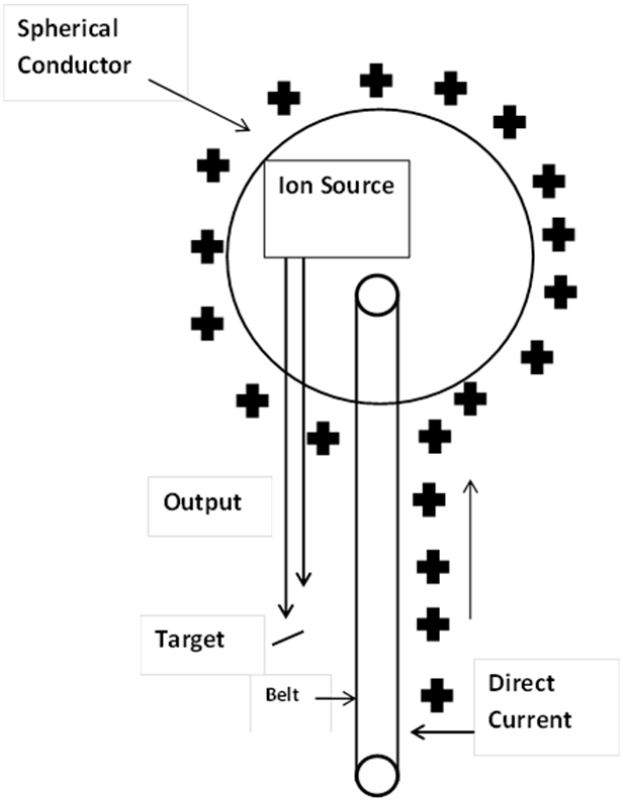

Figure 6-9: *Schematic diagram of a Van de Graaff accelerator.*

The charge source generates charge via the triboelectric effect as the belt rotates. The bottom needles are biased such that they attract electrons from the rotating belt and assist in making the belt move up with an excess of positive charge. This positive charge is removed by the comb of needles at the top and transferred to the large metal sphere known as the electrode. The charge build-up generated in the electrode results in a potential difference between the electrode and the ground.

The ion source of the accelerator machine at University of Pretoria is 2.7 MeV but for this investigation energy of 1.6 MeV was used. $^{4}He^{+}$ ions were used in this study and beam currents up to 15 nA can be obtained**.** A schematic diagram of the accelerator is shown in figure 6-11 below.

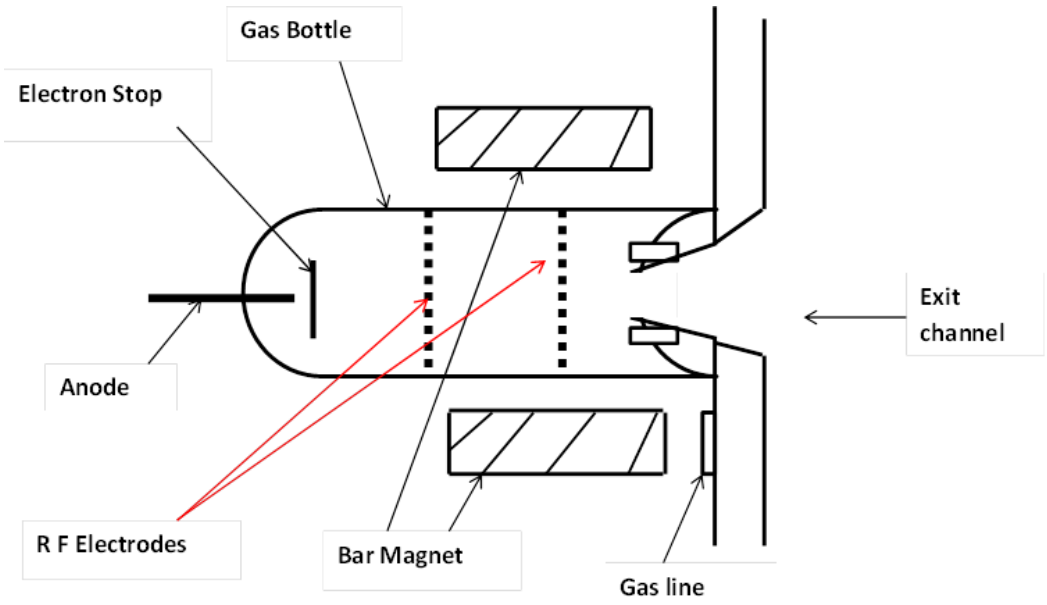

Figure 6-10: *Schematic diagram of the rf ion source.*

A He^+ mono-chromatic beam was used for analysis. This beam was produced by applying a dipole deflection magnet as mass and charge state separator. The beam was deflected into right beam line and guided into the sample chamber. This was done by combining of the horizontal and vertical slits allowing focusing and collimation of the beam. The sample chamber had a solid state detector, collimator (connected to the beam line), vacuum pump system (consisting of a fore pump and turbo pump) and a stage for holding the samples (which is connected to a three axis goniometer for controlled sample rotation). The energies of the backscattered alpha particles from the sample were detected by a solid state detector (Si-surface detector). Then signal from the detector is amplified and digitized by an analogue

inside the multi-chamber chamber analyzer (MCA). The output signal is then stored in a computer which is connected to the MCA. A spectrum of yield vs. channel is obtained

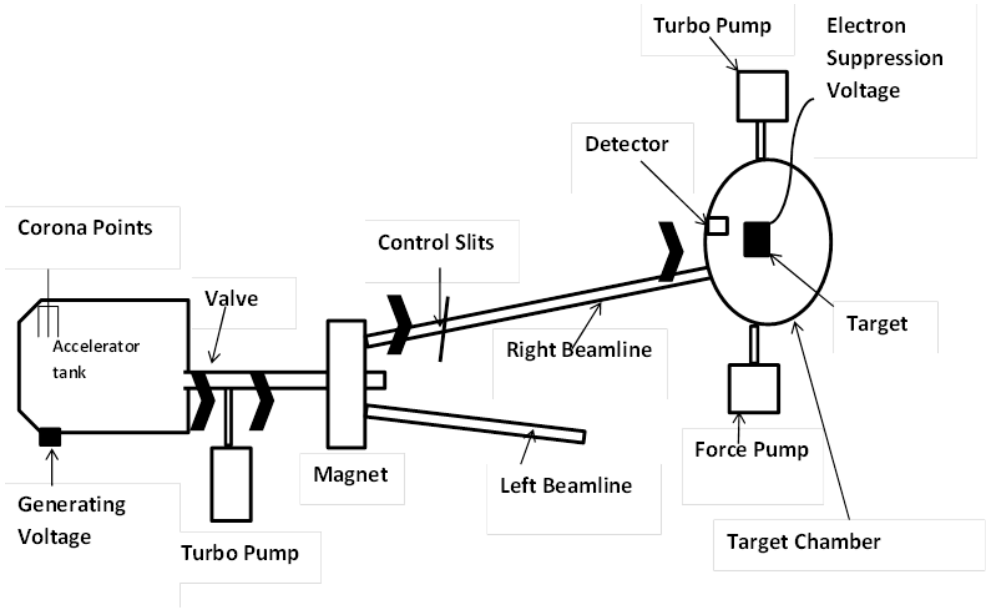

Figure 6-11: *Schematic diagram of the van de Graaff accelerator of the University of Pretoria.*

6.2.1.5 Data Acquisition

Figure 6-12 shows a block diagram for the RBS circuit. The surface barrier detector collects the backscattered particles at 165°. The voltage required (40 V) to establish the reverse bias of the detector is supplied by a Canberra high voltage supply. The surface detector is connected to a Canberra preamplifier. The signal from the surface detector is fed to the preamplifier, which generates a pulse for each incident ion. The height of the pulse is proportional to the energy of the detected particle. This signal is further amplified and shaped by a Tennelec TC 243 amplifier, then sent to the digital oscilloscope to monitor the shape of the pulse (unipolar signal). The signal is digitized and displayed by a multichannel amplifier

(MCA). The pulse height analyser (PHA) mode in the MCA is used during the RBS data collection. Each of the pulses received and recorded is viewed as counts on the RBS spectrum.

While these processes are happening, current from the target sample is sent into an Ortec 439 current integrator where it is digitized. A logical signal from the current integrator is sent to the charge counter and from the counter it is delivered to the MCA and counter. The logic signal from this current commands the counter when to start and stop counting. It also directs the MCA when to start and stop processing the unipolar signal from the amplifier. The desired energy range is selected by the single charge analyzer (SCA) which can be processed by adjusting the lower and upper energy discriminators in the MCA. The output of the MCA is fed to the computer, where it is recorded as yield versus channel number spectrum.

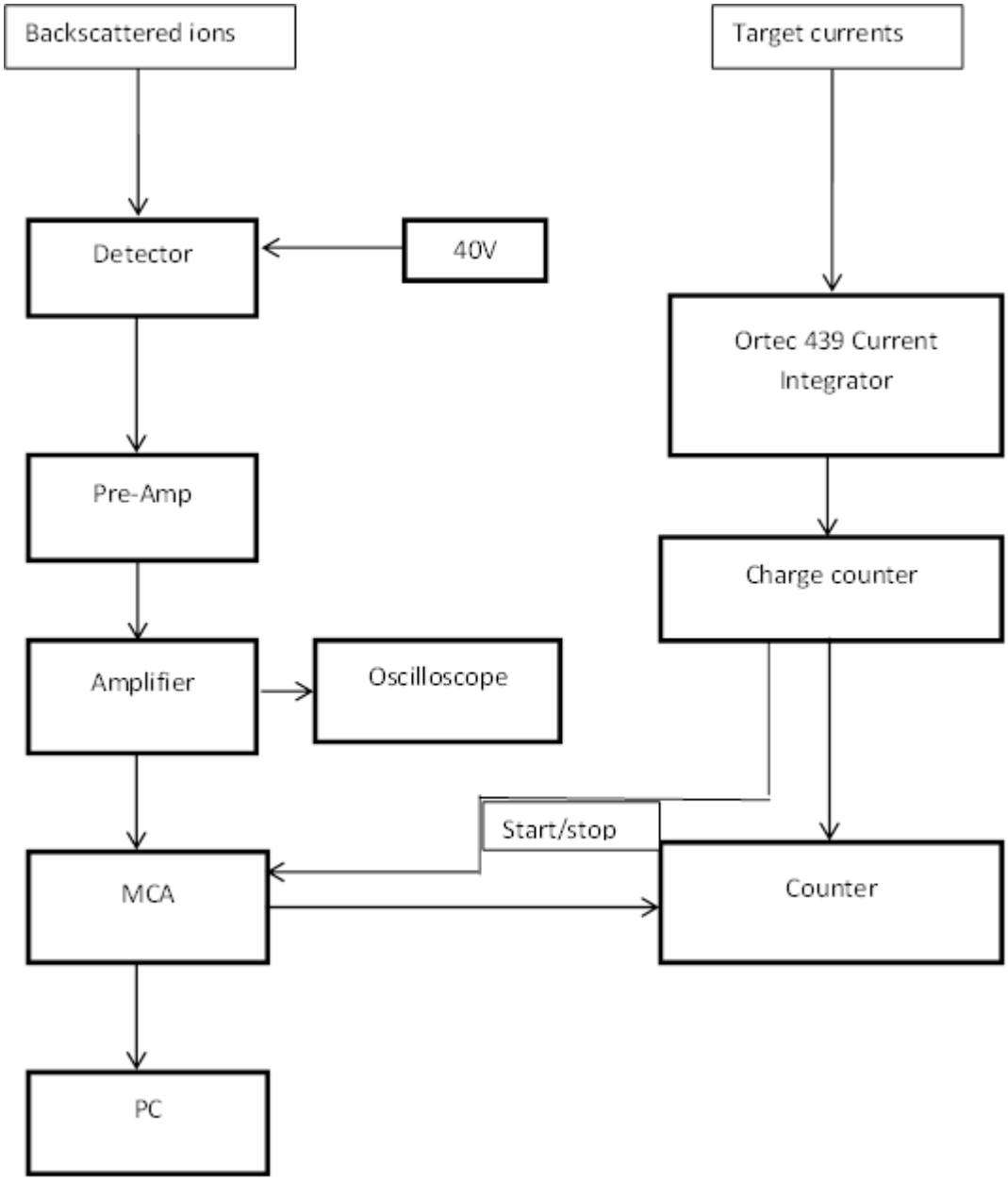

Figure 6-12: *Block diagram for the RBS electronic circuit at the University of Pretoria.*

6.2.1.6. Backscattering Spectrum Simulation Using RUMP

RUMP (Rutherford Universal Manipulation Program) computer program was used to simulate the RBS spectra. RUMP was originally created by L. R. Doolittle [16] and further developed at Cornell University. The RBS data simulated in RUMP is given in the form of

layer-by-layer composition of W-SiC interface before and after annealing. A description of the sample such as elemental composition and thickness of the layers is specified. The measurement parameters used during RBS analysis must be inserted on the RUMP simulation program before beginning the simulation. The condition used to analyse the samples on RBS must be similar with the conditions used for simulation. These include the projectile type, the incident energy of the bombarding ions and the type of the bombarding ion, its charge, current, energy calibration, scattering geometry parameters and the detector parameters. Once the parameters have been inserted in the RUMP code, simulation of the theoretical spectra for the thin film targets can be presumed. The information generated from the simulation includes the depth profile of the sample, sample composition, thickness, diffusion and reaction information, etc. Detailed information about the program is available in [17].

RBS data was calibrated using the standard elements such as Si, Cr, W and O. The surface channels for these elements were obtained from the RBS raw data. The surface energies were calculated using the kinematic factor of each element and the incident beam energy. A graph with a linear fit of energy of the scattered particle vs the channel number was plotted. The linear fit can be represented by the equation:

$$E = kx + c \tag{6.10}$$

The energy calibration curve obtained is shown in figure 6-13. Energy calibration is important because the energy to channel function determines the location of the peak edge of the simulation. The energy calibration was repeated for each set of samples measured on different days.

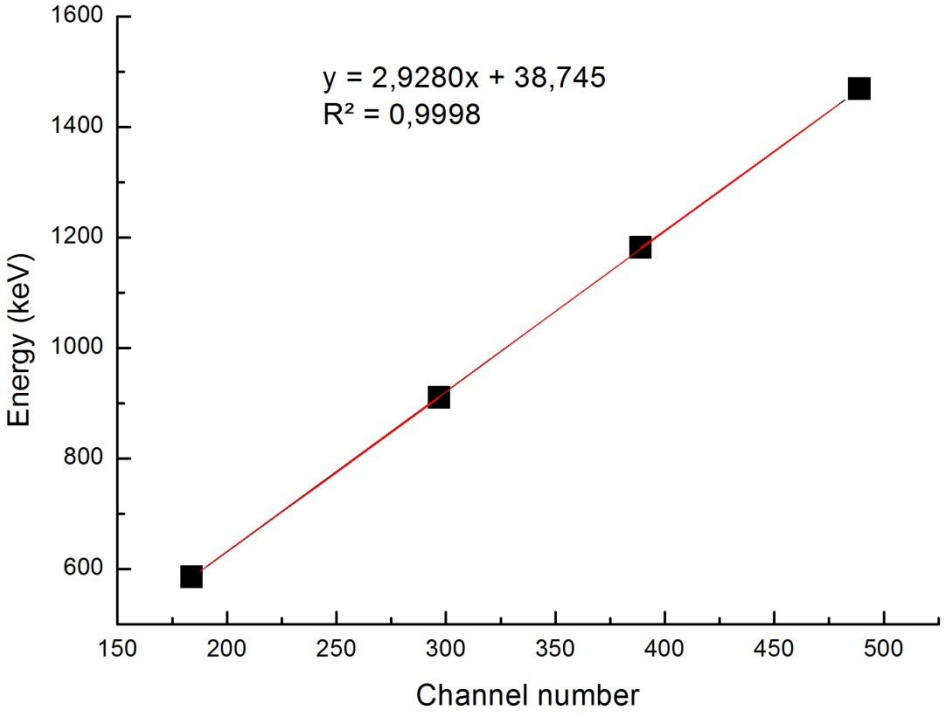

Figure 6-13: *The energy calibration curve.*

RUMP simulations were used to calculate the percentages of the phases formed after tungsten reacted with SiC. The phases were calculated based on the phases identified on the XRD results. Because RBS results can only give us elemental composition ratios and the thickness of the reaction zone, XRD was used to identify the phases. The phases were calculated by considering the W, Si and C concentrations in the reaction zone from the simulated spectra and comparing it to the XRD results. For example if we have the following concentrations 0.12, 0.20 and 0.68 for Si, C and W respectively and we have the following phases WC, WSi_2, and WO_2. Then a concentration of 0.20 of W will be consumed to form WC phase. For the WSi_2, about 0.06 of W will be consumed leaving about 0.74 concentration of unconsumed SiC.

6.2.2. Scanning Electron Microscopy (SEM).

The scanning electron microscopy (SEM) is a microscope that uses electrons instead of light to form high-resolution images of sample surfaces. Since its first development in the 1930's, SEM has been used in different studies such as material development, metallic materials, ceramics, semiconductor, medical science and biology [18]. SEM is used in order to gather information about the sample's surface and near surface morphology, chemical composition, crystal structure and orientation of material [19]. Figure 6-14 illustrates the processes taking place during SEM measurements.

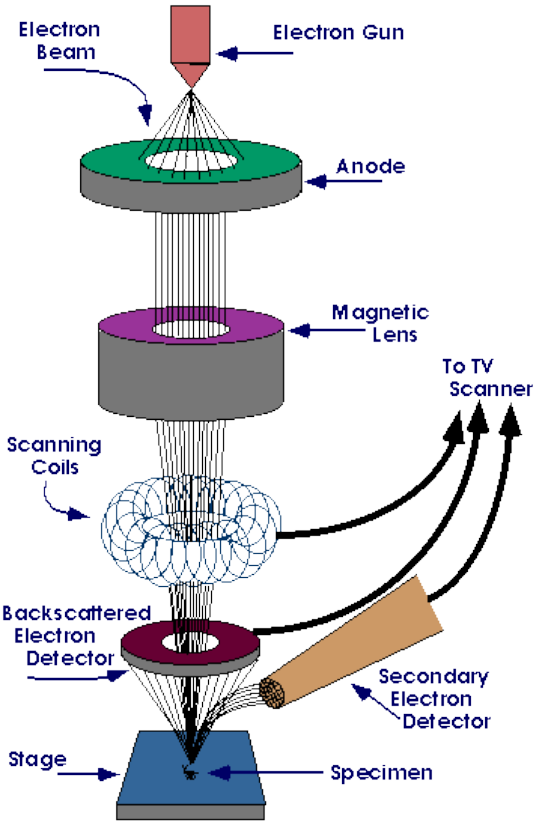

Figure 6-14: *A schematic diagram representing the processes taking place during SEM operation, taken from [20].*

At the top of the microscope lies an electron gun which generates a stable beam of electrons. There are three types of electron guns, viz. tantalum hexaboride (LaB_6), tungsten hairpin and

field emission [21][22]. In this case, a field emission gun (FEG) was used. The FEG cathode usually has a sharp metal (tungsten) tip of 100 nm or less. The electrons generated by the electron gun are primarily accelerated toward an anode that is adjustable from 200 V to 300 kV [3]. There are two types of FEG, which is the cold and Schottky field emission gun. For both field emissions, ultra-high vacuum conditions are required to avoid contamination of the cathode surface. Before the machine is operated, the tip is flushed cleaned by heating at about 2500K for a few seconds. The accelerated electrons (beam) pass through the electromagnetic fields and lenses, which focus the beam down towards the sample. A pair of deflector coils controlled by the scan generator are responsible for rastering the focused beam across the sample surface [22].

The incident electrons cause electrons to be released from the sample due to inelastic and elastic scattering within (near-surface) the material. Various particles carrying information from the sample will be released (as illustrated in figure 6-15) and fed to the detectors. The particles produced from the interaction of the electrons with the samples are: secondary electrons, backscattered electrons, characteristic X-rays and Auger electrons.

Secondary electrons (SE) are the electrons which results due to the inelastic collision of the electron beam with the electrons of the sample. These electrons have energy which is less than 50 eV [23]. The SE are used for topographical imaging as they are generated from regions very close to the surface (< 10 nm). These electrons are generated along the incident electrons' trajectory but only those generated a few nanometres underneath the sample surface are detected – the others are absorbed in the sample owing to their low energy [18]. The electrons intensity variation creates a contrasting image. The contrast of the sample surface in this case depends on the where about of SE released. More electrons are able to escape at an edge than away from the edge and this result in the edge appearing brighter.

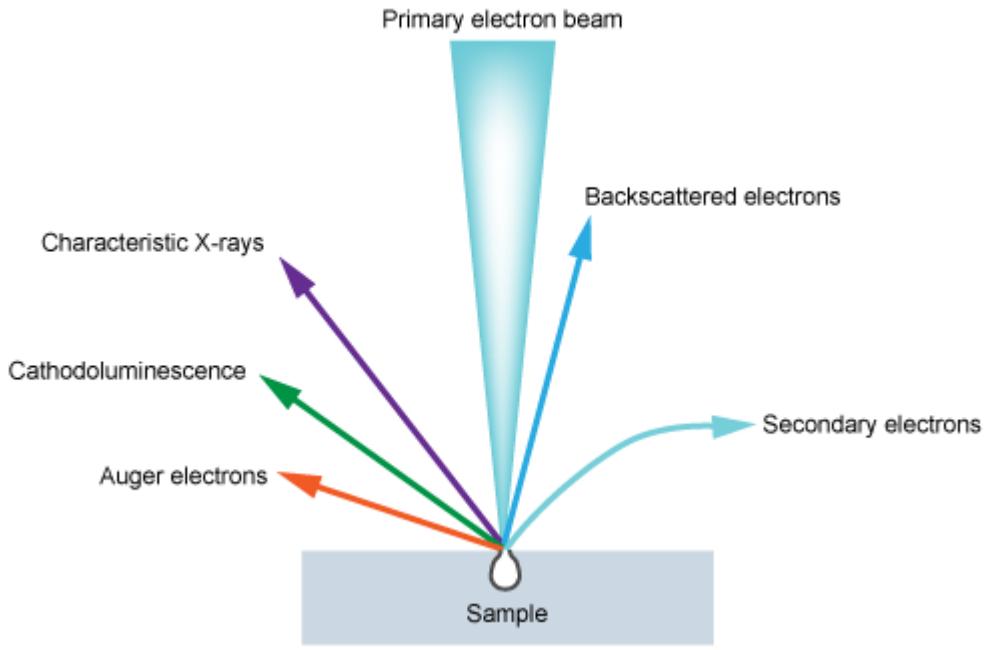

Figure 6-15: *Schematic representation of the interaction between the electron beam and sample together with the particles formed, taken from [24].*

The tilt effect and edge effect are among the contrast factors for SE, both due to the sample surface morphology. They are caused by the effects of topography on the generation of secondary electrons and are what gives form and outline to the images produced by the Secondary Electron detector. Electrons preferentially flow to and are emitted from edges, protrusion and circumferences of the sample. Poor signal intensity occurs in those regions shielded from the detector. The Back scattered electrons (BE) emitted from regions of the sample facing towards the detector enhance the topographic contrast [25][26]. Lowering the beam kV can reduce edge effect. The protrusions and circumferences of objects on sample surface as shown in figure 6-16 generates a large number of SE , thus such places will appear brighter than even portions.

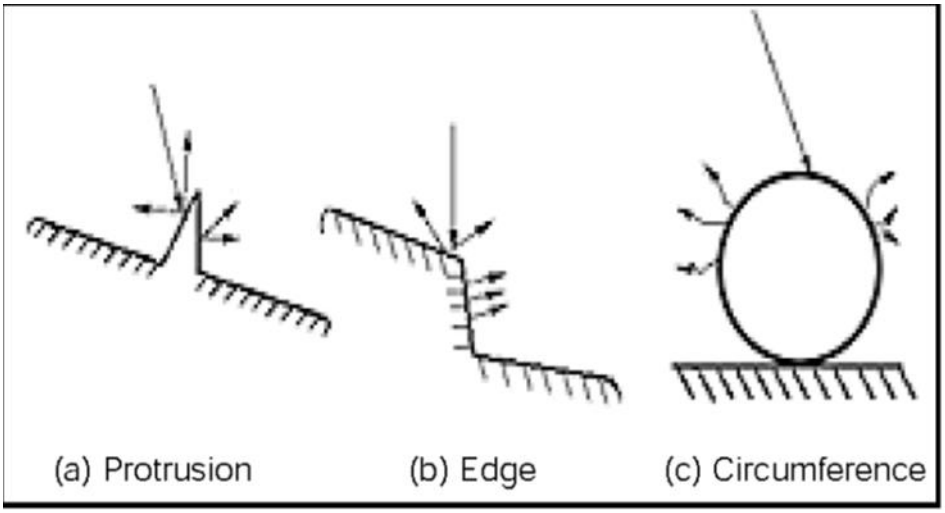

Figure 6-16: *A schematic representation of the edge effect of SE with different surface conditions, taken from* [25].

Backscattered electrons (BE) are the electrons which result due to the elastic collision between the electron beam and the nucleus of the sample. These electrons have more energy as compared to SE and provide information from deeper regions of the sample. BE provides information about composition and topography of the sample. BE give different contrast between areas with different chemical compositions [18]. That is an element with a high atomic number will appear brighter than the one with a low atomic number. Samples which are insulators absorb the incident electrons, which lead to charge up of the sample surface. This makes the SEM image look brighter giving false information about the sample. Insulating samples have to be coated with a conductive film to reduce charge up.

Auger electrons are a result of the outer higher energy electrons occupying the lower energy level due to excitation of the primary electrons. The signal from the Auger electrons gives information about compositional maps of the surface. The characteristic X-rays provide information about the chemical characterization of the sample. X-rays are formed when

electrons in the outer shell with high energy fills the hole in the lower energy shell. The energy is released is in the form of X-ray.

The Zeiss Ultra 55 field emission SEM from University of Pretoria was used to study the surface morphology of the samples in this study. The microscope is equipped with secondary electrons, backscattered electrons and in-lens SE detectors. In this study the in-lense was mostly used for analysis. The in-lens detector is located in the column above a sample and it is capable of detecting scattered electrons of the surface originating from the impact of the beam. In-lens detection is often combined with energy filtering of the secondary electrons that form the image. The analysis of the surface for the W/SiC thin film was done with beam energy of 2 kV, operating with 0.7 nm spatial resolution to show the surface features.

6.2.3 X-ray Diffraction (XRD).

X-ray diffraction (XRD) is a popular technique used in different fields for material analysis. It is mostly used for phase identification, to measure the size of the crystalline material, internal stress and strain of crystalline regions [27]. The information obtained from this technique is the phases a film is composed of, thickness, roughness, and texture. XRD is a qualitative and quantitative technique which is reliable and does not necessarily require any sample preparation [28].

X-rays are electromagnetic waves with a short wavelength of (about 0.1 to 10 nm) and they are shorter than the wavelength of visible light (about 400 to 800 nm) [29]. They have high energy (of about 10^2 to 10^5 eV) as compared to light (10 eV) [29].

When a monochromatic X-ray beam incident on a crystal lattice, it gets scattered at all the scattering centers, which lie on the lattice planes of the sample (see figure 6-17). The angle between the incident X-ray beam and the lattice planes is called θ. The angle between the incident and scattered X- ray beams is called 2θ. The 2θ of maximum intensity is known as the Bragg angle. The scattered beams at different lattice planes must be scattered coherently, to give maxima in scattered intensity. These conditions give rise to in the Bragg equation (5-11):

$$n\lambda = 2d \sin \theta \qquad (5\text{-}11)$$

where *n* is an integer, λ is the wavelength of the X-ray, *d* is the interatomic spacing between the planes in lattice of the sample generating the diffraction and θ is the diffraction angle in degrees. It can be seen from the Bragg equation that if the wavelength is known then the distance between lattice planes of the sample can be determined.

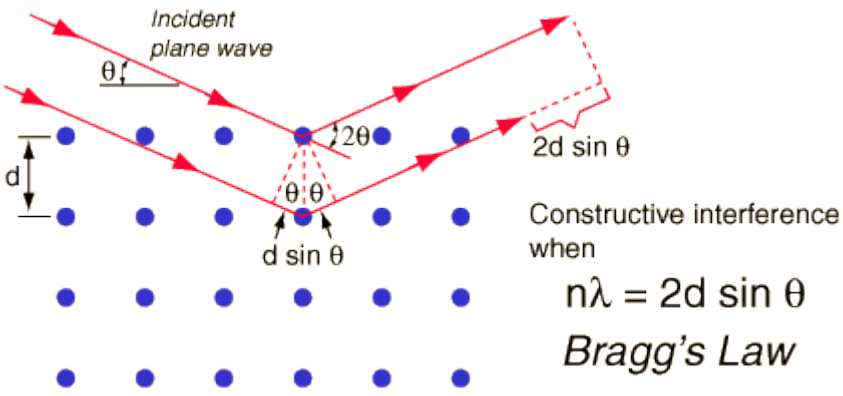

Figure 6-17: *Shows Bragg's law for an incident beam x-ray beam on a crystal lattice plane, taken from [30].*

X-ray diffractometers comprise of the following basic elements: an X-ray tube, a sample holder, and an X-ray detector. X-rays are generated in a cathode ray tube by heating the filament to produce electrons. The electrons are then accelerated by high voltage towards the target, bombarding the target material with electrons. If the electrons have sufficient energy to dislodge inner shell electrons of the target material, characteristic X-ray are produced. These X-rays are collimated and directed onto the sample which needs to be analyzed. The geometry of an X-ray diffractometer is such that the sample rotates in the path of the collimated X-ray beam at an angle θ. While the X-ray detector is mounted on an arm to collect the diffracted X-rays and rotates at an angle of 2θ. The instrument used to maintain the angle and rotate the sample is termed a goniometer. The sample and detector are on the same side. As the sample and/or detector being rotated, the intensity of the reflected X-rays is recorded. When the geometry of the incident X-rays impinging the sample satisfies the Bragg equation, constructive interference occurs and a peak (in a form of intensity) occurs. A detector records and processes this X-ray signal and converts the signal to a count rate which is then output to a device such as a printer or computer monitor.

The spectra contains numerous components, the most common being K_α and K_β. The K_α consists of $K_{\alpha 1}$ and $K_{\alpha 2}$. $K_{\alpha 1}$ has a slightly shorter wavelength and twice the intensity as $K_{\alpha 2}$. The specific wavelengths are characteristic of the target material (Cu, Fe, Mo, Cr). $K_{\alpha 1}$ and $K_{\alpha 2}$ are sufficiently close in wavelength such that a weighted average of the two is used. Copper is the most common target material for single-crystal diffraction, with Cu $K\alpha$ radiation = 1.5418 Å [31]. Other target material are Cr ($K\alpha$ 2.29 Å), Fe ($K\alpha$ 1.94 Å), Co ($K\alpha$ 1.79 Å) and Mo ($K\alpha$ 0.71 Å) [31].

6.2.3.1 Scherrer Equation

The Scherrer equation relates the size of crystallites, in a solid to the broadening of a peak in a XRD diffraction pattern. The equation is used to determine the particle size of crystals. The Scherrer equation can be written as [32]:

$$D = \frac{K\,\lambda}{B\cos\theta} \qquad (5\text{-}12)$$

where D mean size of the crystal , K is a dimensionless shape factor (values between 0.62 – 2.08), λ is the wavelength of the X-ray, B is the line broadening at the full width half maximum (FWHM) and θ is the Bragg angle. The Scherrer equation is limited to nano size particles and it cannot be used for grains larger than about 0.1 to 0.2 μm. The Scherrer formula provides a lower bound on the particle sizes because of a variety of factors. These factors can contribute to the width of a diffraction peak besides instrumental effects and crystallite size; the most important of these are usually inhomogeneous strain and crystal lattice imperfections.

6.2.3.2 XRD experimental setup

The crystalline phases obtained from XRD are identified using the database provided by the International Centre for Diffraction Data (ICDD). The peak positions and relative intensities are compared with those found in the ICDD database to identify the phases present. The ICDD keeps the database of inorganic and organic species identified as Powder Diffraction File (PDF). The PDF-2 database version comprises in addition to the d-spacing and

intensities, the *hkl* values, the chemical formula, cell dimensions, selected physical properties and references [27].

The XRD analysis was performed at South African Nuclear Energy Corporation (NECSA). The Bruker D8 Discover equipment was used to analyse the samples. The equipment uses Cu (K_α) X-ray radiation source. The collection was done at a two-theta step size of 0.03º and dwelling time 240 s per frame (four frames). The incident X-ray beam was retained at 0.5º relative to the surface of the sample and the diffraction pattern collected by the detector rotated by the goniometer from 22º to 120º two-theta.

6.2.4 Atomic Force Microscopy (AFM).

The AFM instrument was invented by Binning and co-workers in 1986, because they wanted an instrument which does not have the limitations of scanning tunnel microscopy (STM) [33][34]. It falls under the family of Scanning Probe Microscopy (SPM) techniques which includes Scanning Tunnelling Microscopy (STM), Scanning Force Microscopy (SFM), Scanning Near Field Optical Microscopy (SNOM), etc. [35]. Atomic force microscope (AFM) is an instrument which uses a sharp probe to measure the surface topography in both two and three dimension imaging and also the physical properties of the surface. AFM produces high resolution imaging for different material surfaces in a nanometer scale [33].

The sharp probe is placed in such a way that it is close enough to the surface so that it can interact with the force fields associated with the surface. The probe is then scanned over the sample surface in a way that the forces between the sample and the probe remain constant. In tapping mode the cantilever oscillates near the sample surface. The probe is usually made of

silicon or silicon nitrite (Si_3N_4). An image containing the surface information such as roughness, electrical properties, etc. will be created. This image is created by monitoring the precise motion of the probe as it is scanned across the surface. The information received from the image about the surface morphology include: quantitative roughness value, grain size and structure.

In the microscope the forces between the cantilever and the sample surface is measured by the photo detector (force sensor). The output from the detector is sent to the Z axis feedback controller that drives the Z motion generator (Piezoelectric tube scanner). The feedback controller uses the detector output to maintain a fixed distance between the probe and the sample. The probe is moved across the X and Y axis by the X-Y motion generators (Piezoelectric tube scanner). The motion of the probe is monitored and used to generate an image of the surface. The probe moves in a raster-like pattern. AFM have very good vertical resolution in the order of 0.1 nm [19].

The laser from the laser source is focused on the backside of the cantilever and reflected into a detector with two sections (see figure 6-18). The output from each sides of the detector is converted in a deferential amplifier to the electrical charge. The cantilever bends when the probe interacts with the surface, and the directions of the light changes causing a change in the amount of light in the two detector sections. The cantilever measures the repulsive or attraction force between the atoms on the tip and the sample surface during the deflection of the probe.

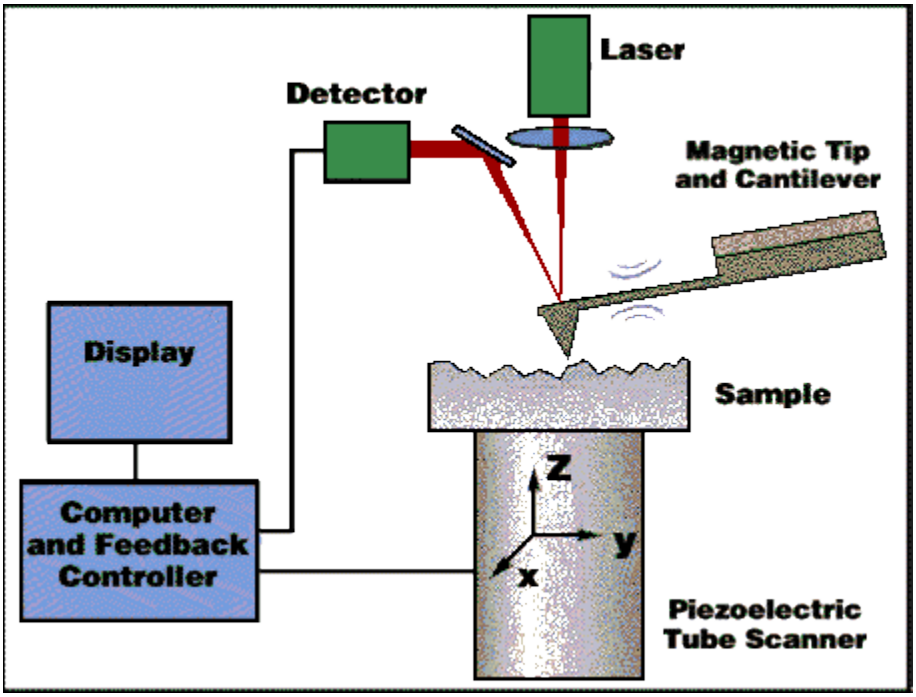

Figure 6-18: *Schematic diagram of an AFM setup, taken from [36].*

AFM has two operating modes, that is, the tapping mode and contact mode, see figure 6-19. In contact mode, the constant force between the tip and sample is maintained by the feedback control, when the probe is scanning across the sample surface. The image is constructed by the amount of cantilever deflection (repulsive forces) required to keep the force constant.

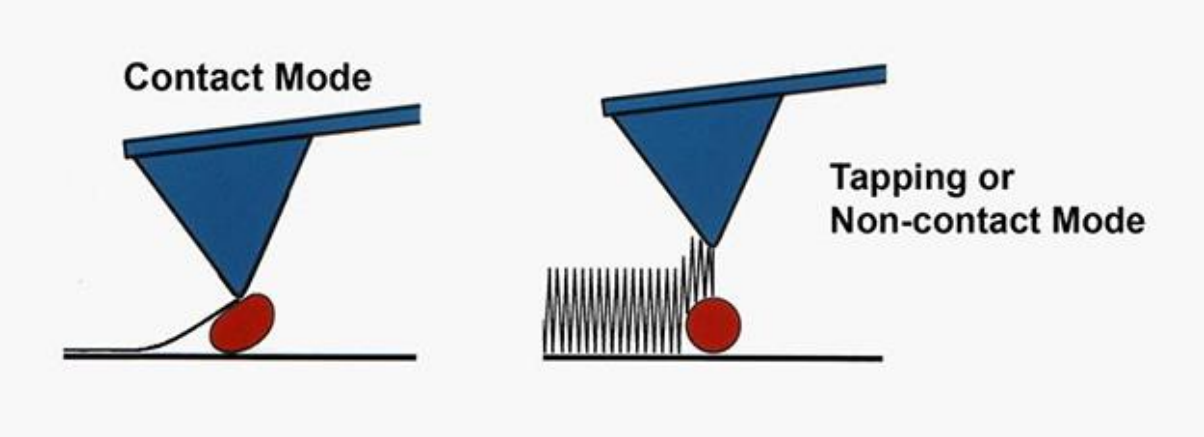

Figure 6-19: *Schematic diagram representing contact and tapping mode, taken from [37].*

In tapping mode, the sharp tip touches the sample surface for a very short contact time, thus avoids the issue of lateral forces and drag across the surface. The cantilever vibrates at its resonance frequency and as it moves closer to the surface, oscillations are affected by the tip-surface interaction. The voltage required to adjust the z-axis of the piezoelectric scanner in order to maintain the pre-set amplitude of oscillation is used to create the images and the surface height.

The 2D and 3D AFM images provide both quantitative and qualitative information of the sample surface. The topography of thin film usually takes the series of peaks and valleys which may vary in both height and spacing. Surface roughness measurements are done in two planes: one in the plane of the surface described by spatial parameters, and the second is perpendicular to the surface of the thin film described as height deviation in the z-direction. In quantitative analysis of AFM images the following parameters are used to describe the surface changes:

- Average roughness (R_a)
- Root mean square roughness (R_{rms})
- Mean grain size
- Peak-to valley roughness (R_{pv})

In characterizing the surface topography, the amplitude parameters are the main parameters used. The most commonly used amplitude parameters are R_a and R_{rms}. Particularly, R_{rms} is used to study the changes in the newly formed surface as well as spatial differences when studying the surface feature using different scales. The R_{rms} is used mostly because it is more sensitive to large deviations with respect to the mean line. If one wants to know if R_{rms} values

are making sense, the height points have to be uniformly distributed according to a normal distribution curve [38].

The R_a is described as follows:

$$R_a = \frac{1}{N}\sum_{i-1}^{N}\left|z_i - z_{cp}\right| \tag{6.13}$$

Where z_i is the current z value, z_{cp} is the average of the z values within the given area and N is the number of points within the scan area. Thus, the R_a is the arithmetic mean of the absolute values of the height of the surface profile $\left|z_i - z_{cp}\right|$.

The R_{rms} takes the square of the measures of R_a. The R_{rms} roughness of a surface is similar to the roughness average, the difference being the mean squared absolute values of surface roughness profile. The function R_{rms} is defined as follows:

$$R_{rms} = \sqrt{\frac{\sum_{i-1}^{N}(z_i - \bar{z})^2}{N}} \tag{6.14}$$

where $\bar{z}$ is the average of the z values within the given area, z_i is the z value for a given point and N is the number of points within the given area.

The maximum profile peak height (R_p) is the measure of the highest peak on the surface profile from the baseline. The maximum profile valley depth (R_v) is the measure of the deepest valley across the surface profile analyzed from the baseline.

6.2.4.1 AFM experimental setup

The atomic force microscopy from University of Pretoria was used to study the surface morphology of the samples. W-SiC diffusion couples were mounted on a metal using carbon tape. The AFM images where obtained using the Dimension Icon AFM system, working in contact mode. A Si_3N_4 cantilever and Si probe of a tip radius ≥ 10 nm were used in this study with a spring constant of 0.32 N/m, a resonance frequency of the Si probe was 40-47 kHz and a scan rate of 0.5 Hz. The AFM images obtained were analyzed using NanoScope Analysis (Bruker, USA) software.

In this study the AFM images were collected in two different scan sizes of 3 μm × 3 μm and 20 μm × 20 μm at three different spots on the sample for as-deposited and annealed samples (700 ºC, 800 ºC, 900 ºC and 1000 ºC for 1h). The AFM images had 256 × 256 data points or pixels and the 3D images were taken in a raster scan pattern extending to the scan length, L. The scan of 20 μm × 20 μm was used for analysis of the samples.

6.3 References

[1] K. Seshan, *Handbook of thin film deposition process and Technologist*, Second edi. Santa Clara, California: Noyes Publication, 2002.

[2] M Systems, "Monitoring & Control of Thin Film Deposition Process Sputter Deposition Equipment," *M Systems Newsletter*, 2015. [Online]. Available: http://www.m-system.co.jp/newsletter/182/clip_contents.html. [Accessed: 27-Apr-2017].

[3] E. G. Njoroge, "Solide-state interaction between Zr thin films and SiC," PhD thesis, University of Pretoria, 2014.

[4] T. Donnellan, "Materials & Manufacturing - AC Sputtering." [Online]. Available: https://www.arl.psu.edu/mm_mp_ac_sputtering.php. [Accessed: 11-Feb-2016].

[5] B. Gadicharla, "Processing and characterization of metallic thin films : sputter deposition, substrate temperature calibration, thickness determination and thermal analysis," PhD thesis, Lehigh University, 1998.

[6] T. T. Thabethe, T. T. Hlatshwayo, E. G. Njoroge, T. G. Nyawo, T. P. Ntsoane, and J. B. Malherbe, "Interfacial reactions and surface analysis of W thin film on 6H-SiC," *Nucl. Instruments Methods Phys. Res. Sect. B Beam Interact. with Mater. Atoms*, vol. 371, no. B, pp. 235–239, 2016.

[7] W. K. Chu and Wei-Kan Chu, *Backscattering Spectrometry*. New York: Academic Press Inc, 1978.

[8] J. W. Meyer and E. Rimini, *Ion Beam Handbook for Material Analysis*. London: Academic Press Inc, 1977.

[9] J. R. Tesmer and N. M, *Handbook of Modern Ion Beam Materials analysis*. Pittsburgh: Materials Research Society, 1995.

[10] J. Grob and P. Siffert, "Rutherford Backscattering Spectrometry (RBS)," *Prog. Cryst. growth Charact.*, vol. 8, no. 1–2, pp. 59–106, 1984.

[11] L. Feldman and J. Meyer, *Fundermentals of Surface and Thin Film Analysis*. New York: Elsevier Science Publishing Co., 1986.

[12] T. T. Thabethe, "RBS INVESTIGATION OF THE DIFFUSION OF," MSc dissertation, University of Pretoria, 2013.

[13] E. Kamaratos, "The Mean Excitation Energy for Stopping Power I, the Bragg Rule, and Chemical and Phase Effects. Application of a Statistical Treatment to the Determination of I for Chemically Bound Particles," *Chem. Rev.*, vol. 84, pp. 561–576, 1984.

[14] W. H. Bragg and R. Kleeman, "On the α particles of radium, and their loss of range in passing through various atoms and molecules.," *London, Edinburgh, Dublin Philos. Mag. J. Sci.*, vol. 10, p. 318, 1905.

[15] R. van de Graaff, "A 1,500,000 volts electrostatic generator," *Phys. Rev. A*, vol. 39, p. 1919, 1932.

[16] L. R. Doolittle, "Algorithms for the rapid simulation of Rutherford backscattering spectra," *Nucl. Instruments Methods Phys. Res. Sect. B Beam Interact. with Mater. Atoms*, vol. 9, no. 3, pp. 344–351, 1985.

[17] “Genplot Information.” [Online]. Available: http://www.genplot.com/RUMP/index.htm. [Accessed: 27-Apr-2017].

[18] T. T. Hlatshwayo, “Diffusion of silver in 6H-SiC,” PhD thesis, University of Pretoria, 2010.

[19] S. Zhang, L. Li, and A. Kumar, *Material characterisation techniques*, 1st ed. Florida: Taylor & Francis, 2009.

[20] “SEM Image.” [Online]. Available: https://www.purdue.edu/ehps/rem/rs/sem.htm. [Accessed: 18-Jan-2016].

[21] W. Zhou and Z. Wang, *Scanning Microscopy for Nanotechnology-Techniques and Application*. Springer-Verlag, 2006.

[22] B. Hafner and B. Hafner, “Scanning Electron Microscopy Primer,” *Cities*, pp. 1–29, 2007.

[23] E. Velasco and E. S. Velasco, “Scanning Electron Microscope (SEM) as a means to determine dispersibility,” PhD thesis, Iowa State University, 2013.

[24] “Electron-matter interactions | MyScope.” [Online]. Available: http://www.ammrf.org.au/myscope/sem/background/concepts/interactions.php. [Accessed: 27-Apr-2017].

[25] A. Technology, “A Guide to Scanning Microscope Observation A Guide to Scanning Microscope Observation.” [Online]. Available: http://www.jeolusa.com/RESOURCES/Electron-Optics/Documents-Downloads?EntryId=1. [Accessed: 12-Jan-2017].

[26] S. Reed, *Electron Micropobe Analysis and Scanning Electron Microscopy in Geology*, Second edi. United Kindom: Cambridge University Press, 2005.

[27] J. I. Langford and D. Louer, "Powder diffraction," *Reports Prog. Phys.*, vol. 59, no. 2, pp. 131–234, 1996.

[28] P. F. Fewster, "X-ray analysis of thin films and multilayers," *Reports Prog. Phys.*, vol. 59, no. 11, pp. 1339–1407, 1999.

[29] P. Knipping and M. Von Laue, "X-Ray diffraction," 1952. [Online]. Available: http://dasher.wustl.edu/bio5325/reading/vanholde-xray-98.pdf. [Accessed: 11-Feb-2016].

[30] "Bragg's Law." [Online]. Available: http://hyperphysics.phy-astr.gsu.edu/hbase/quantum/bragg.html. [Accessed: 30-May-2017].

[31] G. Hölzer, M. Fritzsch, M. Deutsch, I. Härtwig, and E. Förster, "Ka1,2 and Kb1,3 X-ray emission lines of 3d transition metals.," *Phys. Rev. A*, vol. 56, pp. 4554–4568, 1997.

[32] Y. Zhao and J. Zhang, "Microstrain and grain-size analysis from diffraction peak width and graphical derivation of high-pressure thermomechanics," *J. Appl. Crystallogr.*, vol. 41, no. 6, pp. 1095–1108, 2008.

[33] E. Meyer, "Atomic force microscopy," *Prog. Surf. Sci.*, vol. 41, no. 3–49, p. 51, 1992.

[34] G. Binnig, C. F. Quate, and C. Gerber, "Atomic Force Microscopy," *Phys. Rev. Lett.*, vol. 56, p. 930, 1986.

[35] W. Bowen and N. Hilal, *Atomic Force Microscopy in Process Engineering*,

Introduction to AFM for Improved Process and Products. Oxford, UK: Butterworth-Heinemann, Elsevier, 2009.

[36] U. Greifswald, "AFM Setup," 2016. [Online]. Available: http://www.engr.sjsu.edu/WofMatE/images/mfmschem.gif. [Accessed: 27-Apr-2017].

[37] H. G. Hansma, "Research on Biological Atomic Force Microscopy." [Online]. Available: http://web.physics.ucsb.edu/~hhansma/biomolecules.htm. [Accessed: 27-Apr-2017].

[38] M. Raposo, Q. Ferreira, and P. a Ribeiro, "A Guide for Atomic Force Microscopy Analysis of Soft- Condensed Matter," *Mod. Res. Educ. Top. Microsc.*, pp. 758–769, 2007.

Chapter 7 : Results and Discussion

In this study, the interaction between tungsten (W) and SiC together with the surface morphology of W thin film deposited on SiC were investigated. The as-deposited samples were annealed in vacuum, hydrogen and argon environments. The as-deposited and annealed samples were analyzed using RBS, XRD, SEM and AFM. In this chapter, the findings upon annealing in the different atmospheres are discussed. Firstly, the vacuum annealing results are discussed, followed by the hydrogen annealing results and finally the argon annealing results.

7.1 As-deposited samples

7.1.1 Rutherford Backscattering Spectrometry

A typical RBS spectrum of W deposited on 6H-SiC (black) is shown in figure 7-1. The corresponding simulated spectrum (red) obtained using RUMP [1] computer code is also included. The horizontal axis represents the energy of the backscattered particles in MeV and in channel number. The vertical axis is the normalized yield, that is, the amount of particles which are scattered into the detector normalized to the total incident beam dosage, the detector solid angle and the channel width of a multichannel analyser. The arrows in figure 7-1 indicate the surface energy or channel positions of the elements. W is located at the high-energy region of the spectra at channel number 488 because it has the highest kinematic factor. Silicon, oxygen and carbon are located at 297, 186 and 126, respectively. The location of Si and C below their surface energy positions (at some depth below the surface of the sample) is due to the deposited W layer. The Si high energy edge and W lower energy edge separation is distinct, this is because W has higher mass compared to Si and C since RBS is

sensitive to mass. Carbon is superimposed on top of the Si signal at around channel number 117. There was no diffusion between W thin film and SiC substrate observed on the as-deposited.

The thickness of the as-deposited layer obtained from RUMP simulation was about 73.8 nm and was composed of about 63.4 at.% W and 36.6 at.% O. Thus, the RBS results indicated the presence of oxygen on the W as-deposited layer. This reaction was not caused by the W-SiC exposed to the atmospheric gases outside the deposition chamber, because W does not react with oxygen at room temperature [2][3]. The oxygen contamination came from the deposition chamber during the deposition process. The oxygen was incorporated into the depositing W layer and reacted with the W atoms to form tungsten oxide (which was identified using XRD - see subsection 7.2.2). The presence of tungsten oxide was confirmed by XRD analysis. This seems also to be consistent with RBS oxygen profile in Fig. 7-1. The

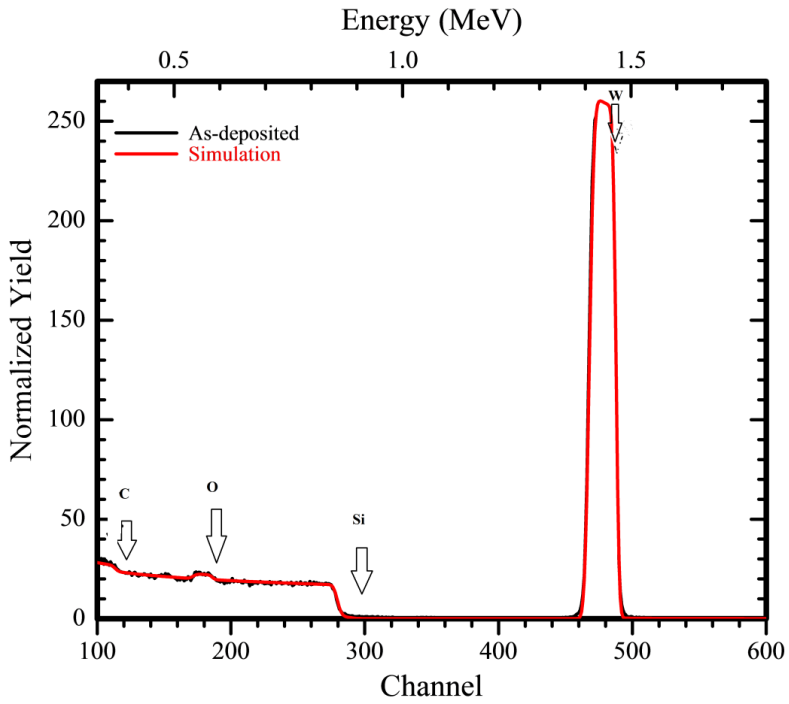

Figure 7-1: *Overlay of the as-deposited RBS spectrum of W deposited on 6H-SiC and the simulated spectrum obtained using the RUMP code.*

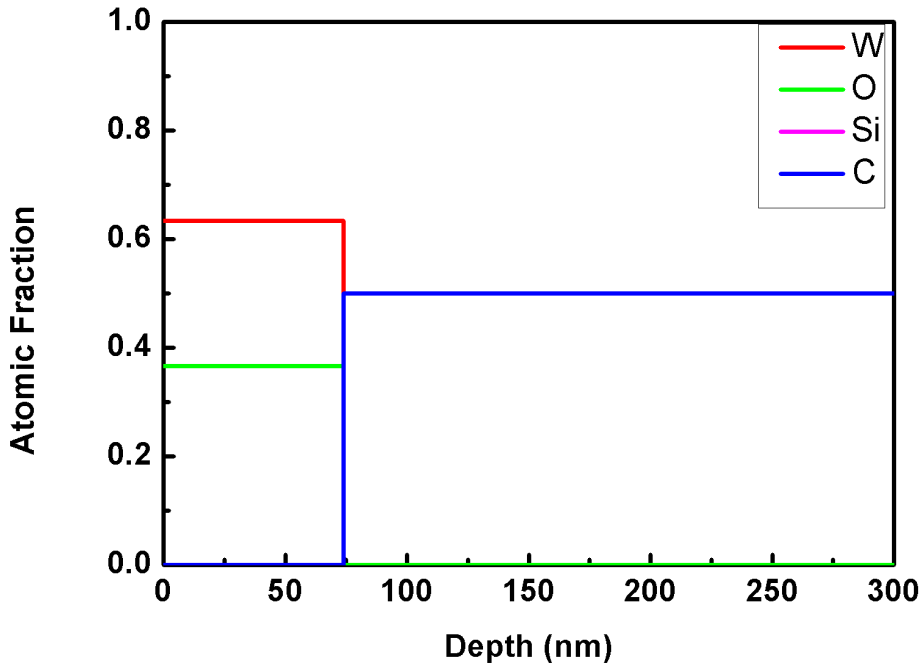

Figure 7-2: *Variation of elemental atomic fraction composition with layer thickness of the as-deposited W-SiC obtained from RUMP simulation.*

In the first layer the amount of W was 69.8 % and the amount of WO_3 was 30.2%. In Fig. 7-2 the silicon profile is not seen because it is overlapping with the C layer (Si and C concentrations/profiles are equal in this case). In the graph where the Si is equal to C, it represents SiC substrate from a depth of about 73.8 nm. Thus, Figure 7-2 shows a W layer with incorporated oxygen on a SiC substrate.

7.1.2 Grazing Incident X-ray Diffraction

GIXRD patterns of W deposited on 6H-SiC substrate before annealing are shown in figure 7-3. The as-deposited sample had broad W peaks at 40.3° and 73.4° attributed to the (110) and (211) planes. WO_3 (140) peak at 49.0° was also observed. The W broad peaks on the as-

deposited might be due to the nano-particle size effect [4][5]. The nano-particle size effect takes place when a nano-material fails to converge to the diffraction line because the lattice sum of the atoms is small, leading to broad peaks.

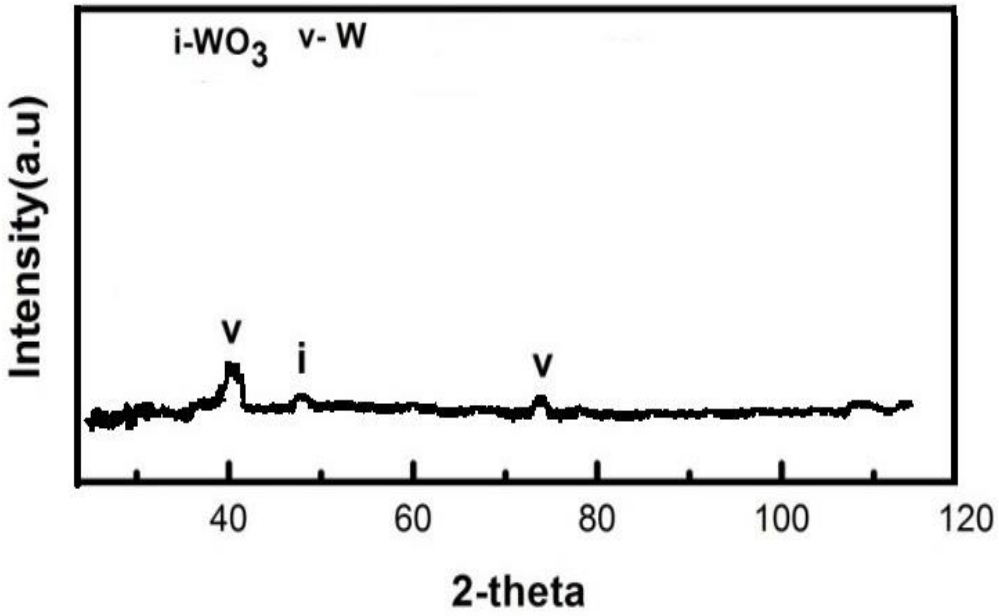

Figure 7-3: *X-ray diffraction patterns of the as-deposited W-SiC.*

The SEM images (see the next section) confirmed the presence of very small W grains. The presence of WO_3 indicates oxidation of W, which correlates with RBS results.

7.1.3 Scanning Electron Microscopy and Atomic Force Microscopy

The SEM micrographs of the as-deposited sample in figure 7-4 (a) displays a fairly uniform surface of the W thin film. The W thin film is composed of very small grains that are evenly distributed and cover the whole 6H-SiC substrate. The ratio between the substrate temperature and the melting point of the target (T/T_M) can be related to the surface morphology which results into grains (granular surface structure) [6]–[8]. Thornton [7] reported that a columnar grain structure will result if the ratio (T/T_M) is below 0.3. In this case the ratio (T/T_M) was 0.08, since W has a melting point of 3695 K and the substrate

temperature was about 298 K during deposition. The value clearly falls under the columnar grain morphology region.

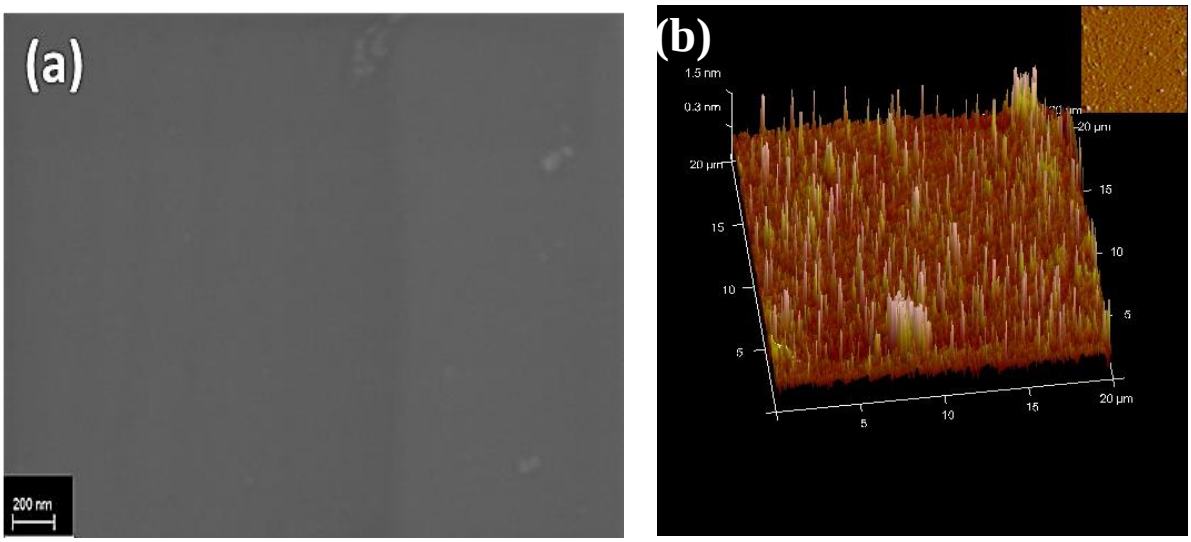

Figure 7-4:*(a) SEM micrograph of W-SiC of as-deposited sample and (b) AFM 3D micrograph and the 2D image inclusion of the as-deposited sample.*

The 2D insert AFM image in figure 7-4 (b) indicates a fairly flat surface with tiny grains which are distributed evenly. This shows that the thin W film deposited was polycrystalline. These results are in agreement with the SEM and XRD findings. SEM image for the as-deposited showed tiny grains covering the SiC substrate and XRD patterns had broad peaks. These indicate the sample was polycrystalline and composed of nano-particles. The R_{rms} of the as-deposited sample obtained from AFM was 0.4 nm. This indicated that the surface was fairly smooth.

7.2 Vacuum Annealing

7.2.1 Rutherford Backscattering Spectrometry

The RBS spectra of the W thin film before and after annealing for 1 hour at 700 °C, 850 °C and 900 ºC are depicted in figure 7-5. The results for the sample annealed at 800 °C were

similar to the sample annealed at 700 °C. Thus, only 700 °C is discussed. The RBS spectra of samples annealed at 700 °C and 800 ºC (not shown here) matched the as-deposited spectrum. However, the depth profile from RUMP simulation (figure 7-6) of the 700 °C spectrum indicates a intermix layer of about 24.1 nm wide.

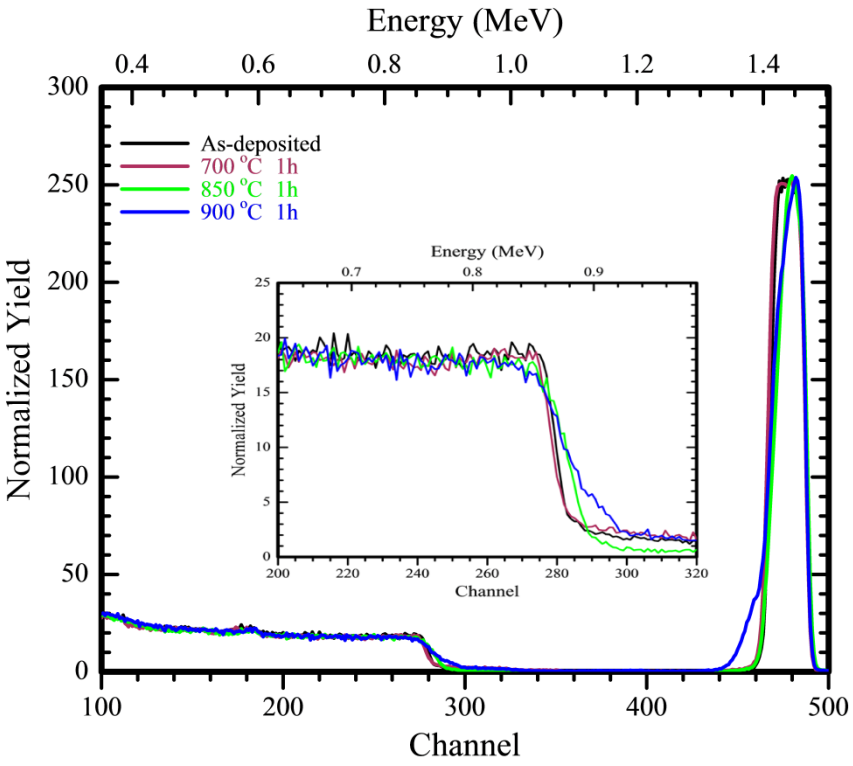

Figure 7-5: *RBS spectra of as-deposited W-SiC sample compared with those annealed at 700 °C, 850 °C and 900 ºC for 1 hour and insert of magnified Si signal from channel numbers 200 to 320.*

This implies that inter-diffusion between W and SiC had occurred during annealing at this temperature. The results showed a reduction in the oxygen content when compared to the as-deposited from 36.6 at.% to 23.6 at.%. Three layers were observed: the W-O layer, the intermixed layer and SiC substrate layer for the 700 °C annealed sample. The initial annealing at 700 °C led to a formation of an intermixed layer of 24.1 nm as the second layer, the first layer's width, decreased to 63.3 nm. The first layer had 23.6 at.% of O and 76.4 at.% of W, while the second layer had 33.4 at.% W, 33.3 at.% C and 33.3 at.% Si. The amount of

Si, C and W which inter-diffused to the reaction zone (RZ) was the same. The XRD result in section 7.2.2 indicates that a reaction took place to form WC and CW_3. This means that SiC decomposed due to the presence of W and only the C reacted with W.

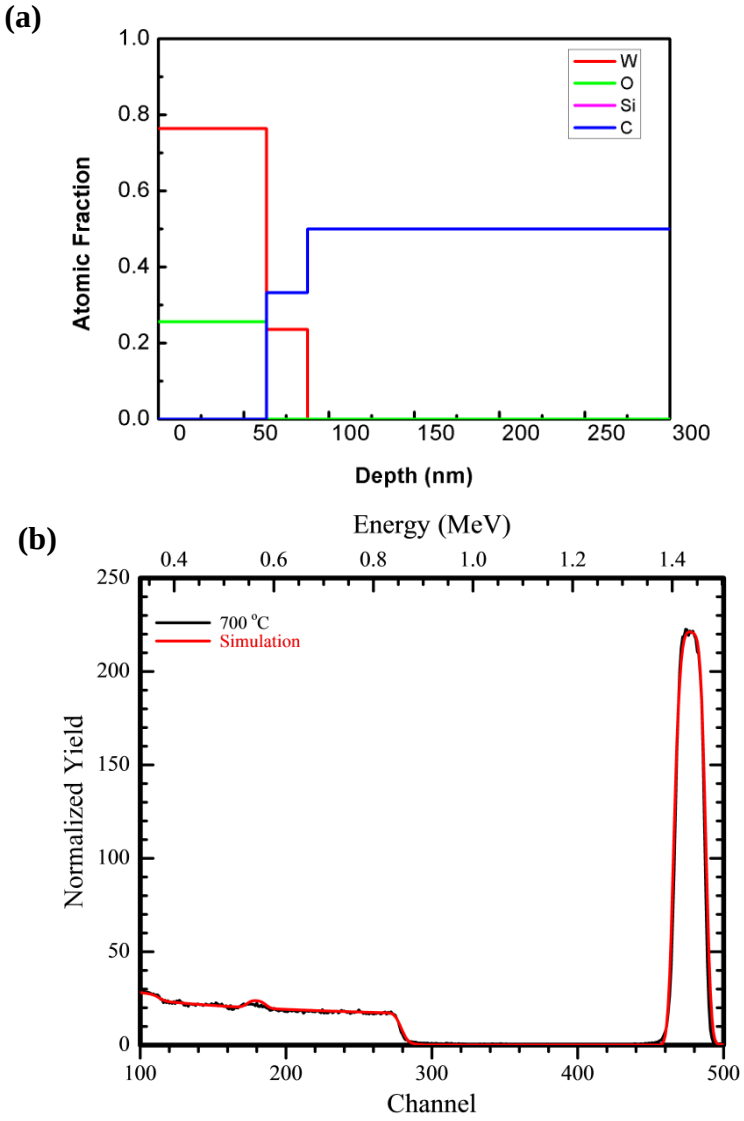

Figure 7-6: *(a) Variation of elemental atomic fraction composition with layer thickness of the W-SiC sample annealed in vacuum at 700°C for 1h. (b) Raw RBS data with RUMP simulated spectrum for the sample annealed at 700 °C 1h.*

The intermixed layer is referred to as RZ, where W and SiC have reacted to form new compounds. In the first layer WO_2 was about 35.4 % and W was about 64.6 %. In the second layer there is 16.7 % WC, 33.4 % CW_3, 16.6 % C and 33.3 % Si.

The RBS spectrum of samples annealed at 850 °C indicated a reduction in the W peak height at the low energy channels. Concurrently, a shift of the Si signal towards higher energy channels was also observed after annealing at this temperature. This observation implied that a reaction between W and SiC at the interface was taking place at this temperature. The intermixed layer consisting of the mixture of W, Si and C of about 26.5 nm wide was observed and is shown in figure 7-7 (a).

The simulation results indicated that the sample was composed of three layers: in the first layer the width was about 45 nm, the second layer width was 26.5 nm and the third layer was the SiC substrate. The following phases were present: 32.5% W, 30.0 % WO_2, 7.5 % WSi_2, 30% WC on the first layer. The second layer had the following phases: 33.4 % of WSi_2, 33.4 % of W_2C, 11 % of Si and 22.2 % of C. These phases were calculated based on the XRD results. Figure 7-7 (a) indicates that Si and C had diffused through the reaction zone to the first layer, with the amount of C being higher than the amount of Si. The RUMP simulation showed the atomic concentration of C on the W metal being higher than the atomic concentration of Si after annealing at 850 °C. This means that C diffuses faster than Si. The diffusion of C faster than Si to the W metal through the RZ upon annealing was also observed by Geib *et al.* [9]. The results observed by Geib supports the results observed in this study of C diffusing faster than Si.

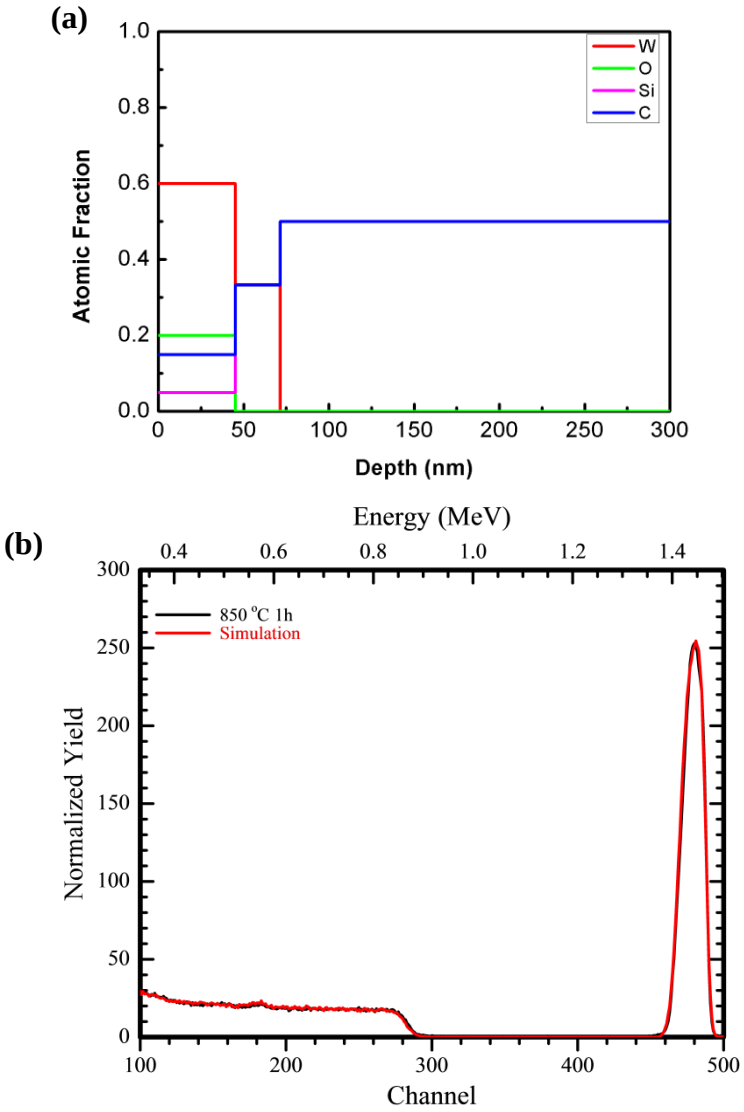

***Figure 7-7**: (a) Variation of elemental atomic fraction composition with layer thickness of the W-SiC sample annealed in vacuum at 850°C for 1h. (b) Raw RBS data with RUMP simulated spectrum for the sample annealed at 850 °C 1h.*

Annealing at 900 °C caused a further reduction in height at the top low energy edge of the W peak. This resulted in a step appearing at the bottom of the W peak extending towards lower energy channels. A further shift of the Si signal towards higher energy channels was also observed after annealing at this temperature. These results indicated that the interactions between W and SiC took place at the interface after annealing at 850 ºC, which led to further widening of the interaction region after annealing at 900 ºC. An increase of C and Si in the

metal layer was observed after annealing at 900 °C. The C was more than the Si in the W metal layer. The reduction of oxygen from 20 % at 850 °C to 10 % after annealing at 900 °C was observed (see figure 7-7 and 7-8). This suggests that annealing the samples in vacuum causes oxygen content to reduce.

The peak height at the surface of the W thin film did not change when compared to 850 °C, indicating that tungsten oxide was still present at the surface. The thickness of the first layer at 900 °C was 36.0 nm and for the second layer was 55.5 nm. The first layer (of about 36.0 nm) consisted of the following phases: 15.0 % WO_2, 18 % WSi_2, 66.0% W_2C, 1.0 % W. The second layer had the following phases: 33.3 % of WSi_2, 33.5 % of W_2C, 11.1 % of Si and 22.2 % of C. In figure 7-8 (a) it is evident that W diffused through the RZ to the SiC substrate.

The sample annealed at 1000 °C shown in figure 7-9 had the following phase composition: the first layer consisted of W_2C which is 27 %, WSi_2 of about 49.2 % and C of 23.8 %. Second layer has the following composition: 33.3 % of WSi_2, 33.4 % of W_2C, 11.1 % of SiC and 22.2 % of C. The width of the first layer was 47.9 nm and that of the second layer was 24.1 nm. Annealing at 1000 °C led to the removal of oxygen, as no oxygen was detected by the RBS. The W was fully consumed by Si and C after annealing at 1000 °C. The amount of C and Si in all the layers was the same. It should be noted that there are more than 3 layers after annealing at 900 °C and 1000 °C, and the other layers were not considered as the amount of W present was very small.

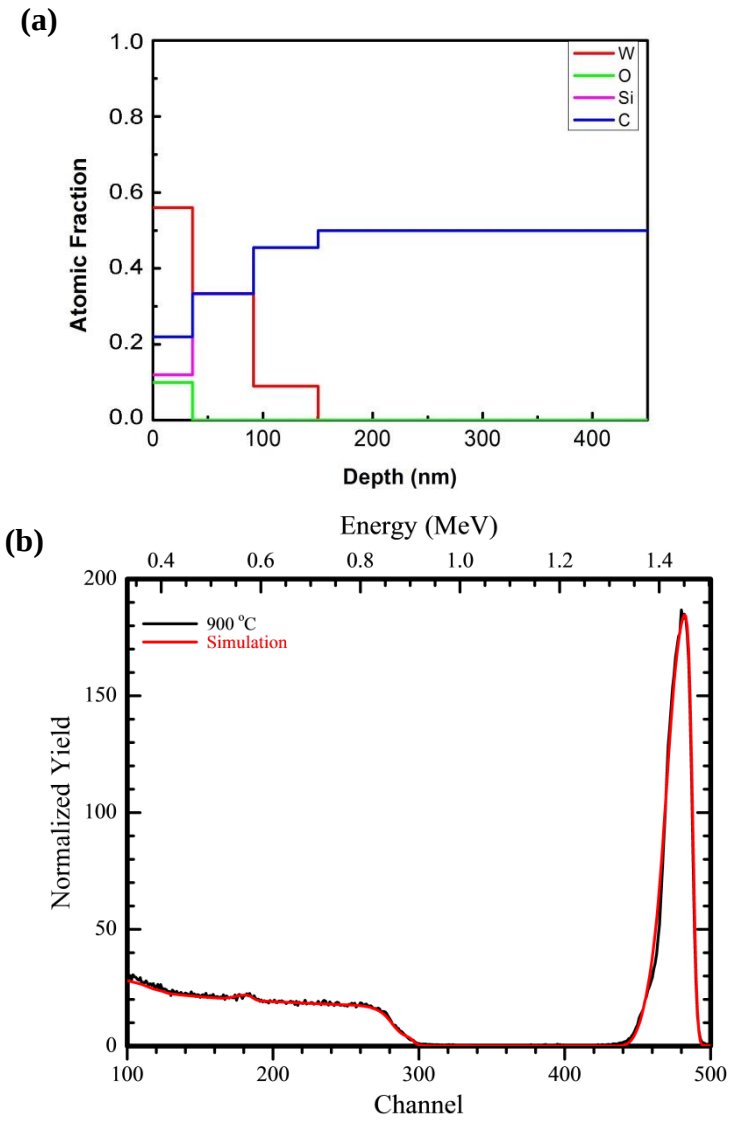

Figure 7-8:*(a) Variation of elemental atomic fraction composition with layer thickness of the W-SiC sample annealed in vacuum at 900 °C and (b) raw RBS data the sample annealed at 900 °C 1h with a RUMP simulation spectrum.*

The oxygen profile reduced with increase in temperature (from 700 °C to 900 °C) when compared to the oxygen peak of the as-deposited sample. This was seen from the increase in the W concentration in RUMP simulation. At 1000 °C the oxygen peak had completely disappeared. This means that the amount of oxygen in the sample annealed at 1000 °C might

be below the RBS detection limit. The vacuum annealing furnace might contain some trace reactive gases which, in the case of hydrogen, then consecutively react with WO_3 as follows:

$$WO_3 + H_2 \rightarrow WO_2 + H_2O \quad (7.0a)$$

$$WO_2 + 2H_2 \rightarrow W + 2H_2O \quad (7.0b)$$

The Si and C were seen to diffuse at different rates upon annealing. C was initially seen to diffuse faster than Si, as it is found in the W metal layer to be more than Si. Increasing the temperature also resulted in the increase of the amount of C and Si diffusing to the W metal, but C was still more than Si. Annealing at 1000 °C led to the diffusion of more Si into the W metal. After annealing at 1000 °C, all the concentrations in the different layers gave the same atomic percentage for Si and C i.e stoichiometry. Thus Si/C ratio shows that no Si or C was lost during annealing.

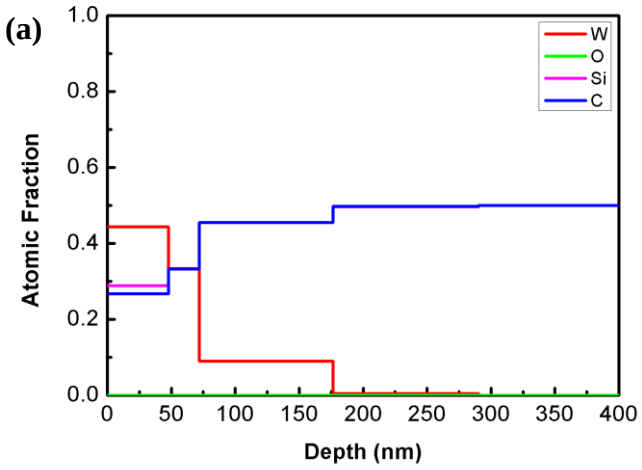

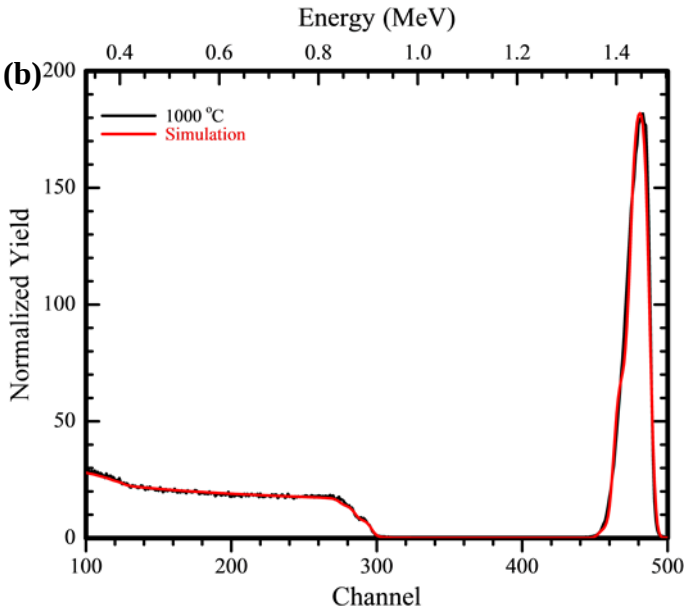

Figure 7-9: *(a) Variation of elemental atomic fraction composition with layer thickness of W-SiC annealed at 1000°C for 1h in vacuum. (b) The raw and simulated RBS spectra of the sample annealed at 1000 °C.*

7.2.2 Grazing Incident X-ray Diffraction

XRD patterns of W deposited on SiC substrate before and after vacuum annealing are shown in figure 7-10. The as-deposited sample was discussed in subsection 7.1.2. Annealing at 700 ºC resulted in appearance of broad diffraction peaks at 2θ position of 58.4° and 100.8°, attributed to the (200) and (310) planes of the W phase reflections, respectively. The appearance of W peaks indicates that the crystallinity of the W thin film improved after annealing. The CW_3 peaks at 2θ position 67.3º and WC peaks (at 48.1º and 52.5º) were also observed. These results indicate that a reaction responsible for the formation of carbides had occurred at this temperature. In this study, the formation of carbides after annealing at 700 ºC in vacuum was observed. Peaks indexed to WO_2 at 36.9º and 79.2° indicate a change in from WO_3 to WO_2 at this annealing temperature.

The heat of formation for the phases in the W-Si-C system, the ternary diagrams and Ellingham diagrams of the reactions in the W-Si-C system have been reported by Seng [10]. From these ternary phase diagrams WC and WSi_2 are expected to be the initial phases at temperature lower than 970 K (~700°C) and they have favourable kinetics. In this study, at an annealing temperature of 700 °C, CW_3 and WC were the initial phases to form with no formation of silicide at the W-SiC interfaces.

After annealing at 800 ºC, peaks indexed to CW_3 at 44.3º and WC at 48.5º were observed. This was accompanied by the disappearance of the WC peak at 52.5º and the appearance of tungsten peaks at 73.4° and 100.8º.

After annealing at 900 ºC and 1000 ºC, a peak indexed to WSi_2 appeared at 26.3º 2θ position and a WO_2 peak at around 54.1º were observed. The peak height (intensity) of W peaks at 900 °C and 1000 ºC increased with increasing temperature. The change in the peak intensity might be due to the change in the nature of W becoming more crystalline. The WC and CW_3 peaks disappeared and the W_2C phase was formed at 900 ºC and 1000 ºC with 2θ peak position at 87.5º. These results indicate that WC and CW_3 were not stable at 900 °C and 1000 ºC. The reactions which have taken place leading to the phase formation can be expressed as follows by equation (7-1), (7-2) and (7-3):

$$20\ W + 10\ C \rightarrow 5\ CW_3 + 5\ WC \qquad (7\text{-}1)$$

$$5CW_3 \rightarrow WC + 14W \qquad (7\text{-}2)$$

$$5W + 2SiC \rightarrow 2W_2C + WSi_2 \qquad (7\text{-}3)$$

Reaction (7-1) occurs for the samples annealed from 700 °C to 800 °C, but this reaction can occur at temperatures higher than 800 °C as can be seen from the table 7-1. At annealing temperatures of 700 °C and 800 °C, W reacts with C to form carbides.

Table 7-1: Change in Gibbs free energy ΔG for some possible reactions between RT to 1000 °C.

			Δ*G*	**(kJ/mol)**	
Reaction	**RT**	**700 °C**	**800 °C**	**900 °C**	**1000 °C**
$20W + 10C \rightarrow 5CW_3 + 5WC$	-191.8	-179.1	-177.8	-176.5	-175.3
$5CW_3 \rightarrow WC + 14W$	-38.2	-35.8	-35.5	-35.3	-35.1
$5W + 2SiC \rightarrow 2W_2C + WSi_2$	6.8	-1.7	-5.2	-9.1	-13.3

Reaction 7-2 occurs after annealing at 850 °C. Annealing at 900 °C causes the tungsten rich carbide to break down to WC and W. The W then reacts with SiC to form WSi_2 and W_2C. Reaction 7-3 takes place for the samples annealed from 850 °C to 1000 °C. Table 7-1 gives the Gibbs free energy Δ*G* for possible reactions between room temperature (RT) to 1000 °C. It shows the formation of WSi_2 and W_2C at annealing temperatures 700 °C. It also indicates that reaction (7-1) can take place during deposition, at 700 °C, 800 °C, 900 °C, 1000 °C, etc. But from the experimental results, reaction (7-1) was favoured at annealing temperatures of 700 °C and 800 °C. The Δ*G* for Reaction (7-3) indicates that this reaction can occur at 700 °C, but mostly preferred at 1000 °C, since at 1000 °C this reaction has the lowest Δ*G*. From the XRD results reaction (7-3) was observed at 900 °C and 1000 °C.

Previously, Baud *et al.* [11] reported that annealing W thin films deposited on SiC at 950 ºC in vacuum resulted in the formation of W_5Si_3 and W_2C. However, in this study, only WSi_2

and W_2C were observed after annealing at 900 °C. Rogowskia *et al.* [12] observed WSi_2 and W_5Si_3 phases after annealing W-SiC contacts in Ar ambient at 700 °C, and at temperatures above 1000 ºC, WSi_2 was the only silicide. The formation of WSi_2 reported in this study has also been observed by Goesman *et al.* [13] and Seng *et al.*[10] at temperatures above 700 °C.

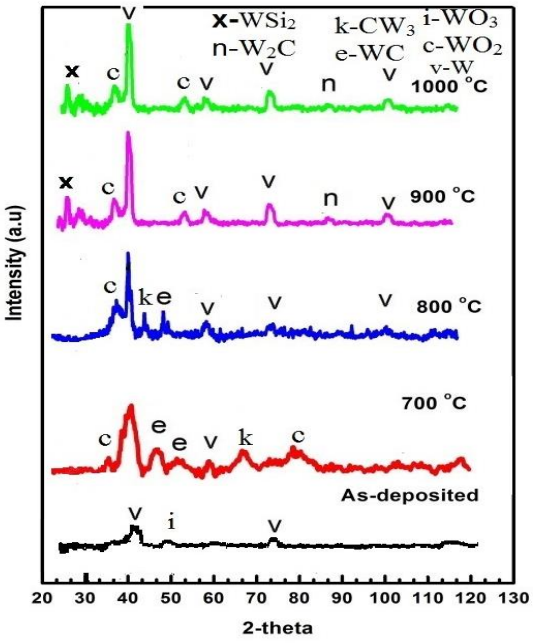

Figure 7-10: *X-ray diffraction patterns of W-SiC sample before and after annealing at 700 ºC, 800 ºC, 900 °C and 1000 ºC in vacuum.*

The driving force of the reactions is usually the thermodynamic and/or kinetic factors at the interface [14]. For a reaction to take place between W and SiC, the bond between Si and C must be broken to form Si and C atoms, which will react with W to form silicides and carbides [15]. When SiC is in contact with a metal, the enthalpies of formation for carbides and silicides along with kinetic factors determine if a reaction would occur. The Si and C atoms then migrate into the W layer and vice versa, leading to the formation of carbides and silicides.

It was observed from previous studies that W films which were deposited on SiC (with the thickness above 150 nm) and annealed in vacuum resulted in the formation of W_5Si_3 as the initial silicide [11][16], whereas W films with thickness less than 100 nm resulted in the formation of WSi_2 [9]. In this case, W thin films of about 73.8 nm was deposited on SiC which resulted in the formation of WSi_2 silicide, as expected. In thicker films, more W atoms are available and therefore W-rich silicides appear as initial phases as opposed to Si-rich phases. In this study, the W film was 73.8 nm thick, so Si-rich silicide (WSi_2) will be the first silicide to appear at the reaction zone.

Table 7-2 shows the calculated average crystal sizes from XRD results using the Scherrer's equation. It shows a decrease in W grain size with increase in annealing temperature. The as-deposited W grain size was 13.1 nm and decreases to 11.0 nm after annealing at 700 °C. The average grain sizes was observed to decrease further after annealing at 800 °C (6.6 nm), 900 °C (6.5 nm) and 1000 °C (6.1 nm). Generally, annealing leads to increase in crystal sizes [17], however, the formation of new phases (all containing W) had grown in a parasitic (at the expense of W) manner, reducing the average W crystal sizes.

The WC and CW_3 average crystal sizes increased when the annealing temperature was increased from 700 °C to 800 °C. More explicitly, The WC crystal size increased from 2.4 nm to 8.2 nm and that of CW_3 changed from 3.1 nm to 10.3 nm. The WO_3 in the as-deposited samples changed to WO_2 after annealing at 700 °C with increase in crystal size from 2.6 nm at 700 °C to 5.1 nm at 1000 °C. WSi_2 and W_2C appeared after annealing at 900 °C. WSi_2 had a crystal size of 9.7 nm at 900 °C, which increased to 10.5 nm after annealing at 1000 °C. The crystal size of W_2C at 900 °C was 1.2 nm, and also increased to 4.8 nm after annealing at 1000 °C. In summary, the decrease in crystal size of W after annealing at 700 °C could be

due to the reaction of W with SiC to form CW_3 and WC. The average crystal sizes of CW_3 and WC increased upon annealing at 800 °C, leading to a further decrease in W average crystal size. The phases which formed, acted as impurities which hindered the W crystal growth. At 900 °C, W_2C and WSi_2 phases formed resulting again in a further decrease of W average crystal size (from 6.6 nm to 6.5 nm). The average crystal size after annealing at 1000 °C of W_2C and WSi_2 increased from 1.2 nm and 9.7 nm to 4.8 nm and 10.5 nm, respectively. WO_2 average crystal size increased with annealing temperature.

Table 7-2: Average crystal sizes of the tungsten, silicides, oxides and carbides crystallites calculated from the XRD patterns of the vacuum annealed samples.

Temp	W (nm)	WC (nm)	CW_3 (nm)	W_2C (nm)	WSi_2 (nm)	WO_3,WO_2 (nm)
As-deposited	13.1	0	0	0	0	4.1
700 °C	11.0	2.4	3.1	0	0	2.6
800 °C	6.6	8.2	10.3	0	0	3.4
900 °C	6.5	0	0	1.2	9.7	5.1
1000 °C	6.1	0	0	4.8	10.5	5.1

In a sample where more than one phase is present, annealing can cause some of the phases to act as impurities to other phases [18][19].

7.2.3 Scanning Electron Microscopy

Figure 7-11 shows the high magnification SEM micrographs of W thin film deposited on 6H-SiC (0001) before and after annealing. The SEM images of the sample annealed at 700 ºC is shown in figure 7-11 (b) which shows the formation of randomly orientated needle-like crystals covering the surface of W thin film. These needle-like crystals could be WO_2 as identified by the XRD patterns and have been described as “nanowires” by other researchers

[20], [21]. The needle-like structure results from the expulsion of the tungsten oxide towards the surface and precipitates on the surface. This leads to tungsten oxide being distributed throughout the surface in the form of needles.

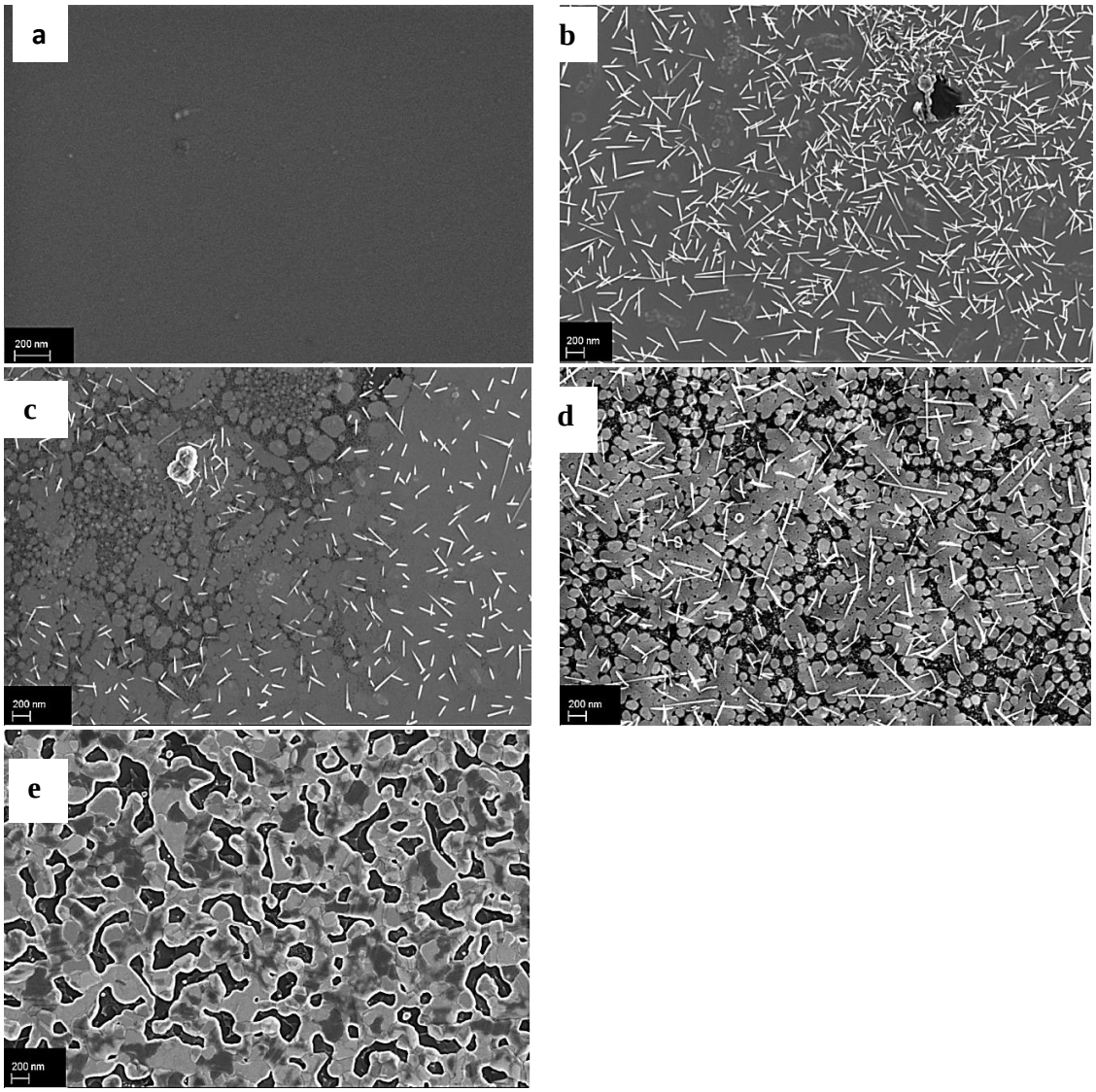

Figure 7-11: *SEM micrographs of W-SiC of (a) as-deposited; vacuum annealed samples for 1 hour at (b) 700 ºC, (c) 800 ºC, (d) 900 ºC and (e) 1000 ºC.*

The SEM micrographs indicate that underneath these needle-like structures, agglomeration of the W grains occurred after annealing at 700 ºC compared to the as-deposited samples. There was also a larger range of grain sizes with some varying shapes.

Annealing at 800 ºC resulted in the formation of W islands as seen in figure 7-11 (c). The surface became increasingly rough and uneven grain growth was observed with increase in annealing temperature. The WO_2 needle-like structures were still present after annealing at 800 °C but with a decrease in quantity. For sample annealed at 900 ºC, depicted in figure 7-11 (d), W thin film was no longer homogenous with increase in island structure on the surface. This island formation might be due to the different phases forming at this temperature, as shown in the XRD results discussed in the previous section, where W reacted with SiC to form both silicides and carbides.

At 1000 ºC, the WO_2 needle-like crystals that were observed at lower temperatures were no longer visible. Only flat crystals with spaces in-between were visible. A difference in contrast was observed on the surface which confirms the possible formation of silicides, carbides or oxides.

7.2.4 Atomic Force Microscopy

AFM images of the as-deposited and the samples annealed from 700 °C to 1000 °C are depicted in figure 7-12. After annealing at 700 °C, the 2D insert shows small islands with spherical and rod-like shapes that protrude from the surface (figure 7-12 (b)).

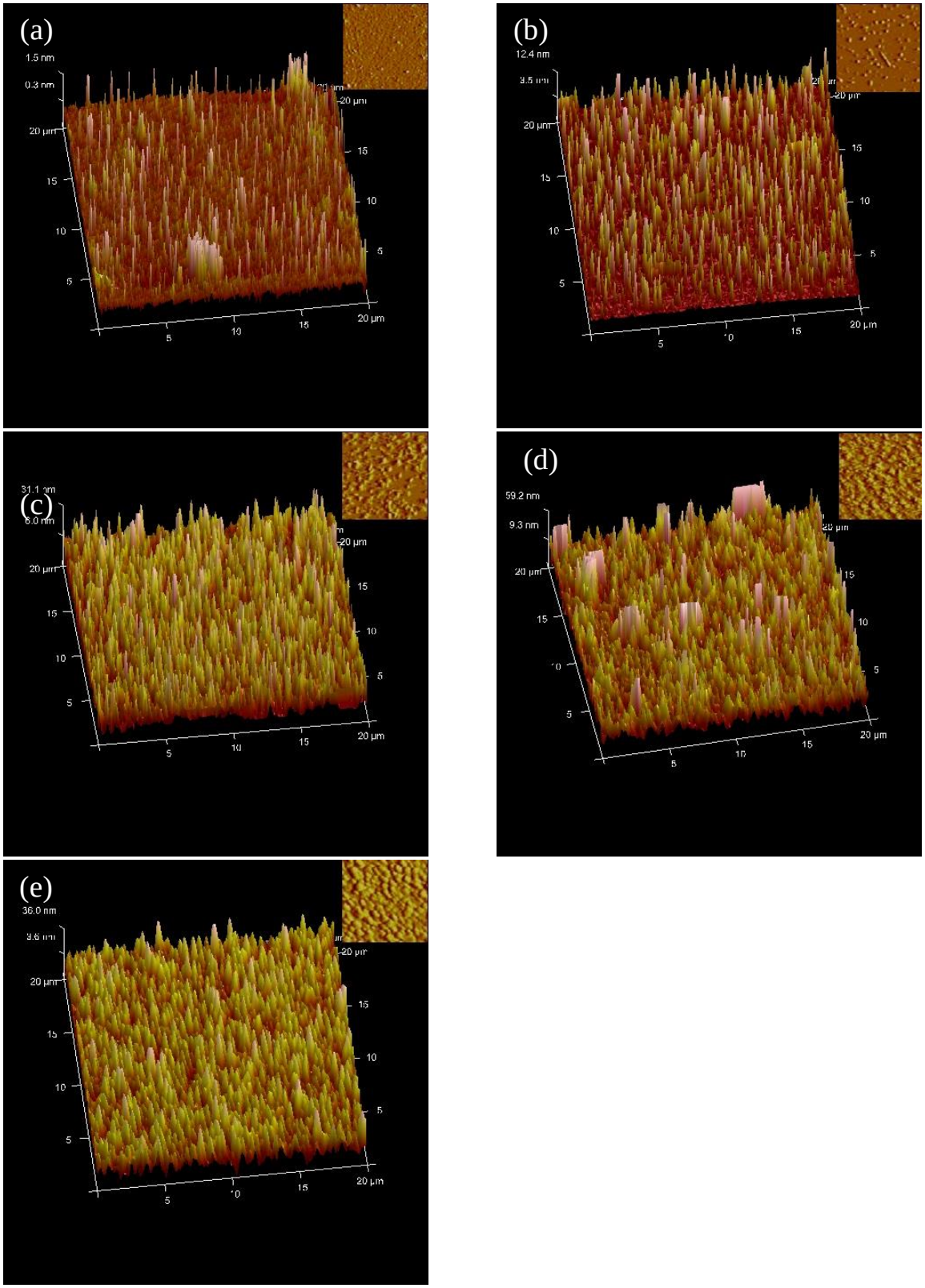

***Figure 7-12**: AFM 3D micrographs and the 2D image insert (a) before and after annealing in vacuum at (b) 700 °C, (c) 800 °C, (d) 900 °C and (e) 1000 °C.*

These islands seem to be on top of the W thin film surface. Similar protruding particles/islands were observed on the SEM image of the samples annealed at 700 °C and were identified as tungsten oxide nanowires by XRD. Increase in annealing temperature (800 to 1000 °C) resulted in increase in the particles/islands covering the surface. The 3D images had irregular hillocks and valleys which grow with increase in annealing temperature.

Table 7-3 shows the root mean square roughness (R_{rms}) and average roughness (R_a) values of the as-deposited sample, annealed at 700 °C, 800 °C, 900 °C and 1000 °C. An increase in roughness with an increase in annealing temperature is observed. This increase is due to interfacial reactions, with tungsten silicides and carbide forming at the interface, causing rearrangements at the interface and on the surface of the W-SiC sample. The peak to valley roughness (R_{pv}) values, which is the vertical distance between the highest and lowest points in the calculated length, increases with increased annealing temperature. This indicates that the sample was indeed becoming rough with increase in annealing temperature.

Table 7-3: The R_{rms}, R_a and R_{pv} values of the W-SiC samples before and after annealing in vacuum.

Temperature (°C)	R_{rms} **(nm)**	R_a **(nm)**	R_{pv} **z- range (nm)**
As-deposited	0.4	0.2	28.0
700	2.3	1.3	32.4
800	7.7	6.2	81.3
900	14.9	10.1	84.2
1000	9.5	7.6	47.9

A representation of the sample roughness with change in temperature is shown in figure 7-13. The R_{rms} is used to measure the average surface roughness. In this figure, it is evident that the surface roughness increases with increase in annealing temperature from 700°C (2.3 nm) to 900 °C (14.9 nm) when compared with the as-deposited (0.4 nm).

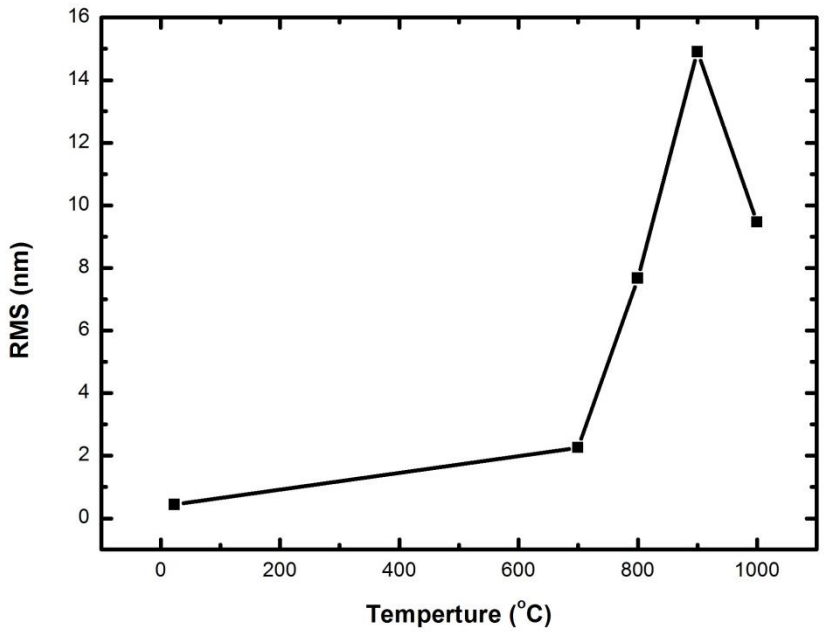

Figure 7-13: *The change in the R_{rms} with annealing temperatures for the samples annealed in vacuum as a function of temperature.*

After annealing at 1000 °C the surface roughness decreases to 6.26 nm due to the change in nature of the surface, from small grain like particles to crystals which look flat but stacked on top of each other and the reduction of the oxide layer as seen from SEM images. The SEM, XRD and RBS are in agreement with the AFM results.

7.3 Hydrogen (H_2) Ambient Annealing

7.3.1 Rutherford Backscattering Spectrometry

The W thin films deposited on 6H-SiC were annealed in H_2 ambient for 1 hour at temperatures ranging from 700 to 1000 ºC. Their corresponding RBS spectra are shown in figure 7-14. The as-deposited W peak has a lower peak height compared to the 700 ºC annealed W peak. The difference between the two spectra might be due to the presence of oxygen in the as-deposited layer.

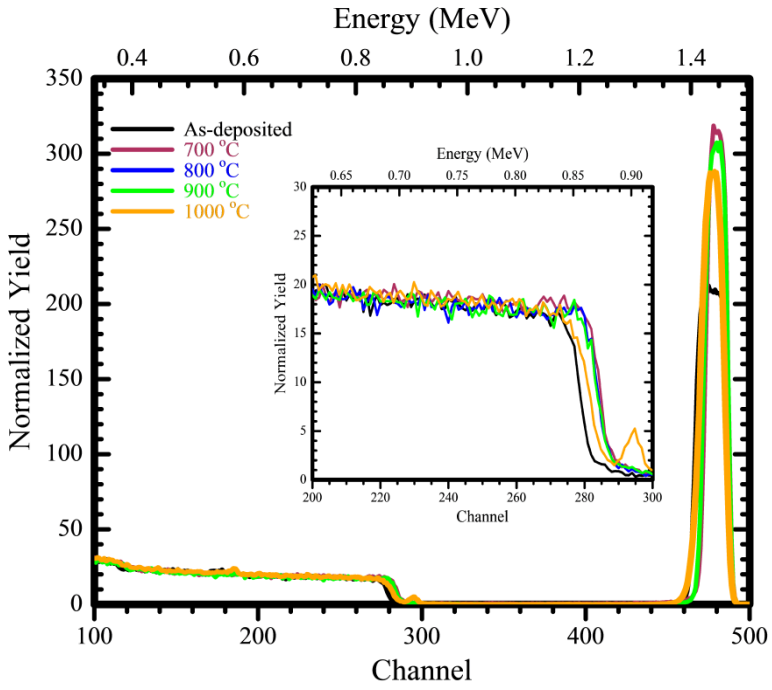

Figure 7-14: *RBS spectra of the as-deposited and annealed samples in H_2 gas for 1 hour at temperatures ranging from 700 to 1000 ºC*

The presence of oxygen in W film reduced the peak height of the RBS spectrum of as-deposited sample. After the oxygen content was reduced in the W film, the height of W peak increased as seen in figure 7-14.The increase in W peak height after annealing in hydrogen due to the removal of oxygen was also observed by other researchers [22], [23]. There are

two possible explanations for removal of oxygen in the deposited film: (1) during annealing, hydrogen reacts with O to form H_2O according to chemical reactions in equation (7-4), (7-5) and (7-6) [24]:

$$4WO_3 + H_2 \rightarrow W_4O_{11} + H_2O \quad (7\text{-}4)$$

$$W_4O_{11} + 3H_2 \rightarrow 4WO_2 + 3H_2O \quad (7\text{-}5)$$

$$WO_2 + 2H_2 \rightarrow W + 2H_2O \quad (7\text{-}6)$$

(2) carbon from the SiC reacted with oxygen to form carbon dioxide gas which then flowed out of the system together with the H_2 gas [22]. Since this did not happen for the samples annealed in vacuum, the more plausible explanation in this case is the former, i.e. that the H_2 gas reacted with oxygen, leaving a pure W layer. To further investigate whether H_2 reacts with O to form a pure W layer, as speculated above, the W-SiC samples were annealed at 600 ^oC, where no interaction between SiC and W was expected, [11] for 1 hour.

The RBS spectrum and RUMP simulation (figure 7-15) indicated a decrease in W thickness to 30 nm with no oxygen (see figure 7-15 (a) and (b)). The loss of W might have been due to delamination. This thickness is of the same order of magnitude as the 700 °C one where some W delaminated was also observed. No interactions between W and SiC were detected at 600 °C. The RUMP simulation of the sample annealed at 700 ºC indicated that a reaction had taken place between W and SiC. The reaction at 700 °C resulted in a 20.9 nm wide W layer as the first layer and, with an intermixed second layer of about 11.5 nm thickness (see figure 7-15 (c)).

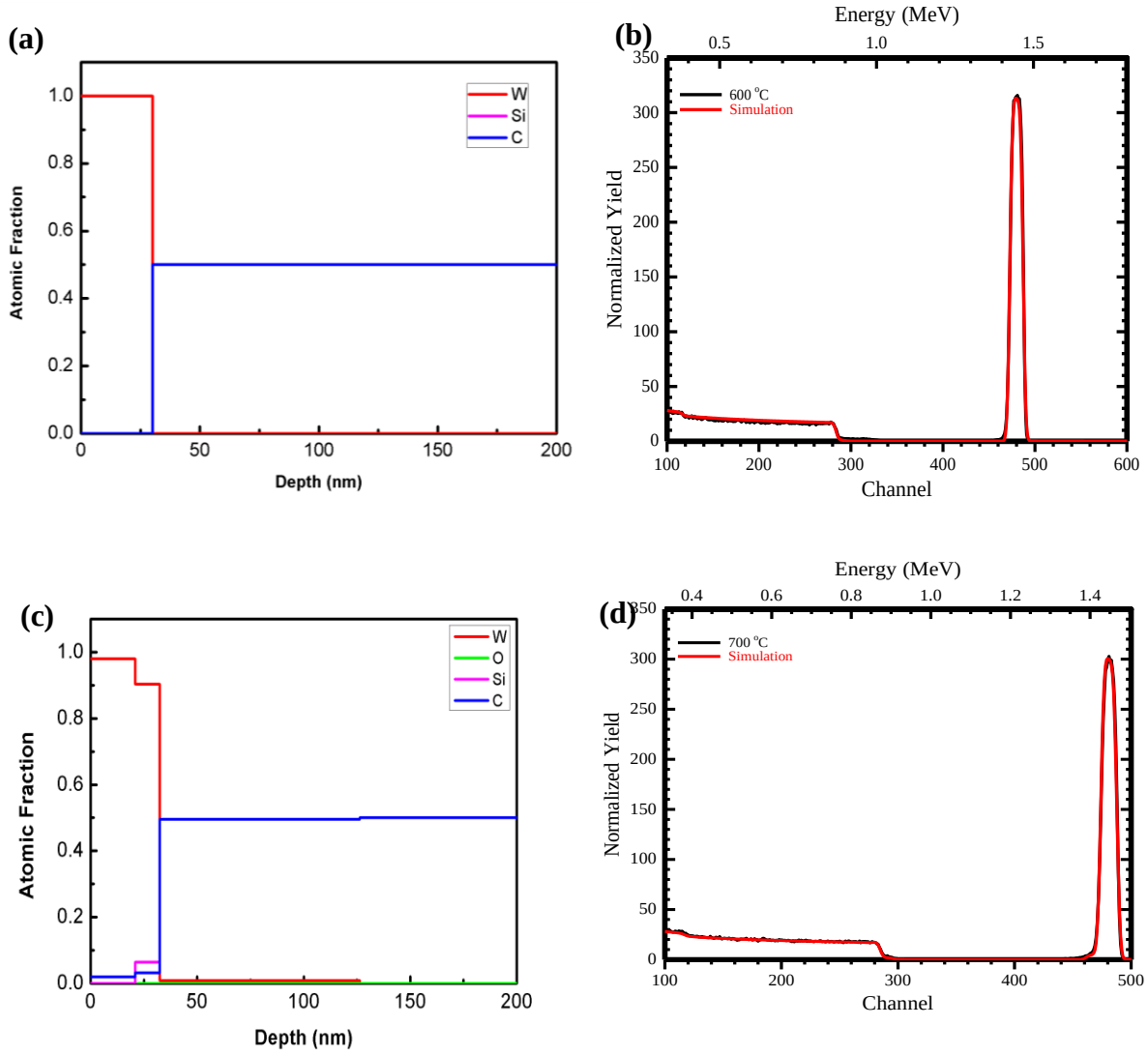

Figure 7-15: *(a) Variation of elemental atomic fraction composition with layer thickness of W-SiC sample annealed in H_2 at 600 °C and (b) RUMP simulated spectrum overlaying the raw RBS data of a 600 °C annealed sample, W-SiC (c) Variation of elemental atomic fraction composition with layer thickness for the samples annealed at 700 °C in H_2 and (d) RUMP simulated spectrum overlaying the raw RBS data of a 700 °C annealed sample.*

A reaction between W and SiC had taken place as a result of the inter-diffusion between W, Si and C. The composition of the RZ was obtained using a RUMP simulation. The RUMP simulations of the first layer suggests the presence of W and WC phases with concentrations of about 96.0 % and 4.0 % ,respectively. From figure 7-15 (c), it can be seen that C diffused through the reaction zone to the W layer.

In the second layer, which is the intermixed layer, the concentrations for W, WC and W_5Si_3 were found to be 76.5 %, 6.4 % and 17.1 %, respectively. These results support that H_2 reacts with oxygen in the deposited W thin film, since no oxygen-related compound was present (like in the as-deposited thin films) or formed during annealing in H_2.

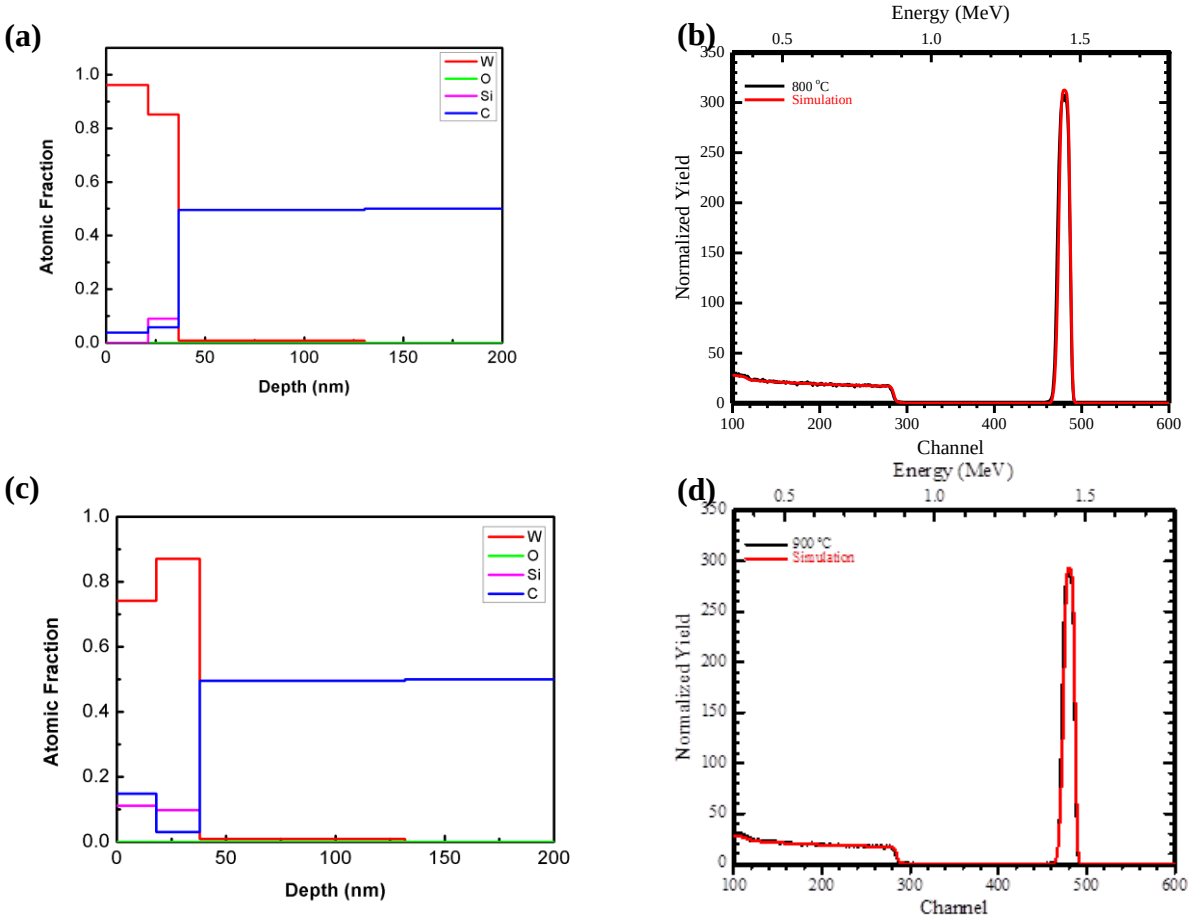

Figure 7-16: *(a) Variation of the elemental atomic fraction composition with layer thickness of W-SiC samples annealed H_2 at 800 °C for 1h. (b) The simulated spectrum are overlaid on the raw RBS data spectrum of the samples annealed at 800 °C. (c) Variation of the elemental atomic fraction composition with layer thickness of W-SiC samples annealed H_2 at 900 °C for 1h. (d) The simulated spectrum are overlaid on the raw RBS data spectrum of the samples annealed at 900 °C.*

A decrease in the height of the tungsten peak after annealing at 800 ºC was observed, indicating that further reactions between W and SiC took place, see figure 7-16 (a and b).

RUMP simulations indicated the presence of C in the W layer. C migrated to the W layer, where it reacted with W to form carbide(s). The diffusion of C into the W layer led to the atomic concentration of Si being higher in the second layer.

The RZ layer increased to a thickness of about 15.3 nm and the W layer containing the diffused C was 21.3 nm thick as a result of further reactions taking place between W and SiC. Similar to the 700 ºC annealed samples, the RUMP simulation for 800 ºC annealed sample had two layers in the RZ from which the percentage of each phase in each layer was determined. The first layer was composed of 92.4 % of W and 7.6 % of WC. The second layer had a concentration of 62.8 % of W, 17.4 % of W_2C, 14.4 % of W_5Si_3 and 5.4 % of WSi_2.

From figure 7-16 (c and d), showing the results for sample annealed at 900 °C, it can be observed that a mixed layer (second layer) of W, Si and C was simulated which was about 19.9 nm. An increase in width in the reaction zone after annealing at 900 °C when compared to the 800 °C annealing was observed. The first layer was composed of 53.7% of W, 29.6% of WC and 16.6% of WSi_2 and the thickness of the layer was 18.1 nm. The second layer (19.9 nm) consists of 69.1% W, 9.3% W_2C, 5.9 % WSi_2 and 15.7% W_5Si_3.

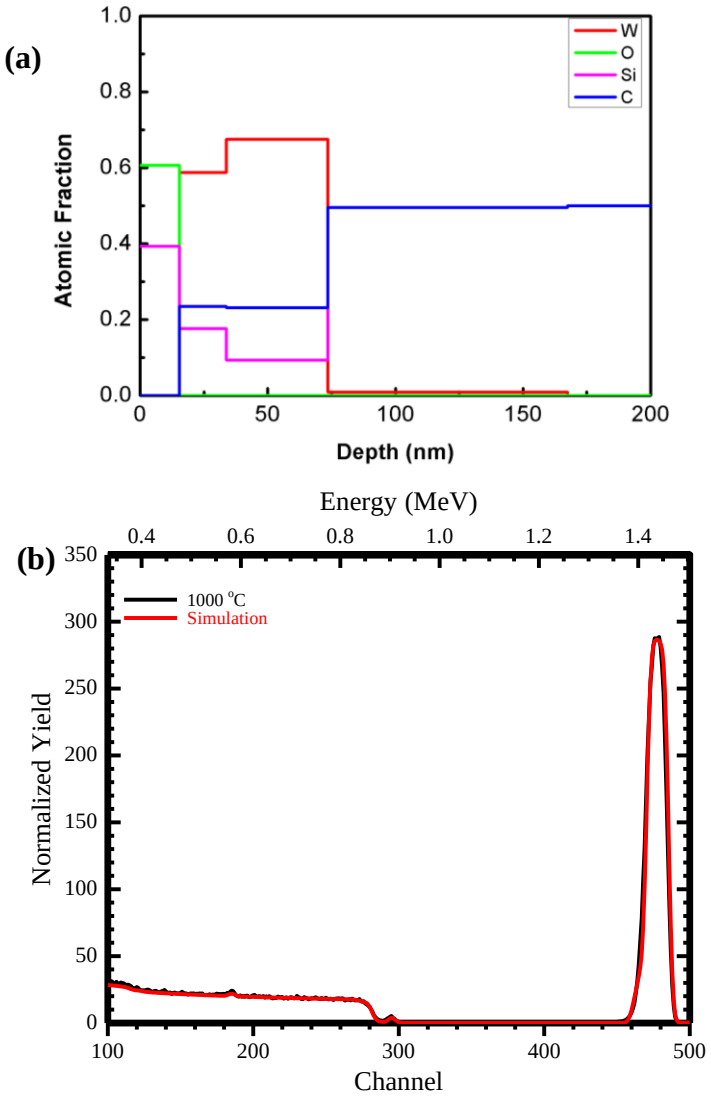

Figure 7-17: *(a) Variation of elemental atomic fraction composition with layer thickness after annealing in H_2 at 1000 °C of W-SiC obtained from RUMP simulation. (b) The overlay spectra of raw RBS data and simulated spectrum at 1000 °C.*

From the RBS spectrum of W-SiC sample annealed at 1000 °C, the presence of oxygen and Si at the surface can be observed (figure 7-17). The Si layer observed on the surface indicated that at 1000 ºC, Si segregated to the surface where it reacted with oxygen to form SiO_2. The RUMP simulation in figure 7-17 indicated that the surface of the samples had a thin layer of about 15.3 nm composed of Si and O_2, serving as a first layer. The reaction zone obtained from the RUMP simulation at 1000 ºC was also composed of three layers with different

quantities of carbides and silicides in the different layers. First layer 100 % SiO_2, and the second layer of 18.4 nm thick had W, WC, and WSi_2 with the following percentages of 26.4 %, 47.0 % and 26.5 %, respectively. The third layer with a thickness of 39.8 nm was composed of 10.7 % W, 66.9 % W_2C, 16.3 % W_5Si_3 and 6.12 % WSi_2. The quantity of the silicide phases (WSi_2 and W_5Si_3) in both layers increased with the increase in annealing temperature whereas the quantity of carbides formed (WC and W_2C) changed with increase in temperature.

C diffused to the W metal layer beyond the RZ upon annealing from 700 °C as shown in figure 7-15(c). The amount of C in the W metal layer increased after annealing at 800 °C. At 900 °C both Si and C are found to be present in the W metal layer, with C being more than Si. During the initial annealing, C diffuses more than Si and is present in both the RZ and W metal layer. This showed that C moved rapidly than Si up to 900 °C. At 1000 °C, Si segregated to the surface to form SiO_2. The movement of Si only occurred once C stop diffusing into the W metal. The amount of Si to C in all the layers becomes almost equal after annealing at 1000 °C. The vacuum and H_2 has shown that C reaches equilibrium with W after annealing at 900 °C, which then allows Si to diffuse through the W metal layer.

7.3.2 Grazing Incident X-ray Diffraction

After RBS analysis, the same samples were examined using XRD at grazing incidence geometry. GIXRD patterns of the W thin film deposited on 6H-SiC before and after annealing are depicted in figure 7-18. The as-deposited sample XRD pattern was discussed in subsection 7-1.2.

The sample annealed at 700 °C resulted in the increase in the W peak and new W peaks at 43.9º, 82.1º and 100.8° 2θ positions attributed to (211), (222) and (310) planes, respectively. The new W peaks could be due to the reduction of the tungsten oxide as suggested by the RBS results where the oxygen peak disappeared after annealing at 700 °C. A reaction was observed to have taken place after annealing at 700 °C, with the formation of carbide and silicide phases. The silicide observed was W_5Si_3 with peaks at 29.5º and 61.6º assigned to (310) and (512) planes, respectively. The carbide formed was WC corresponding to (101) and (100) planes at 2θ position of 35.6º and 48.4º, respectively. The appearance of WO_3 (112) at the 34.3º 2θ position and WO_3 (111) at the 41.9º 2θ position indicates that the film still contained an oxide on the W film.

Annealing at 800 ºC resulted in the decrease of the W-rich silicide (W_5Si_3) peak intensity and the formation of a Si-rich silicide: WSi_2 (224) phase and W_2C (610) at the 2θ positions of 103.3ºand 102.9º, respectively. This implies that a fraction of the W_5Si_3 phase reacted with C from SiC to form WSi_2 and W_2C which resulted in a decrease in W_5Si_3 peak intensity. The possible reactions are represented by equations (7.7), (7.8) and (7.9):

$$33\ W + 15\ SiC \rightarrow 8\ WC + 5\ W_5Si_3 + 7\ C \quad (7.7)$$

$$W_5Si_3 + 3\ C \rightarrow WSi_2 + 2\ W_2C + SiC \quad (7.8)$$

$$5\ W + 2\ SiC \rightarrow WSi_2 + 2W_2C \quad (7.9)$$

Equation (7-7) is applicable to annealing at 700 °C and reactions in equations (7.8) and (7.9) represent the reactions that took place at 800 °C to 1000 °C. Table 7-4 shows that WSi_2 and

W_2C can form during deposition at RT, however, from the experimental data WSi_2 and W_2C formed at temperature up to 800 °C. W_5Si_3 and WC were present in all the annealing temperatures. From the Gibbs energy of formation, it is clear that they are expected to be present in samples annealed in this temperature range.

Table 7-4: Change in Gibbs free energy ΔG for some possible reactions between RT to 1000 °C.

			Δ*G* (kJ/mol)		
Reactions	**RT**	**700 °C**	**800 °C**	**900 °C**	**1000 °C**
$33W+15SiC \rightarrow 8WC+ 5W_5Si_3 +7C$	39.8	-119.3	-142.1	-161.8	-187.8
$W_5Si_3 + 3C \rightarrow WSi_2 + 2W_2C+ SiC$	-62.3	-35.1	-33.7	-32.6	-31.9
$5W + 2 SiC \rightarrow WSi_2 + 2W_2C$	6.8	-1.7	-5.2	-9.2	-13.3

WC (35.6º) peak intensity increased after annealing at 800 ºC compared to the 700 ºC annealing. The increase in the peak intensity at 800 ºC in figure 7-18 is due to the increase in the quantity of WC after further reaction between W and SiC. The disappearance of W peaks at 39.9° and 43.0°, with the appearance of W peak at position 40.2° (101) is observed at after annealing at 800 °C (see figure 7-18). Annealing at 900 °C resulted in a reduction in the WC peak intensity at 35.0° and appearance of W peak at 39.0°.

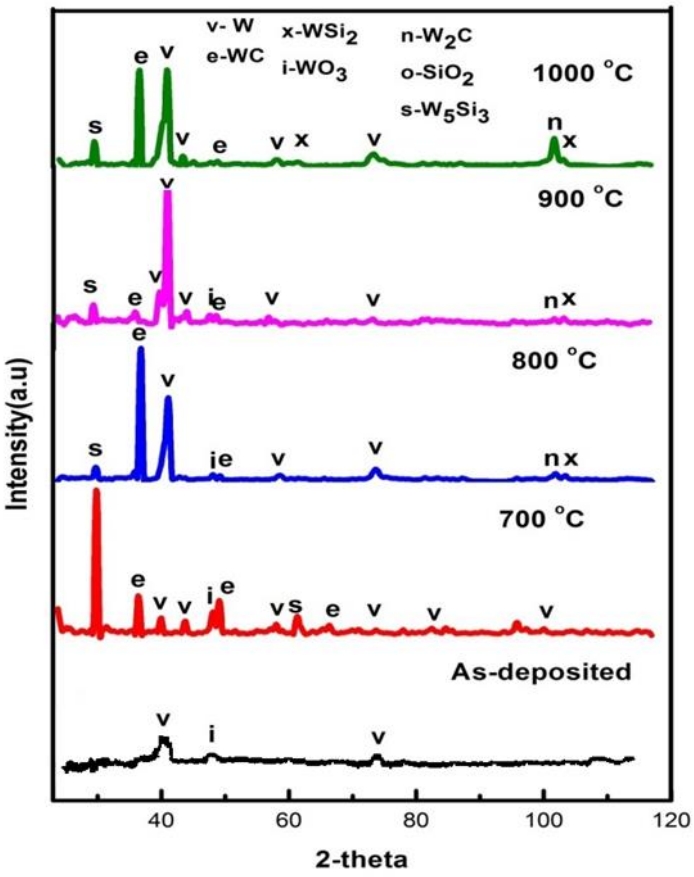

Figure 7-18: *Grazing incidence X-ray diffraction patterns for W-SiC after annealing in H_2 at 700 ºC, 800 ºC, 900 °C and 1000 ºC.*

Annealing at 1000 ºC resulted in an increase in the intensity of the W_2C peak (2θ position 102.9º) compared to that after the annealing at 800 ºC. The change in the W_2C intensity was due to the increase in W_2C volume fraction. An additional peak of WSi_2 at 62.3º was observed, indicating further reactions at the RZ. An increase in the WO_3 and W peak intensities at 41.9° and 41.2°, respectively was due to compound crystallization. The W peaks were still present after annealing at 1000 ºC, indicating that the W layer had not fully reacted. The annealing steps from 700 °C to 1000 °C resulted in a decrease in the peak intensity of WC which might have been due to the formation of W_2C. The WC peak height at 35.6°

increased when the samples were annealed at 700 °C, 800 °C and 1000 °C due to increase in its volume fraction and further reactions.

Table 7-5 shows the average grain size of the phases present before and after annealing. It can be seen that the grain sizes fluctuate with increase in annealing temperature. This is due to the reaction of the phases to form another phase and the rearrangement of the phases formed in the RZ. The W average grain size after deposition was 13.2 nm, which decreased after annealing at 700 °C to 6.7 nm. The decrease in the W peak is due to the presence of impurities, i.e. the phases that formed. The new phases, i.e. W_5Si_3, WSi_2, W_2C and WC all contained W, meaning that they had grown in a parasitic manner from 700 °C to 1000 °C. The crystal size of W_5Si_3 was 11.9 nm, after annealing at 800 °C, it decreased to 10.1 nm. WC crystal size increased from 8.1 nm at 700 °C to 12.2 nm at 800 °C. When the samples were annealed from 900 °C to 1000 °C, an increase in W_5Si_3 crystal size and a decrease in the WC crystal size were observed. WSi_2 and W_2C crystal sizes increased with increase in annealing temperature.

Table 7-5: Average grain size of the tungsten, silicides, oxides and carbides calculated from the H_2 annealed sample XRD patterns.

Temp (°C)	**W (nm)**	**WO_3 (nm)**	**W_5Si_3 (nm)**	**WSi_2 (nm)**	**WC (nm)**	**W_2C (nm)**
As-deposited	13.2	4.1	0	0	0	0
700	6.7	13.5	11.9	0	8.1	0
800	4.8	0	10.1	3.9	12.2	5.2
900	5.9	0	11.4	6.9	7.3	5.8
1000	6.7	0	11.9	7.4	9.1	11.9

In summary this study shows that W_5Si_3 and WC were the initial phases formed after annealing W-SiC at 700 °C, with the WSi_2 only appearing after higher annealing temperatures, i.e. at 800 ºC and above. The formation of these initial phases (W_5Si_3 and WC) have also been observed by other researchers (although the annealing atmospheres were vacuum and Ar) as initial phases [11] [12][25][26], as discussed before. The differences in the phases observed by different researchers are due to the difference in deposition method used and annealing method used. It is clear from annealing in H_2 that the initial preferential phase is not only depended on the thickness of the W layer but also the annealing atmosphere.

7.3.3 Scanning Electron Microscopy

Figure 7-19 shows SEM micrographs of W deposited on 6H-SiC before and after annealing at 700 ºC, 800 ºC, 900 °C and 1000 °C for 1 hour in H_2 ambient. Annealing of the W-SiC samples in H_2 at 700 ºC and 800 ºC for 1 hour led to increase in the size of the grains. The surface structure of the sample annealed at 800 °C has larger grains and more distinct grain boundaries than the sample annealed at 700 °C. Consequently, the surface topography of the W-SiC samples annealed in H_2 at 800 ºC became rougher compared to the 700 ºC annealed sample (see figure 7-19 (b) and (c)). Annealing at 1000 ºC resulted in the formation of hillocks and a much rougher surface compared to the as-deposited. The grain sizes after annealing at 1000 °C are smaller compared to the 900 °C, this was due to the SiO_2 layer formed on the surface. From the RUMP simulation SiO_2 was the first layer covering the W-SiC sample. Tungsten oxide nanowires were not observed on the H_2 annealed samples, since H_2 reacted with oxygen leaving a pure tungsten layer as indicated by the RBS results.

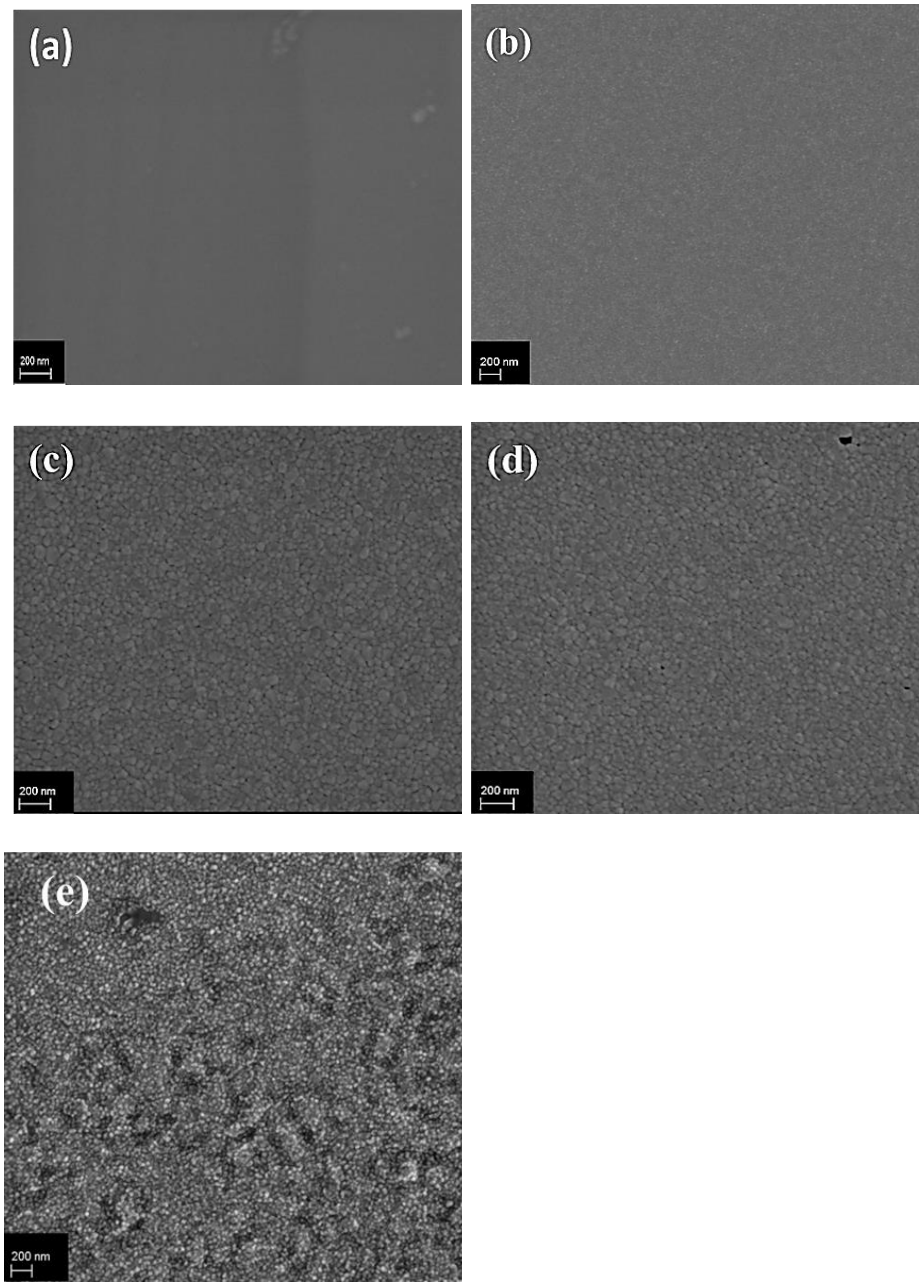

Figure 7-19: *SEM micrographs of (a) As-deposited W-SiC, (b) 700 ºC, (c) 800 ºC , (d) 900 °C (e) 1000 ºC for 1 hour annealed in hydrogen.*

The change in surface topography (from as-deposited to 900 °C) was due to recrystallization of W layer into larger grains and reactions taking place in the W-SiC samples. The SEM results indicate a change in the grain sizes of the sample's surface when annealed at different

temperatures. This confirms that the change in the peak intensities in the XRD results was due to a change in sample structure.

7.3.4 Atomic Force Microscopy

As discussed above in subsection 7.1.3, the AFM surface image of the as-deposited sample was fairly smooth. The samples annealed in H_2 at temperatures ranging from 700 to 1000 °C, shows an increase in average grain size (see the 2D AFM inserted images in figure 7-20). The 2D image after annealing in H_2 indicated a surface composed of granules with different sizes distributed on the sample surface. The granules size appears to be the same after annealing from 700 to 900 °C. At 1000 °C, they appear to have become larger. The 3D height image shows an increase in the particle height with increase in annealing temperature. The surface feature like the clusters and valleys evolve with increase in annealing temperature. Referring to the SEM images in figure 7-19, it was observed that the W grain sizes changed upon annealing, supporting the visible change on the AFM images.

The R_{rms} and R_a values from table 7-6 at 700 °C were 0.83 nm and 0.47 nm, respectively. These values are larger than the as-deposited ones. This was due to the change of the surface, when the atoms of W-SiC sample rearrange themselves which was influenced by the annealing temperature. R_{rms} and R_a values of the samples annealed at 800 °C, 900 °C and 1000 °C were larger compared to the 700 °C annealed sample. The R_{pv} value increases with increase in annealing temperature up to 900 °C. The R_{pv} value decreases after annealing at 1000 °C.

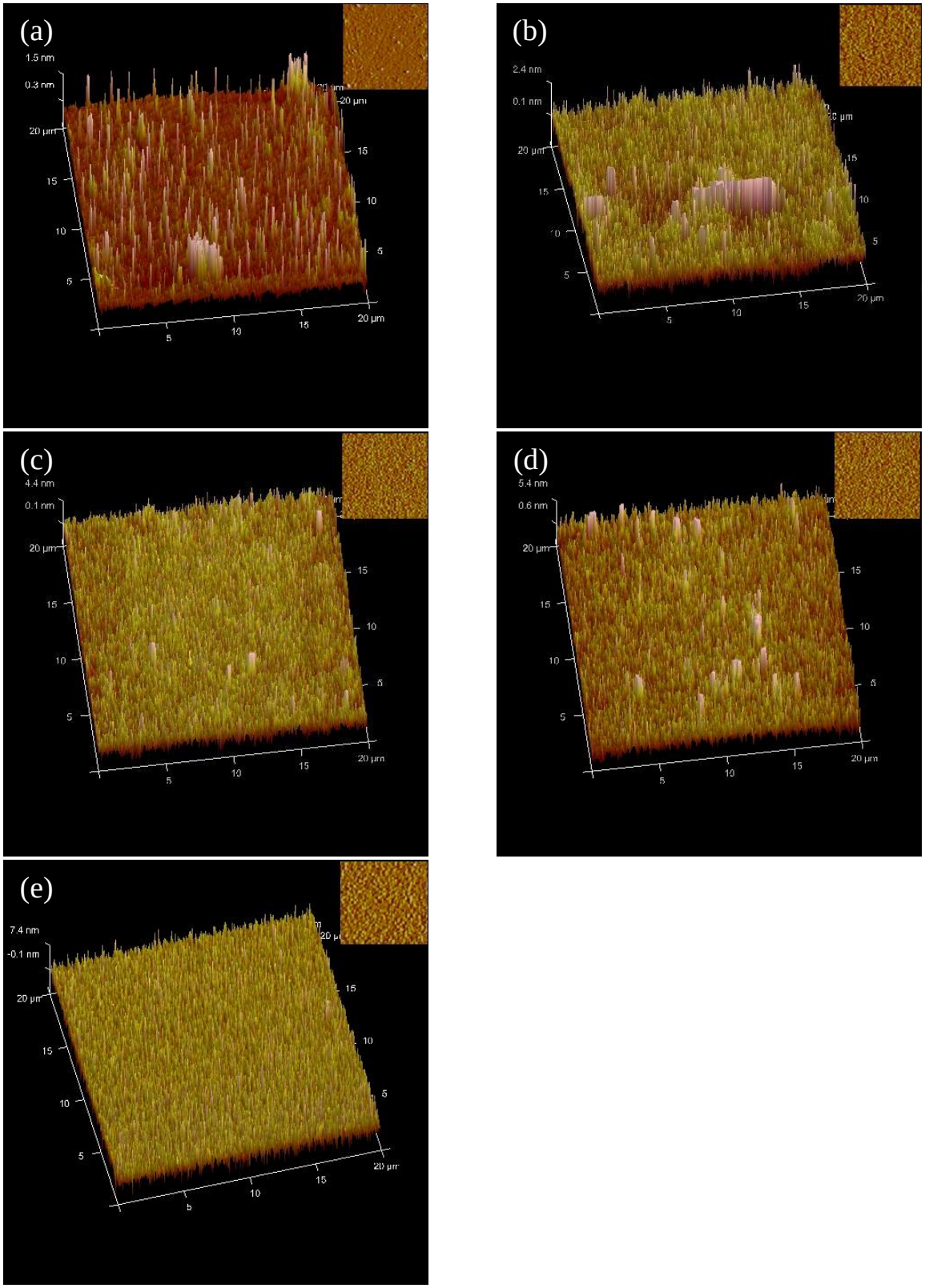

Figure 7-20: *AFM 3D micrographs and 2D images for H_2 annealed samples (a) before, and after annealing at (b) 700 °C, (c) 800 °C, (d) 900 °C and (e) 1000 °C.*

The decrease in the R_{pv} value might be caused by the SiO_2 layer formed during annealing at 1000 °C. The increase in the R_{rms} and R_a values is caused by the interfacial reaction of W and SiC, which results in the formation of tungsten silicides and carbide at the interface. The crystallization of the crystals to form bigger crystallites after annealing causes an increase in the R_{rms} and R_a values.

Table 7-6: AFM values for R_{rms}, R_a and R_{pv} before and after annealing in hydrogen for 1h.

Temperature (°C)	R_{rms} **(nm)**	R_a **(nm)**	R_{pv} **z-range (nm)**
As-deposited	0.4	0.2	28.0
700	0.8	0.5	31.8
800	1.4	0.9	53.8
900	1.6	1.0	70.9
1000	2.6	2.0	32.4

Figure 7-21 shows the change in the roughness of samples with increase in annealing temperature. R_{rms} values of the samples annealed at 700 °C, 800 °C, 900 and 1000 °C were higher than that of the as-deposited sample. This increase in roughness is associated with the change in the nature of the samples from small to larger granules with different sizes which is caused by the interfacial reaction of W and SiC to form silicides and carbides. The R_{rms} values obtained for different annealing temperatures indicate that the H_2 annealed samples had less rough (fine) surfaces compared to the vacuum annealed samples. The increase in roughness of the as-deposited sample from 0.44 nm to 1.60 nm after annealing at 900 °C, means the W grains are growing or becoming bigger.

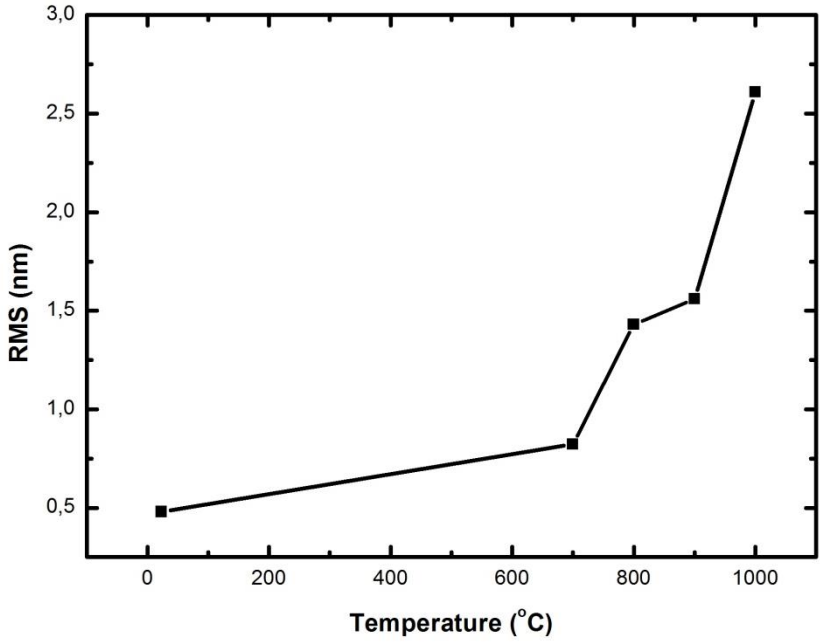

***Figure 7-21**: Root Mean Square (RMS) roughness of the hydrogen annealed samples against temperature.*

7.4 Argon (Ar) Ambient Annealing

7.4.1 Rutherford Backscattering Spectrometry

The W-SiC samples were also annealed in argon ambient at temperature ranging from 700 °C to 1000 °C and their RBS spectra are shown in figure 7-22 (a). The as-deposited sample is included for comparison.

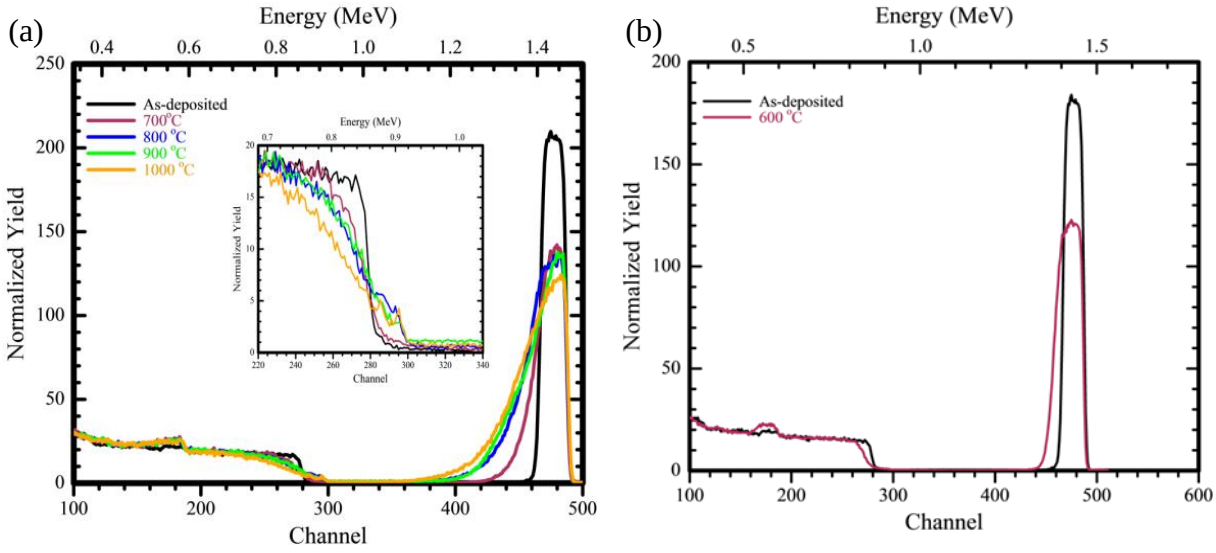

Figure 7-22: *(a) RBS spectra of the as-deposited and samples annealed in Ar gas for 1 hour at temperatures of 700 °C to 1000 ºC and the insert of magnified Si signal from channel numbers 220 to 340.(b) is the RBS of the sample annealed at 600 °C in Ar gas for 1h.*

The RBS spectrum of the sample annealed at 700 °C resulted in a reduction of the W peak height and a significant broadening at the back edge of the W signal towards lower energy channels. Concurrently, the top edge of the Si signal shifted to lower energy channels and the bottom edge shifted to higher channels. These indicate that inter-diffusion between W and SiC took place during annealing at this temperature. Oxygen peak at channel 180 observed on the as-deposited layer was found to be still present at the W-SiC reaction zone after annealing at 700 °C. It was also evident in figure 7-22(a) that the oxygen tails towards SiC after annealing at 700 °C. The best fit during simulation was obtained by fitting seven layers for sample annealed at 700 °C. Figure 7-23 (a) shows the atomic composition profiles at different depths of the 700 °C annealed sample.

Figure 7-22 (b) shows the sample annealed in Ar at 600 °C, this spectrum was included to show that interdiffusion between W and SiC which lead to reactions had already taken place

at this annealing temperature. This tells us that the initial reaction between W and SiC started at temperatures lower than 700 °C. Although not shown, the RBS spectrum for a sample annealed at 500 °C also indicated that interdiffusion and reactions also occurred at this temperature.

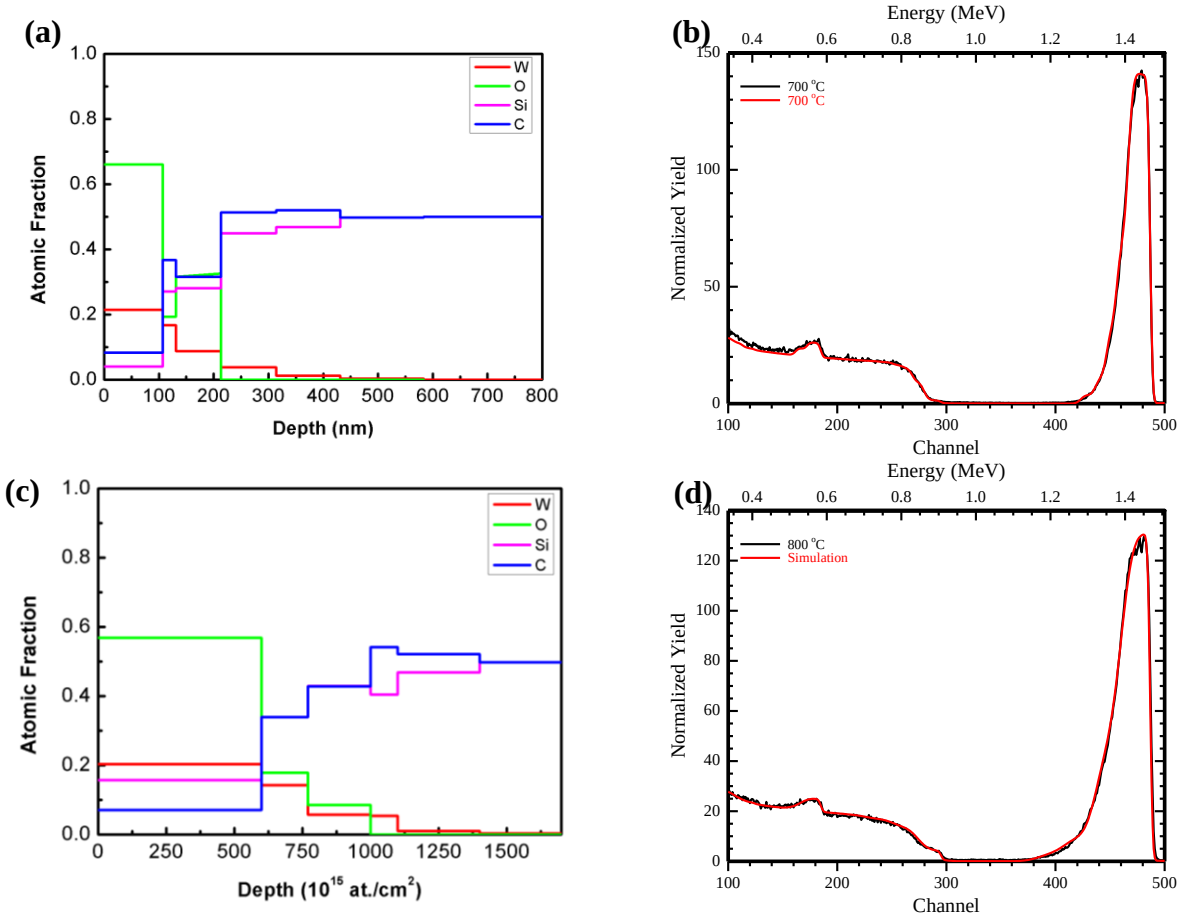

***Figure 7-23**: (a) Variation of elemental atomic fraction composition with layer thickness of the W-SiC sample annealed in Ar at 700 °C and (b) overlay of raw RBS data with the RUMP simulated spectrum. (c) Variation of elemental atomic fraction composition with layer thickness of the W-SiC sample annealed in Ar at 800 °C and (d) overlay of raw RBS data with the RUMP simulated spectrum.*

Only four layers were considered, since the other layers are mainly 96% SiC and W % C. The first layer was about 106.7 nm thick and its phase composed was 72.1 % of WO_3, 3.1 % of SiO_2, 8.2 % of W_5Si_3 and 16.6 % of W_2C. The second layer was 24.6 nm thick with the

following phase compositions: 29.0 % of SiO_2, 12.6 % of W_2C, 16.8 % of W_5Si_3, 4.2 % of WC, 32.6 % of C and 4.8 % of Si. The third layer was about 81.65 nm thick and had the following phase compositions: 47.4 % of SiO_2, 26.0 % of WC, 26.0 % of W_5Si_3 and 0.6 % of SiC. Layer four is 101.3 nm thick and its phase was composed of 11.0 % of WC, 4.5 % of W_5Si_3, 3.3 % of W_2C and 81.2 % SiC. It is clear from the results that a reaction between W and SiC started at a lower temperature than 700 °C.

Annealing at 800 ºC resulted in the further shift of the top of Si edge to lower energy channel numbers, with a step appearing at the bottom of the Si edge. A small reduction in the W peak height, accompanied by increase in the width of W peak occurred (W peak tailed to the lower energy channel numbers, further away from the 700 ºC peak). These indicated further reaction between W and SiC after annealing at this temperature. An increase in the RUMP simulated RZ width was observed. Figure 7-23 (c) illustrates the thickness of the reactants at 800 °C. From figure 7-23 it is evident that O did not disappear instead it took part in the reaction at the RZ. Seven layers were simulated for a good fit, but only 4 layers and phase composition are given, since the others layers have very little W. The first layer was 130.6 nm wide and composed of 45.5% of WO_3, 11.5 % of W_5Si_3, 34.1% of SiO_2, 3.5% of W_2C and 5.4% of C. The second layer was about 45 nm wide with 19.0% of W_5Si_3, 26.9% of SiO_2, 7.8 % of W_2C, 10.7% of C and 35.6% of SiC. The third layer was about 86.5 nm thick with the following compositions: 7.6% of W_5Si_3, 12.9 % of SiO_2, 1.9% of WC, 6.1% of C and 71.5% of SiC. The fourth layer was about 134.5 nm thick with the following phase compositions: 10.1% of WC, 8.9 % of C and 81.0% of SiC.

Annealing at 900 ºC resulted in a W peak being slightly broader when compared to the sample annealed at 800 °C. The width of the reaction zone after annealing at 900 °C was greater than that of the sample annealed at 800 °C. Only four layers with their phase

compositions are reported as the other layers were mainly Si and C. The first layer with thickness of 116.5 nm had the following phase compositions: WO_3 of 60.5%, 22.7% of SiO_2, 8.1% of W_5Si_3, 2.2% of W_2C and 6.5% of C. The second layer was 114.8 nm thick with 32.7% of SiO_2, 16.3% of W_5Si_3, 4.1 of W_2C, 31.9 % of C and 15.0% of SiC.

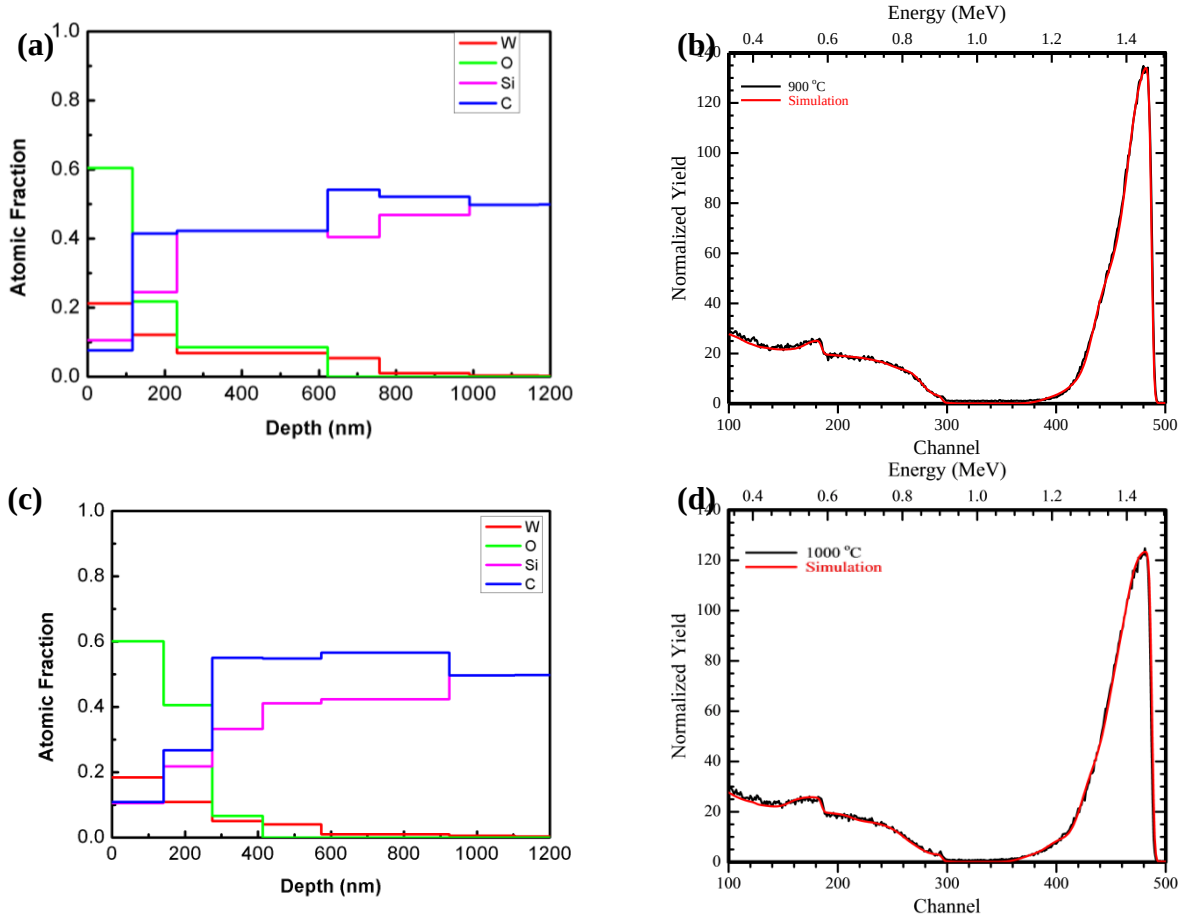

Figure 7-24: *(a) Variation of elemental atomic fraction composition with layer thickness of the W-SiC sample annealed in Ar at 900 °C and (b) overlay of raw RBS data with the RUMP simulated spectrum. (c) Variation of elemental atomic fraction composition with layer thickness of the W-SiC sample annealed in Ar at 1000 °C and (d) overlay of raw RBS data with the RUMP simulated spectrum.*

The third layer of about 390.8 nm had the following compositions: 12.7% of SiO_2, 9.2% of W_5Si_3, 2.3% of WC, 6.6% of C and 69.2% of SiC. The fourth layer which is 134.5 nm wide had the following compositions: 9.1% of WC, 9.9% of C and 81.0% of SiC. Increasing the annealing temperature to 1000 ºC resulted to a further shift in the Si top edge to lower energy

(channel numbers) and a reduction in the W peak height accompanied by broadening of the W signal towards lower energy (channel numbers). The reaction zone increased after annealing at 1000 °C. In all annealing temperatures, the oxygen peak was observed to be tailing towards the lower energy channels. This indicated that oxygen was taking part in the W-SiC RZ as one of the reacting agents. Annealing at 1000 ºC resulted in further shift of W peak to lower energy channel number. The peak height of W also reduces when compared to the 900 °C spectrum, where the Si edge and W peak height did not have a noticeable change. About 7 layers were simulated but only 4 are reported, because the other layers were composed of about 96.0% of SiC. The first layer of about 140.9 nm thick had the following phase composition: 60.0% of WO_3, 22.6% of SiO_2, 4.6% of W_5Si_3, 1.1% of W_2C, 8.9 of C and 2.8 of SiC. The second layer was 133.4 nm thick and was composed of the following phases: 60% of SiO_2, 5% of W_5Si_3, 16.8% of W_2C, 18.3% of C and 2.4% of SiC. The third layer was 138.4 nm thick and had the following phase compositions: 9.9% of SiO_2, 6.8% of W_5Si_3, 3.7% of WC, 24.7% of C and 54.9% of SiC. The forth layer was 160.5 nm thick with the following phase compositions: 7.2% of WC, 10.6% of C and 82.2% of SiC.

The composition of the RZ from the RUMP simulations after annealing from 700 °C to 1000 °C consisted of W, Si, C and O. The possible compounds formed were: tungsten silicide, tungsten carbide, tungsten oxide and silicon oxide. All the compounds remained present with varying fractions after each annealing temperature. The surface roughness did not have an impact on our RBS results. Since Ar is an inert gas, it does not react with oxygen to reduce the quantity present. The reaction between the W and SiC reduces the W concentration, making the amount of WO_3 in the first layer to be dominant. The ratio of oxygen to tungsten in WO_3 in high thus an increase in the oxygen is observed.

7.4.2 Grazing Incident X-ray Diffraction

The GIXRD patterns of the W thin film deposited on 6H-SiC substrate before and after annealing are depicted in figure 7-25. The samples annealed at 700 °C had additional two broad W peaks positioned of 43.5º, 57.1º and 81.2º attributed to (211), (200) and (222) reflection planes, respectively. They were not observed on the as-deposited because of the nano-particle size nature of the material. Nano-particles cause peak broadening; in some cases the peak broadening was significant, causing no peak detection. A reaction between W and SiC took place after annealing at 700 °C.

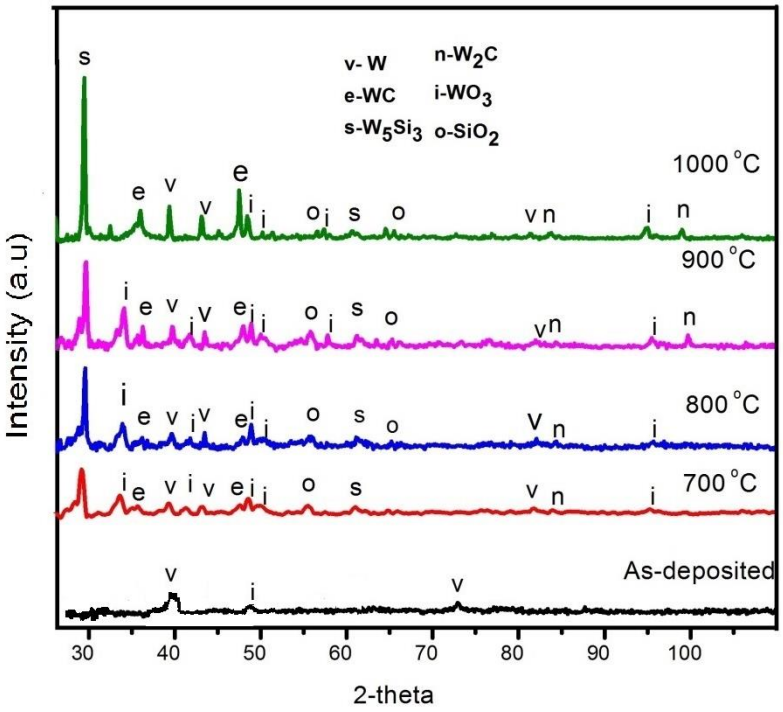

Figure 7-25: *X-ray diffraction patterns for the W-SiC sample before and after annealing in argon ambient at 700 ºC, 800 ºC, 900 °C and 1000 ºC for 1h.*

These results correlate with the RBS results which showed that a reaction had occurred after annealing at 700 °C. The initial silicide formed was W_5Si_3 with (310) and (512) planes at 29.5º and 61.6º respectively. The carbide formed was WC corresponding to (100) and (101) planes at 35.6º and 48.4º, respectively. The appearance of WO_3 with (112) plane at 34.3º,

(111) plane at 41.9º, ($\bar{1}$40) plane at 49.0º, (002) plane at 51.2º and (510) plane at 95.9º indicated the presence of an oxide in the sample annealed at 700 °C. The appearance of the SiO_2 peak at 2θ position of 56.9º with the orientation of (535) located at the W and SiC interface was observed after annealing at 700 °C. The formation of SiO_2 could be due to a reaction between WO_3 and SiC. As reported from our RUMP simulations of RBS results, oxygen in the form of oxide (tungsten oxide) was found at the RZ layer that formed between W and SiC. The W_2C carbide with orientation of (103) plane at 84.39º 2θ position was also observed. Equation (7-10) and (7-11) show the resulting products after reaction:

$$9\ W + 3\ SiC \rightarrow W_5Si_3 + 3WC \qquad (7\text{-}10)$$

$$2WO_3 + 3\ SiC \rightarrow 3\ SiO_2 + W_2C + 2C \qquad (7\text{-}11)$$

Equation (7-10) and (7-11) occurred simultaneously at temperatures ranging from 700 °C to 1000 °C. Table 7-7 confirms that the reactions represented by equation (7-10) and (7-11) are possible.

Table 7-7: ΔG for Ar samples at RT to 1000 °C for the reaction determining the stability of the reaction products.

			Δ*G* (kJ/mol)		
Reaction	**RT**	**700 °C**	**800 °C**	**900 °C**	**1000 °C**
$9\ W + 3\ SiC \rightarrow W_5Si_3 + 3WC$	-45.6	-74.0	-78.2	-82.4	-86.6
$2WO_3+3SiC \rightarrow 3SiO_2 + W_2C+ 2C$	-850.5	-846.7	-858.7	-847.1	-847.6
$2WO_3+2SiC \rightarrow WSi_2+W_2C+CO_2+2O_2$	1556.8	1192.6	1141.9	1091.5	1041.2

The GIXRD patterns for the sample annealed at 800 ºC did not show much of a difference as compared to the 700 ºC annealed patterns. W_2C (203) at 97.9º 2θ position together with a new SiO_2 (404) peak at 2θ position 65.4º were observed after annealing at 900 °C and 1000 ºC. An increase in the intensity of the peaks upon annealing from 700 ºC to 1000 ºC suggests a change in the structure: samples are becoming more crystalline from their polycrystalline nature and change in crystal size.

Table 7-8 shows the calculated average crystal sizes of the phases obtained from the XRD results using Scherrer's equation. The as-deposited sample had W average grain size of about 13.1 nm. Annealing the sample at 700 °C led to a decrease in the W average crystal size to 7.4 nm.

Table 7-8: Average crystal sizes of the silicides, oxides and carbides calculated from the Ar annealed sample XRD patterns.

Temp (°C)	**W (nm)**	**W_5Si_3 (nm)**	**WC (nm)**	**W_2C (nm)**	**WO_3 (nm)**	**SiO_2 (nm)**
as-deposited	13.1	0	0	-	4.1	-
700	7.4	8.4	29.4	1.9	7.1	4.4
800	16.2	17.6	12.5	12.8	10.3	10.6
900	16.6	20.0	17.8	16.5	12.3	12.9
1000	17.3	21.0	18.6	10.8	12.5	13.7

This decrease in the W average crystal size was caused by the parasitic growth of the newly formed phases. After annealing at 800 °C, an increase in the W average crystal size to 16.2 nm was observed. The average crystal size of W was observed to increase to 16.6 nm and 17.3 nm after annealing at 900 °C and 1000 °C, respectively. The WC phase average crystal at 700 °C was 29.4 nm, and at 800 °C it decreased to 12.5 nm. The average crystal size for the W_2C phase increased from 1.7 nm at 700 °C to 16.5 nm at 900 °C. A decrease in the

average crystal size at 1000 °C to 10.8 nm was observed. The parasitic growth due to the presence of different phases affected the crystal growth of the WC phase at 800 °C and W_2C phase at 1000 °C. The samples annealed at 900 °C and 1000 °C results in the increase of the WC average grain size to 17.8 nm and 18.6 nm, respectively. The average crystal sizes of W_5Si_3, W_2C, WO_3 and SiO_2 increased from 8.4 nm, 1.9 nm, 7.1 nm and 4.4 nm at 700 °C to 21.0 nm, 12.5 nm and 13.7 nm at 1000 °C, respectively.

7.4.3 Scanning Electron Microscopy

In figure 7-26, the SEM micrographs of W thin film deposited on 6H-SiC before and after annealing at 700 ºC, 800 ºC, 900 ºC and 1000 ºC for 1 hour in Ar are depicted. The as-deposited sample shows a fairly flat surface of the W thin film. Annealing at 700 ºC and 800 ºC led to a major change in the surface morphology of the samples. The sample's surface became crystalline at 700 ºC and the crystals were of different sizes and shapes and were randomly orientated. At 800 ºC, rod-like crystals of different sizes were observed with no preferred orientation. At both temperatures, some of the crystals were protruding from the surface. The difference in surface morphology indicated that substantial reactions along with atomic migration in the W film surface took place during annealing.

Smith and Thompson [27], investigated the effect of annealing in N_2 and Ar ambient of W deposited on Si at 1100 °C. They co-sputtered W and Si on a Si substrate and observed that annealing in argon resulted in the formation of large grains while in N_2 a smooth surface was observed. The change in the surface structure of W deposited on Si after annealing in which produced a highly rough surface was ascribed to the reaction between W and Si. They further stated that stress assisted growth was taking place leading to large columnar grains forming.

The delamination in the stress assisted growth regions allowed new regions of unstressed and unreacted silicide to regrow.

Annealing at 900 ºC and 1000 ºC resulted in crystals growing (stacking) on top of each other with pores observed between the crystals. Inside the pores, small crystallites were observed to have formed. At 1000 °C, small crystals in between the big crystals were larger as compared to the 900 °C annealed sample. The big crystals at 1000 °C when compared to 900 °C became smaller. These results are also in agreement with the XRD results where the changes in the crystal nature of the annealed samples were indicated by the increase in the intensity of diffraction peaks. The presence of the small grains formed in between the larger crystals observed in figure 7-26, might affected the calculated crystal size of the phases formed, as seen in Table 7-8. If the area analysed has the mixture of small and large crystals of different and/or same phases, the phase with large crystals will show large intensity and the small crystallites will have small intensity.

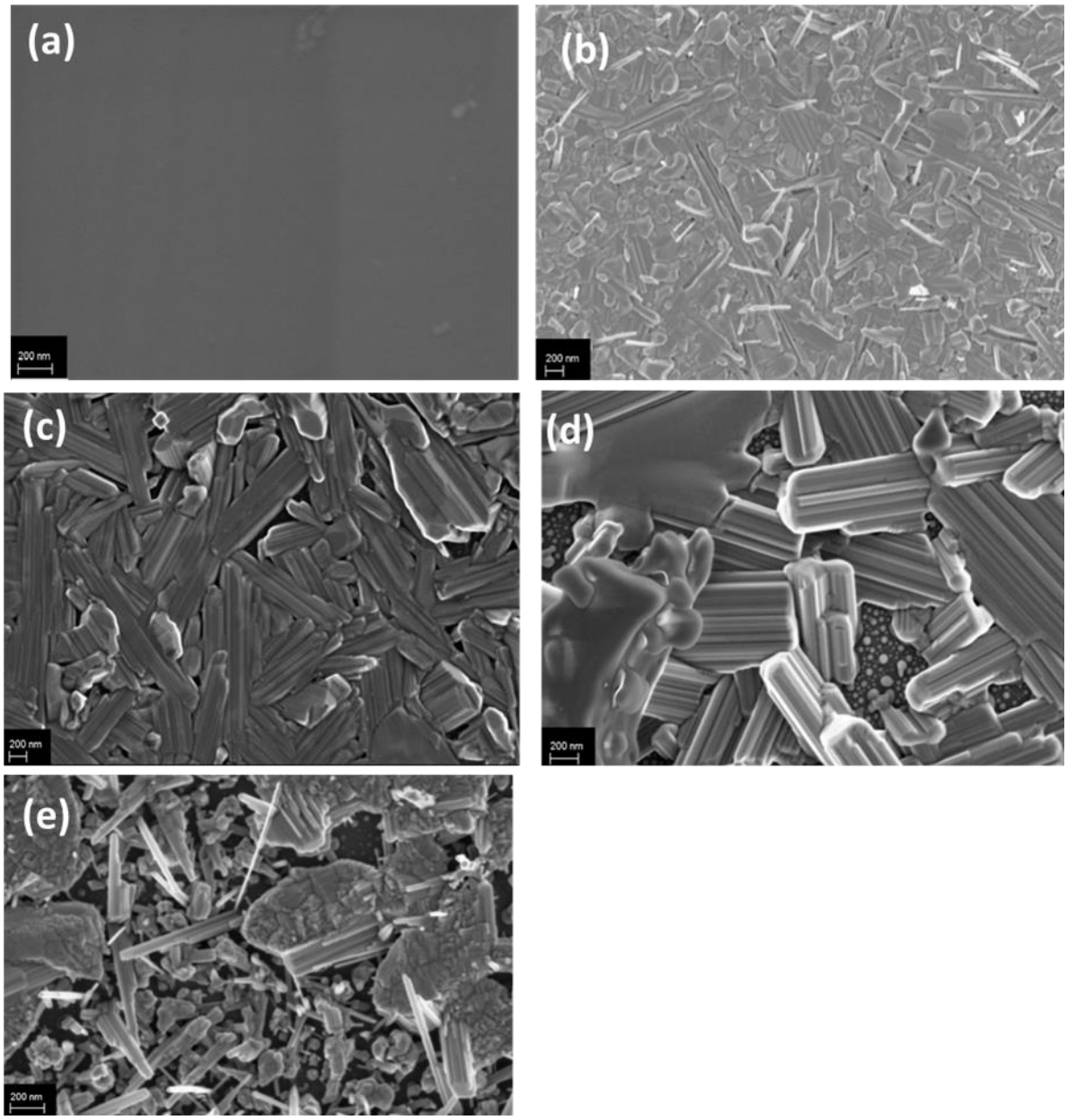

Figure 7-26: *SEM micrographs of (a) as-deposited W-SiC and Ar-annealed sample at (b) 700 ºC, (c) 800 ºC, (d) 900 ºC and 1000 ºC for 1 hour.*

The phases with both large and small crystals will be averaged, causing either an increase or decrease in the crystal size, depending on the number of the large or small crystals present. Annealing at high temperatures resulted in the formation of large crystals in the form of distinct islands (pores between the crystals). The formation of large crystals and spaces between crystals on the W-SiC surfaces was also observed on samples annealed in vacuum [28]. These cavities are formed during the parasitic growth of crystallites and crystal surfaces

at elevated temperatures. Parasitic growth follows Wulf's law [29], which states that crystal surfaces with high surface energies feed the surfaces with lower surface energies, resulting in the former growing faster than the latter, thereby exposing larger areas of crystal surfaces with lower surface energies. This leads to a minimization of the Gibbs free energy of the system.

7.4. 4 Atomic Force Microscopy

Figure 7-27 shows the AFM 3D micrographs (the inserts are their respective 2D images) of samples annealed in Ar atmosphere compared with the as-deposited sample. The AFM 2D image for 700 °C has large granules of different sizes compared to the as-deposited. The 3D image shows pronounced islands, hillocks and valleys in the 700 °C annealed sample. The samples annealed at 800 °C, 900 °C and 1000 °C show large crystals with irregular shape and different sizes in form of islands. This fast growth rate is due to the high reaction between W and SiC and the rearrangement of the atoms in the sample (surface diffusion). The 3D micrograph indicates that the hillocks, valleys and island evolved with annealing temperature. At 1000 °C, the number of large crystal decreases leading to a drop in the R_{rms}.

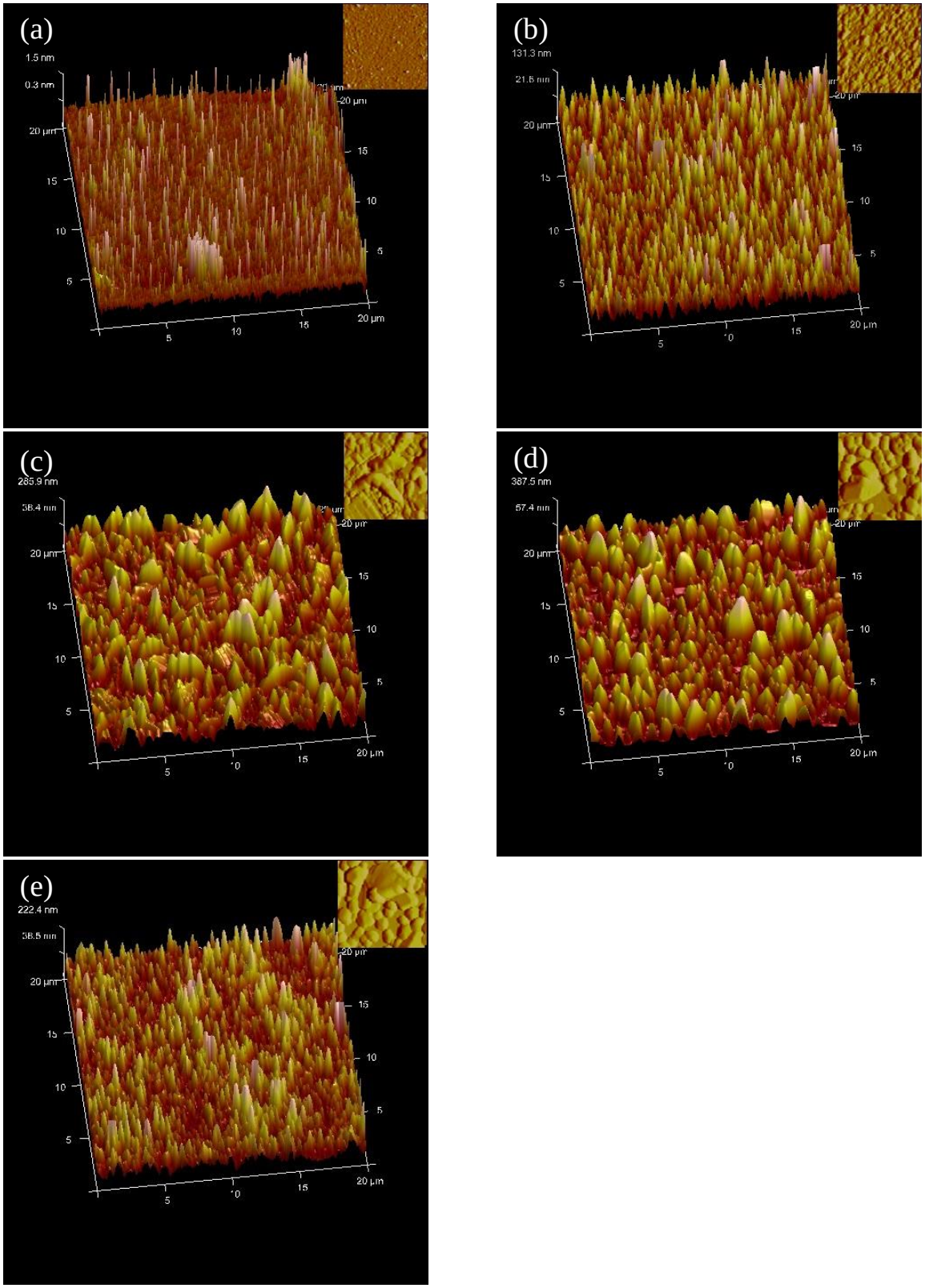

Figure 7-27*: AFM 3D micrographs and the 2D image inclusion (a) before and after annealing in or Ar annealed samples at (a) RT, (b) 700 °C, (c) 800 °C, (d) 900 °C and (e) 1000 °C.*

Table 7-9 shows the calculated values of R_{rms}, R_a and R_{pv} as-deposited and annealed samples. The decrease in R_{pv} after annealing at 1000 °C from 645 (at 900 °C) to 467 nm was caused by the change in the nature of the sample surface. As it was observed from the SEM images, a large number of small crystals appeared after annealing at 1000 °C and this might have been the cause for the reduction in the crystal size for the 1000 °C annealed samples. From figure 7-26 (b to e) the 2D image shows a mixture of large and small crystals in a form of stand-alone islands. The AFM 2D image shows similar information to the SEM image. The difference in the two types of image is caused by the difference in which the image is created (collected and generated) during the different type of analyses.

Table 7-9: Values for R_{rms},R_a and R_{pv} before and after annealing the samples in Ar for 1h.

Temperature (°C)	R_{rms} **(nm)**	R_a **(nm)**	R_{pv} **z-range (nm)**
As-deposited	0.4	0.2	28.0
700	31.6	24.4	440.0
800	70.1	54.4	472.0
900	102	82.9	645.0
1000	50.0	37.9	467.0

The R_{rms} and R_a values for the samples annealed in argon are larger than the values obtained from the vacuum and hydrogen annealed samples. This is due to the large crystals which form upon annealing in argon as seen from the SEM images. Figure 7-28 shows a plot of *Rrms* roughness of the Ar annealed samples.

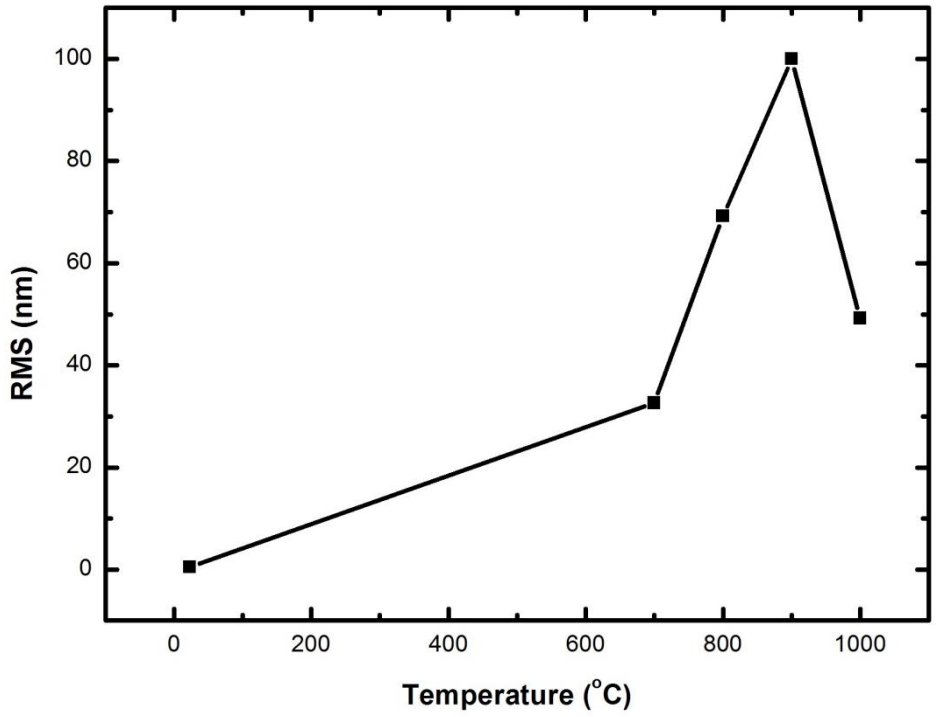

Figure 7-28: *Root Mean Square (RMS) of the Ar annealed samples against temperature.*

7.5 Discussion

In this study W was sputter deposited on 6H-SiC. The deposited samples were annealed in vacuum, hydrogen and argon ambient at temperatures ranging from 700 °C to 1000 °C for 1h. According to the W-Si-C ternary phase diagram obtained from Seng [10] a reaction between W and SiC can occur between 23 °C to 700 °C depending on the deposition of method used for deposition. The phases expected to form are WSi_2 and WC based on the phase diagram. WSi_2 is stable with WC and SiC within temperatures range of 23 °C - 700 °C. At the temperature range of 700 °C - 1867 °C, WC is stable with SiC and W_5Si_3. W_5Si_3 becomes stable with SiC and W_2C at the temperatures above 1867 °C.

In this study the sample annealed in vacuum at 700 °C indicated the formation of CW_3 and WC in the RZ. The surface structure contained small W crystallites of different sizes with

tungsten oxide nanowires embedded on the W surface. The crystals on the surface did not show any form of separation/segregation, the surface structure was still intact. The sample annealed at 800 °C indicated surface segregation/separation on some parts of the samples, while other parts remain intact. The sample composition remained the same for the 700 °C annealed sample, with fewer tungsten oxide nanowires. The surface roughness of the sample annealed at 800 °C was 7.7 nm, while the surface roughness of the sample annealed at 700 °C was 2.3 nm. W_2C and WSi_2 were observed to form at 900 °C, causing the surface roughness (14.9 nm) to double when compared to that of 800 °C annealed sample. The entire surface was composed of large and small islands. The 1000 °C annealed sample had large spaces in between the crystals, with small crystallites in the spaces. The surface roughness of about 9.5 nm was obtained with WSi_2, WC and W_2C as the phases present.

Annealing the W-SiC samples in H_2 at 700 °C results in the reaction between W and SiC forming W_5Si_3 and WC at the RZ. The surface was smooth (about 0.83 nm surface roughness) and composed of small crystallites/granules with no visible grain boundaries. An increase in the reaction zone at 800 °C results in the surface roughness of 1.44 nm. The surface structure showed grain boundaries. W_2C and WSi_2 were formed with WC and W_5Si_3 still present. Further increase in reaction temperature to 900 °C, resulted in the increase of the RZ and the surface roughening (1.60 nm). Yet, the surface structure at 900 °C still looked like the one observed at 800 °C.

Sample annealed in Ar at 700 °C formed crystals and the following phases were observed; W_5Si_3, WC, W_2C and SiO_2. The surface was fully covered with crystal and had grain boundaries. The W_5Si_3, WC, W_2C and SiO_2 phases were present in all the annealing temperature. No change in the phases was observed after annealing from 700 °C to 1000 °C.

The surface structure changed, that is at 800 °C the crystals were seen to be big, with spaces in between them. The samples annealed at 900 °C and 1000 °C had a mixture of small and large crystals. The small crystals were formed in between the large crystals.

The W-SiC samples annealed in vacuum [28], hydrogen [25] and argon [26] ambient from 700 °C to 1000 °C for 1h indicated differences in surface structure and phases formed. The Ar and H_2 annealed samples showed that the reaction between W and SiC to form silicide occurred at 700 °C. The vacuum annealing results only indicated the formation of silicide at 900 °C. It was evident that the formation of silicide in vacuum annealed samples starts at higher temperatures than the Ar and H_2 annealed samples. Annealing in vacuum resulted in the reduction of the oxygen from the W thin film with increase in annealing temperature. The samples annealed in H_2 led to the removal of the oxygen present in the as-deposited W film. The removal of oxygen in the H_2 ambient is because H_2 is a reactive gas (removes oxygen by reacting with it). Annealing in argon did not reduce the oxygen content present in the samples. Instead, the oxygen took part in the reaction between W and SiC. Ar is an inert gas, so it does not react with the oxygen present on as-deposited samples.

In hydrogen annealing, H_2 reacts with the oxygen on the surface to form water vapour. H_2 further enter W surface via the grain boundaries, reacts with oxygen inside the W-WO_3 layer then escape via grain boundary. The tungsten dioxide in vacuum annealed sample precipitates and diffuses via the grain boundary, reducing the oxygen in the W-SiC sample. Annealing in argon prevents the oxygen removal and diffusion of tungsten oxide towards the surface. During annealing at 700 °C in Ar ambient, WO_3 dissociates to form W and O, SiC dissociates to form Si and C. Inter-diffusion between all the atoms takes place leading to Si reacting with O. The argon influences the diffusion of oxygen towards the SiC, allowing it to react with Si.

Since Ar is heavier than hydrogen and is inert, it causes Oxygen to go further inside. The presence of oxygen in the argon annealed samples acted as a catalyst to speed up the reaction between W-WO_3 and SiC. Annealing in vacuum reduced the tungsten oxide present and annealing in hydrogen removed the oxygen present (as seen in RBS, XRD and SEM results). Hence the reactions in H_2 annealed samples and vacuum annealed sample were slower as compared to the argon annealed samples.

The reaction zone thicknesses after annealing in vacuum, hydrogen and argon were different. The samples annealed in Ar had a greater reaction zone thickness than the vacuum and H_2 annealed samples. Annealing in different atmospheres results in the RZ thickness order as shown in figure 7-29: Ar samples > vacuum samples > H_2 samples. More reaction products are formed in the argon annealed samples when compared to the vacuum and H_2 annealed samples. Thus, the annealing atmospheres also played a role in the thickness of the reaction zone. Annealing in different environments was found to produce different surface morphologies.

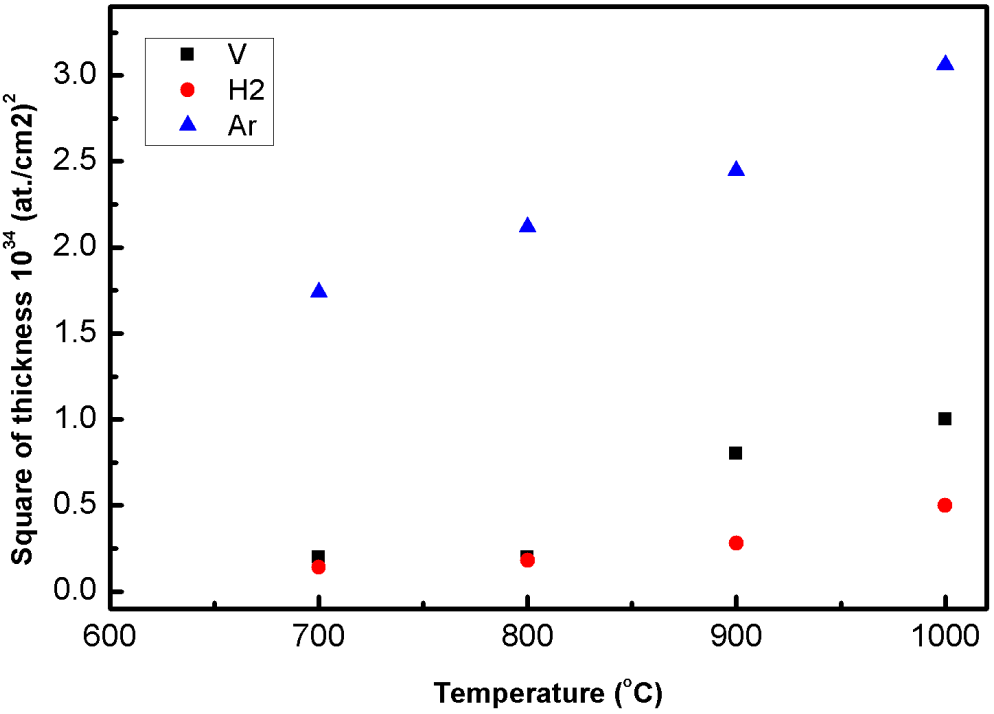

Figure 7-29: *Plot of square of the total reaction zone thickness versus annealing temperature.*

The samples annealed in vacuum contained tungsten oxide nanowires, while the formation of small W grains was observed in the hydrogen annealed samples. Large crystals were observed on the surface of the argon annealed samples, clearly indicating the surface morphology dependence on annealing atmosphere. Annealing at 900 ºC and 1000 ºC indicated that the material crystallizes at a fast rate in Ar atmosphere with a formation of large crystals with spaces in between them. While the vacuum annealed sample at 1000 °C led to the formation of crystals with openings (holes) in between them. An increase in the W grain size was observed on the surface of H_2 annealed samples.

The crystal size of the Ar annealed [26] (from 700 ºC to 1000 ºC) W-SiC samples' surface were larger and randomly orientated compared to the vacuum annealed [28] and hydrogen annealed [25]. Crystal growth in the form of grains was observed after annealing in hydrogen.

Annealing in vacuum resulted in the formation of grains which changed with increase in temperature to form crystals in the form of distinct islands (spaces in between the flat crystals). The presence of oxygen might have influenced the formation of the large crystals (enhances crystallization) in Ar annealed samples. The formation of large crystals and spaces between crystals on the W-SiC surfaces was also observed on W-SiC samples containing oxygen annealed in vacuum and Ar. In the vacuum annealed samples, precipitation might also play a role in reducing the number of impurities causing the formation of crystals at 1000 °C. The Ar annealed samples had high surface roughness than the vacuum and H_2 annealed samples.

The different surface morphologies between the hydrogen and vacuum annealed surfaces were previously explained in terms of the reducing effect (i.e. removal of oxygen) of the hydrogen [25]. The different morphology of the Ar annealed samples can be explained in terms of a crystal growth model [26]. In this model, crystals grow due to minimization of the surface energies. Crystals with high surface energies merge with crystals with low surface energies so as to minimize their surface energies.

When annealing samples, some gas atoms present in the annealing system can be physisorbed or chemisorbed on the crystallite surfaces and in the reaction zone via cavities/opening in the layer during annealing. Hydrogen, a reacting gas, is commonly chemisorbed and physisorbed on W surfaces [30][31][32]. According to the step-flow mechanism [33] of crystal growth, impurity atoms on the growth surfaces of crystallites inhibit the growth process of the crystallites. Based on this model, one can expect the hydrogen annealed samples to have smaller crystallites than the vacuum annealed samples – as was observed [25], [28]. Hydrogen penetrates the W thin film, reacts with some of the oxygen and escape via the grain

boundaries. Some of the hydrogen gas sticks on the tungsten surface (due to the week van de Waal forces) and between the W film cavities [31][34]. This H_2 gas that sticks on the W acts as impurity which slows down the W crystal growth.

In vacuum annealing, trace gases are still present and can stick to the surfaces of the crystallites. During annealing the small particles present in the chamber after evacuation can be chemisorbed and some physisorbed. The impurities in vacuum annealed samples are way less than in the hydrogen annealed samples as the trace gases in vacuum are less. Thus, the growth rate in vacuum annealing sample is greater than the H_2 annealed sample. Because Ar is a noble gas with no chemisorption and with little to no physisorption in W surfaces, the Ar annealed samples should have the largest crystallites – also observed in this study.

Since the RBS, XRD, SEM and AFM do not show the phase location and diffusion path in the reaction zone, RBS spectra results and RUMP simulation in combination with XRD, are used to speculate the phase arrangements/diffusion path of the samples annealed in vacuum, H_2 and Ar are suggested to follow the order below:

For vacuum annealed samples:

WO_2-W/CW_3/WC/SiC at 700 °C and 800 °C (7-11)

WO_2-W/W_2C/WC/WSi_2/SiC at 900 °C and 1000°C (7-12)

The diffusion path observed in the vacuum annealed samples agrees with Son's results [9].

Hydrogen annealed samples:

$W\text{-}WC/W_5Si_3/WC/SiC$ at 700 °C (7-13)

$W/\ W_5Si_3\ /\ W_2C/\ WC/WSi_2/SiC$ at 800 °C to 900 °C (7-14)

$SiO_2/W/W_5Si_3/W_2C/WC/SiC$ at 1000 °C (7-15)

Annealing in H_2 indicated that C diffuses faster than Si, leading to the diffusion path in equation (7-13). At high temperature, Si catches up with the C diffusion resulting to the diffusion path observed (7-15). Similar diffusion path was also reported by Goesman and Schmid-Fetzer [13] after annealing of W-SiC sample in vacuum at 1200 °C.

Argon annealed samples:

$WO_3\text{-}W/SiO_2/\ W_5Si_3/W_2C/WC/SiC$ 700°C to 1000 °C (7-16)

The diffusion path order in equation 7-16 follows the speculation that tungsten rich materials are expected to form closer to the tungsten. While carbon- or silicon-rich materials will form closer to the SiC substrate. A phase will only be tungsten rich if it is located nearest to the tungsten film. Changyou *et al.* [35] reported on the structural arrangement of the RZ for W-SiC to be following this order: $W/W_2C/W_5Si_3/WC/SiC$ after annealing in vacuum, while Toplišek [36] report had the following order for W-SiC vacuum annealed samples: $W/W_5Si_3/W_3Si/W_2C/SiC$. The structural arrangement observed by the latter authors is in agreement with the ones represented in (7-14), (7-15) and (7-16).

From different experimental results [9][12][13], heat of formation and Elligham diagram [10], WSi_2 is expected to be the first silicide before the formation of W_5Si_3. The presence of

W_5Si_3 silicide does not prevent the formation of WSi_2 as seen in H_2 annealed samples, although the temperature of formation is lowered to 800 °C when compared to the vacuum annealed samples at 900 °C.

The formation of WSi_2 did not take place for the Ar annealed samples. Instead Si reacted with O to form SiO_2. The formation of SiO_2 might have prevented the formation of WSi_2. Annealing in Ar at 700 °C forms WC, W_2C, W_5Si_3 and SiO_2 phases, and the phases did not change with increase in temperature. The assumption that SiO_2 becomes stable with SiC at 700 °C to 1000 °C was made. This assumption was based on the fact that no other phases are formed after annealing at 700 °C. The formation of SiO_2 at 700 °C to 1000 °C was only observed in Ar because the oxygen content does not reduce; there is enough oxygen to react with Si. The SiO_2 quantity is high enough for the GIXRD equipment to detect it. For the samples annealed in H_2, the formations of SiO_2 occurred at 1000 °C.

Figure 7-30 represents a W-Si-C ternary diagram adapted from Seng [10], with the inclusion of oxygen. This figure summarises the results obtained in this study. The vacuum and hydrogen annealed samples are in line with the W-Si-C ternary diagram adapted from Seng. But annealing in argon introduces oxygen as one of the reactants in the RZ, which resulted in the diagram below with W-Si-C-O. The diagram shows O product formed in the reaction that takes place in argon annealed samples. The tie –lines indicate the diffusion path and stability of the reactants and products. The black bold tie-lines mean the phases are observed for all annealing atmospheres. The maroon bold tie-line means that W_5Si_3 is not present in vacuum annealing. Looking at the (W-Si-C) diagram below the silicides are stable with SiC. Also, WSi_2 is stable with WC and W_5Si_3 is stable with W_2C. The black dotted tie-line between WC and WSi_2 means that WSi_2 is not necessarily stable and present at all the annealing

temperatures (between 700 °C and 1000 °C), as it was shown from the results that WSi_2 is formed at 800 °C (H_2) and 900 °C (vacuum) and SiO_2 is formed when annealing in Ar. Introducing O prevents the formation of WSi_2, and favours the formation of SiO_2. The SiO_2 will (at 700 °C to 1000 °C) become stable with SiC and W_2C (just like WSi_2). The W_5Si_3 was observed to form in Ar and H_2 ambient but was not observed in vacuum annealed sample. In H_2 and Ar annealed samples there were more W atoms available and therefore W-rich silicides appear as initial phases as opposed to Si-rich phases. This is due to favourable kinetics since, the number of W atoms available at the interface to react with Si to form silicides is high. For the H_2 annealed samples, oxygen from WO_3 is removed, which leaves more W atoms. For the samples annealed in Ar ambient, the oxygen from tungsten oxide reacts with Si, providing more W atoms in the system.

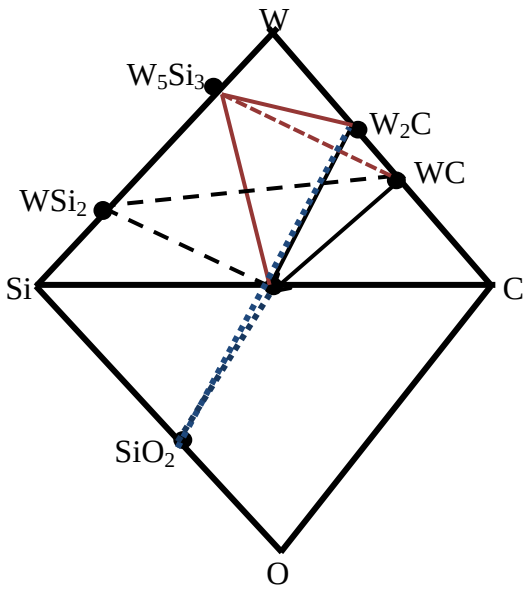

Figure 7-30: *Phase Diagram representing W-Si-C-O system between RT ≤ T ≤ 1000°C. It shows the phases formed between W, WO_3-SiC when the annealed in Ar, H_2 and vacuum from 700 to 1000 °C.*

In vacuum, the tungsten oxide precipitates and moves to the surface. Different annealing conditions, material available for reaction and favourable kinetics or thermodynamically favoured conditions determine which phases will be preferred. W is seen to diffuse deeper into the SiC for the Ar annealed samples than the vacuum and H_2 annealed samples. This shows that annealing in Ar and the presence of oxygen enhances the diffusion of W deeper in the SiC. C is observed to move/diffuse faster than Si when annealed in different atmosphere at different annealing temperature. After C reaches equilibrium, Si begins to diffuse. Reactions in Ar annealed samples start at temperatures lower than 700 °C, in H_2 it starts at 700 °C and in vacuum it visible at 850 °C (although it starts at 700 °C). Annealing in a gaseous atmosphere lowers the reaction temperature. The initial phases observed in H_2 are W_5Si_3 and WC, in Ar are W_5Si_3, WC, W_2C, SiO_2 and in vacuum WC and WSi_2. The surface structure of the samples annealed at 700 °C in vacuum is flat and is composed of small granules covering the whole surface. For the samples annealed at temperatures ≤ 800 °C, the surface structure contains openings. The surface structure for the sample annealed in H_2 from 700 ° to 1000 °C was fairly smooth and flat. At temperatures ≤ 800 °C, the surface contains grain boundaries. The argon annealed samples have large surface crystal with opening for 700 °C to 1000 °C annealed temperatures. This means at 800 °C to 1000 °C temperatures the W-SiC surface structure becomes compromised and cannot be used for nuclear application at temperatures above 700 °C.

References

[1] L. R. Doolittle, “Algorithms for the rapid simulation of Rutherford backscattering spectra,” *Nucl. Instruments Methods Phys. Res. Sect. B Beam Interact. with Mater. Atoms*, vol. 9, no. 3, pp. 344–351, 1985.

[2] “Tungsten: reactions of elements.” [Online]. Available: https://www.webelements.com/tungsten/chemistry.html. [Accessed: 05-May-2017].

[3] H.-J. Zhai, B. Kiran, L.-F. Cui, X. Li, D. a Dixon, and L.-S. Wang, “Electronic structure and chemical bonding in MO(n)- and MO(n) clusters (M = Mo, W; n = 3-5): a photoelectron spectroscopy and ab initio study.,” *J. Am. Chem. Soc.*, vol. 126, no. 49, pp. 16134–41, 2004.

[4] J. Kaduk, “Poly Crystallography, Inc.,” 2017. [Online]. Available: http://www.polycrystallography.com/index.html. [Accessed: 24-Jan-2017].

[5] “Particle size and shape | Rigaku - X-ray analytical instrumentation.” [Online]. Available: http://www.rigaku.com/en/applications/particle_size_shape. [Accessed: 24-Jan-2017].

[6] I. Petrov, P. B. Barna, L. Hultman, and J. E. Greene, “Microstructural evolution during film growth,” *J. Vac. Sci. Technol. A*, vol. 21, p. S117, 2003.

[7] J. A. Thornton, “High rate thick film growth,” *Annu. Rev. Mater. Sci.*, vol. 7, p. 239, 1977.

[8] K. L. Westra and D. J. Thomson, “The microstructure of thin films observed using atomic force microscopy,” *Thin Solid Films*, vol. 257, no. 1, pp. 15–21, 1995.

[9] K. M. Geib, C. Wilson, R. G. Long, and C. W. Wilmsen, “Reaction between SiC and W , Mo , and Ta at elevated temperatures,” *J. Appl. Phys.*, vol. 68, no. 6, pp. 2796–2800, 1990.

[10] W. F. Seng and P. A. Barnes, “Calculations of tungsten silicide and carbide formation on SiC using the Gibbs free energy,” *Mater. Sci. Eng. B*, vol. 72, pp. 13–18, 2000.

[11] L. Baud, C. Jaussaud, R. Madar, C. Bernard, J. S. Chen, and M. A. Nicolet, “Interfacial reactions of W thin film on single-crystal (001) β-SiC,” *Mater. Sci. Eng. B*, vol. 29, no. 1–3, pp. 126–130, Jan. 1995.

[12] J. Rogowski and A. Kubiak, “Effects of annealing temperature on the structure and electrical properties of tungsten contacts to n-type silicon carbide,” *Mater. Sci. Eng. B*, vol. 191, pp. 57–65, Jan. 2015.

[13] F. Goesmann and R. Schmid-Fetzer, “Stability of W as electrical contact on 6H-SiC: phase relations and interface reactions in the ternary system W-Si-C,” *Mater. Sci. Eng. B*, vol. 34, no. 2–3, pp. 224–231, 1995.

[14] Y. K. Rao, *Stoichiometry and Thermodynamics of Metallurgical Processes*. New York: Cambridge University Press, 1985.

[15] T. C. Chou, “High temperature interfacial reactions of SiC with metals,” *J. Vac. Sci. Technol. A Vacuum, Surfaces, Film.*, vol. 9, no. 3, p. 1525, 1991.

[16] F. Goesmann and R. Schmid-Fetzer, “Metals on 6H-SiC: contact formation from the materials science point of view,” *Mater. Sci. Eng. B*, vol. 46, no. 1–3, pp. 357–362, 1997.

[17] M. R. Johan, M. S. M. Suan, N. L. Hawari, and H. A. Ching, “Annealing Effects on the Properties of Copper Oxide Thin Films Prepared by Chemical Deposition,” *Int. J. Electrochem. Sci.*, vol. 6, pp. 6094–6104, 2011.

[18] P. M. Martins, F. A. Rocha, and P. Rein, “The Influence of Impurities on the Crystal Growth Kinetics According to a Competative Adsoprtion Model,” *Cryst. Growth Des.*, vol. 6, no. 7, pp. 2814–2821, 2006.

[19] S. K. Poornachary, “Effect of Impurities on Crystal Growth Processes,” National

University of Singaphore, 2007.

[20] G. Y. Chen, V. Stolojan, D. C. Cox, C. Giusca, and S. R. P. Silva, “Growth of Tungsten Oxide Nanowires Using Simple Thermal Heating,” in *Emerging Technologies-Nanoelectronics, 2006 IEEE Conference on. IEEE, 2006.*, 2006, pp. 376–378.

[21] A. Ağıral and J. G. E. H. Gardeniers, *On-Chip Tungsten Oxide Nanowires Based Electrodes for Charge Injection*. Croatia: INTECH, 2010.

[22] Y. Li, J. P. Li, C. C. Jia, and X. Q. Liu, “Fabrication of tungsten films by metallorganic chemical vapor deposition,” *Int. J. Miner. Metall. Mater.*, vol. 19, no. 12, pp. 1149–1153, 2012.

[23] S. Xu and L. Diao, “Study of tungsten oxidation in O2:H 2:N2 downstream plasma,” *J. Vac. Sci. Technol. A Vacuum, Surfaces, Film.*, vol. 26, no. 3, p. 360, 2008.

[24] J. H. Hougen, R. R. Reeves, and G. G. Mannella, “Reduction of Tungsten Oxides with Hydrogen,” *Ind. Eng. Chem.*, vol. 48, pp. 318–320, 1956.

[25] T. T. Thabethe, T. T. Hlatshwayo, E. G. Njoroge, T. G. Nyawo, and J. B. Malherbe, “The effect of thermal annealing in a hydrogen atmosphere on tungsten deposited on 6HSiC,” *Vacuum*, vol. 129, pp. 161–165, 2016.

[26] T. T. Thabethe, E. G. Njoroge, T. T. Hlatshwayo, T. P. Ntsoane, and J. B. Malherbe, “Surface and interface structural analysis of W deposited on 6H – SiC substrates annealed in argon,” *RSC Adv.*, vol. 7, pp. 2–7, 2017.

[27] P. M. Smith and M. O. Thompson, “The Effects of N2 and Ar as the Ambient Gas During Rapid Thermal Annealing of Tungsten Silicide,” *MRS Proceedings*, vol. 100. pp. 707–712, 1988.

[28] T. T. Thabethe, T. T. Hlatshwayo, E. G. Njoroge, T. G. Nyawo, T. P. Ntsoane, and J. B. Malherbe, “Interfacial reactions and surface analysis of W thin film on 6H-SiC,”

Nucl. Instruments Methods Phys. Res. Sect. B Beam Interact. with Mater. Atoms, vol. 371, no. B, pp. 235–239, 2016.

[29] G. Z. Wulf, "On the question of speed of growth and dissolution of crystal surfaces," *Krist. Mater.*, vol. 34, p. 449, 1901.

[30] P. Bénard and R. Chahine, "Storage of hydrogen by physisorption on carbon and nanostructured materials," *Scr. Mater.*, vol. 56, no. 10, pp. 803–808, 2007.

[31] T. E. Madey, "Chemistry of hydrogen on W (100): Absolute sticking probability, coverage and electron stimulated desorption," *Surf. Sci.*, vol. 36, pp. 281–294, 1973.

[32] K. F. Poulter and J. A. Pryde, "Chemisorption of hydrogen on rhenium," *J. Appl. Phys.*, vol. 1, no. 2, pp. 169–172, 1968.

[33] W. K. Burton, N. Cabrera, and F. C. Frank, "The growth of crystal and the equilibrium structure of their surfaces," *Philos. Trans. R. Soc. A*, vol. 243A, p. 299, 1931.

[34] R. E. Hummel and K. H. Guenther, *Handbook of Optical Properties*, Volume I. New York, USA: CrC Press, 1995.

[35] C. Guo, C. Zhang, L. He, B. Jin, and N. Shi, "Microstructure Characterization of Long W Core SiC Fiber," *J. Mater. Sci. Technol.*, vol. 23, no. 5, pp. 677–684, 2007.

[36] T. Toplisek, M. Gec, A. Ivekovic, S. Novak, S. Kobe, and G. Drazic, "Analytical Electron Microscopy of W-Core b-SiC Fibers for Use in an SiC-Based Composite Material for Fusion Applications," *Microsc. Microanal.*, vol. 19, no. S5, pp. 136–139, 2013.

Chapter 8 : Conclusions and Future work

8.1 Conclusions

This study of W thin film deposited on 6H-SiC was conducted to gain more understanding of the interaction between W and SiC and the structural changes resulting from this interaction. This study is important for a vast number of technological applications which involve W and SiC in contact at elevated temperatures. In this study, W thin film was DC sputter deposited on 6H-SiC at room temperature and annealed from 700 °C to 1000 °C for 1 h. Annealing was performed in vacuum, H_2 and Ar to determine the lowest reaction temperature, to study the W and SiC interaction and structural changes. The as-deposited and annealed samples were analyzed by RBS, GIXRD, SEM and AFM.

The W thin film with a thickness of about 73.8 nm was deposited on 6H-SiC. The as-deposited sample had a mixture of tungsten and tungsten oxide in the first layer, and SiC substrate as the second layer. The RBS results indicated that the W-SiC diffusion couple was stable up to a temperature of 700 °C for vacuum and H_2 annealed samples, and at temperatures lower than 700 °C for Ar annealed samples. For the vacuum annealed samples, a reaction was observed to occur at 700 °C and proceeded after annealing at 850 °C. The Ar and H_2 annealed samples indicated a reaction between W and SiC in all the annealing temperature range (700 °C to 1000 °C). Carbon was seen to diffuse first into the W metal in the different annealing atmosphere.

Annealing in different atmospheres resulted in a variation in the RZ thicknesses with the thickness of the Ar annealed samples being thicker than those of the vacuum annealed samples, which in turn were thicker than those of the H_2 annealed samples. The RBS results

suggested that the reaction rate between W and SiC was greater for the Ar annealed samples than for the vacuum and H_2 annealed samples. W was seen to diffuse deeper in the SiC upon annealing in Ar.

XRD results indicated a polycrystalline microstructure of the as-deposited W thin film on the 6H-SiC. After 700 °C annealing in H_2, W_5Si_3 coexisted with WC as the initial phase, while CW_3 coexisted with WC as initial phases in vacuum annealing, the samples annealed in an Ar ambient had W_5Si_3, SiO_2, W_2C and WC as initial phases. The phases observed for the Argon annealed samples were the same in all the annealing temperatures. The WSi_2 and W_2C were observed to appear after annealing at 800 °C in H_2 and after annealing at 900 °C in vacuum. SiO_2 was seen in all the annealing temperatures for the Ar annealed samples, while it was only observed at 1000 °C for the H_2 annealed samples. The presence of SiO_2 in the Ar annealed samples prevented the formation of WSi_2 in the chosen annealing temperature range.

The surface morphology of the samples was characterized using SEM and AFM. The SEM image of the as-deposited film showed a fairly flat surface composed of small granules which appeared to be evenly distributed (homogeneous). The surface roughness of the as-deposited sample was 0.4 nm. The surface roughness of the samples increased with increase in annealing temperature (in vacuum, hydrogen and argon) which made the surface to become heterogonous. The H_2 annealed samples were composed of granules in a form of crystallites which were relatively small. Large crystals were formed after annealing in an Ar. Vacuum annealed samples had tungsten nanowires on the surface. The formation of different crystal sizes upon annealing in different atmospheres was explained using the step-flow model of crystal growth. Some gas atoms present in the annealing system can be physisorbed or

chemisorbed on the crystallite surfaces and in the reaction zone via cavities/opening in the layer during annealing. This will cause the crystals growth to be slow. Island formation on the surfaces (with pores between the crystals) of the Ar and vacuum annealed samples was influenced by the parasitic growth of crystallites following Wulf's law. The surface roughness of the samples after annealing in vacuum, H_2 and Ar at 700 °C was 2.26 nm, 0.833 nm and 31.6 nm, respectively. Increase in roughness was observed to take place upon annealing. Argon annealed samples were rougher than the vacuum and H_2 annealing atmosphere.

For the Ar annealed samples, a very rough surface with large crystals were observed and the oxygen was not removed but it took part in the reaction. Annealing in H_2 removed the oxide layer present, forming a surface composed of granules. Vacuum annealing slowed down the initial reaction between W and SiC and a formation of oxide nanowires were observed. Surface degradation occurred at 800 °C for vacuum and Ar annealing, while annealing in H_2 preserved the surface structure. The amount of W atoms available for reactions, determines the phases which will form. The annealing atmosphere determines the initial temperature of reaction. It was evident from the results that annealing in Ar gas reduces the initial reaction temperature. In a W-SiC system, Ar atmosphere acts a catalyst, which speeds up the reaction and causes a rough surface structure. The W-SiC samples with high oxygen content results in the formation of SiO_2 instead of WSi_2.

The results of this study show that it is better to anneal in vacuum/H_2 than in Ar when studying W-SiC contacts. In studying defects for W/SiC composite Ar annealing will be suitable. For cases where one is interested in studying the structural integrity of W-SiC one can consider annealing in different atmosphere. The ultra thin tungsten coating on SiC cannot

be used as one of the layers to protect SiC at temperatures above 700 °C, since the reaction between W and SiC is seen to take place at this temperature. The reaction between W and SiC result in the formation of grain boundaries which can influence easy escape of the FPs through the SiC. Other alternatives can be investigated, such as replacing SiC as a whole with a new material, like zirconium carbide, which will be able to operate at high temperatures (above 1000 °C). The stability of W-SiC up to 700 °C makes it good for electronic device application expected to operate at temperatures of 700 °C and below.

8.2 Future studies

For future work, further investigation need to be carried out, this involves the following:

- Cross-sectional transmission electron microscopy to examine the interface and reaction zone structure of W-SiC samples to characterize the structure.
- Conduct experiments which will focus on the structural arrangement and movement of the various species in the different layers.
- Calculate the activation energy and study the diffusion kinetic
- Study solid-state reaction of W-SiC when irradiated with Xe^{26+} swift heavy ions with fluences of 5×10^{14} at 170 MeV.
- Present a more detailed study on the reaction between W-Si-C-O by calculating the Gibbs energy of formation and draw a detailed phase diagrams.
- The effect of W thickness in phase formation.
- Conducting current-voltage characteristics to determine the ohmic character of the material.

Appendix

Nuclear Instruments and Methods in Physics Research B 371 (2016) 235–239

Contents lists available at ScienceDirect

Nuclear Instruments and Methods in Physics Research B

journal homepage: www.elsevier.com/locate/nimb

Interfacial reactions and surface analysis of W thin film on 6H-SiC

T.T. Thabethe [a,*], T.T. Hlatshwayo [a], E.G. Njoroge [a], T.G. Nyawo [b], T.P. Ntsoane [c], J.B. Malherbe [a]

[a] Department of Physics, University of Pretoria, Pretoria 0002, South Africa
[b] Department of Physics, University of Zululand, KwaDlangezwa 3886, South Africa
[c] South African Nuclear Energy Corporation SOC Limited, Pretoria 0001, South Africa

ARTICLE INFO

Article history:
Received 30 June 2015
Received in revised form 19 October 2015
Accepted 26 October 2015
Available online 4 November 2015

Keywords:
Tungsten
SiC
Interface
Reactions
Annealing

ABSTRACT

Tungsten (W) thin film was deposited on bulk single crystalline 6H SiC substrate and annealed in vacuum at temperatures ranging from 700 to 1000 °C for 1 h. The resulting solid state reactions, phase composition and surface morphology were investigated by Rutherford backscattering spectroscopy (RBS), grazing incidence X ray diffraction (GIXRD) and scanning electron microscopy (SEM). XRD was used to identify the phases present and to confirm the RBS results. The RBS spectra were simulated using the RUMP software in order to obtain the deposited layer thickness, composition of reaction zone and detect phase formation at the interface. RBS results showed that interaction between W and SiC started at 850 °C. The XRD analysis showed that WC and CW_3 were the initial phases formed at 700 and 800 °C. The concentration of the phases was however, too low to be detected by RBS analysis. At temperatures of 900 and 1000 °C, W reacted with the SiC substrate and formed a mixed layer containing a silicide phase (WSi_2) and a carbide phase (W_2C). The SEM images of the as deposited samples showed that the W thin film had a uniform surface with small grains. The W layer became heterogeneous during annealing at higher temperatures as the W granules agglomerated into island clusters at temperatures of 800 °C and higher.

Vacuum 129 (2016) 161–165

Contents lists available at ScienceDirect

Vacuum

journal homepage: www.elsevier.com/locate/vacuum

The effect of thermal annealing in a hydrogen atmosphere on tungsten deposited on 6H–SiC

T.T. Thabethe [a, *], T.T. Hlatshwayo [a], E.G. Njoroge [a], T.G. Nyawo [b], J.B. Malherbe [a]

[a] Department of Physics, University of Pretoria, Pretoria, 0002, South Africa
[b] Department of Physics, University of Zululand, KwaDlangezwa, 3886, South Africa

ARTICLE INFO

Article history:
Received 4 November 2015
Received in revised form
17 January 2016
Accepted 19 March 2016
Available online 21 March 2016

Keywords:
Tungsten
SiC
Interface
Reactions
Annealing

ABSTRACT

Tungsten (W) film was deposited on a bulk single crystalline 6H–SiC substrate and annealed in H_2 ambient at temperatures of 700 °C, 800 °C and 1000 °C for 1 h. The resulting solid state reactions, phase composition and surface morphology were investigated by Rutherford backscattering spectrometry (RBS), grazing incidence X ray diffraction (GIXRD) and scanning electron microscopy (SEM) analysis techniques. These results are compared with the vacuum annealed results reported in our earlier work. As deposited RBS results indicated the presence of W and O_2 in the deposited thin film, the GIXRD showed the presence of W, WO_3, W_5Si_3 and WC. RBS results indicated the interaction between W and SiC was accompanied by the removal of oxygen at 700 °C. The GIXRD analysis indicated the presence of W_5Si_3 and WC in the samples annealed at 700 °C. At temperatures of 800 °C and 1000 °C, W annealed in a H_2 ambient further reacted with the SiC substrate and formed a mixed layer containing silicide phases and carbide phases, i.e. W_5Si_3, WSi_2, WC and W_2C. The SEM micrographs of the as deposited samples indicated the W thin film had a uniform surface with small grains. Annealing at 800 °C led to the agglomeration of W grains into clusters making the surface rough.

RSC Advances

PAPER

Cite this: *RSC Adv.*, 2017, 7, 2

Surface and interface structural analysis of W deposited on 6H–SiC substrates annealed in argon

T. T. Thabethe,*[a] E. G. Njoroge,[a] T. T. Hlatshwayo,[a] T. P. Ntsoane[b] and J. B. Malherbe[a]

A study of a tungsten (W) thin film deposited on a single crystalline 6H–SiC substrate and annealed in Ar at temperatures of 700 °C, 800 °C, 900 °C and 1000 °C for 1 hour was conducted. The subsequent solid state reactions, phase composition and surface morphology were investigated by Rutherford backscattering spectrometry (RBS), grazing incidence X-ray diffraction (GIXRD) and scanning electron microscopy (SEM) analysis techniques. RBS analysis of as-deposited samples indicated the presence of W and oxygen in the as-deposited thin film, the GIXRD analysis of the as-deposited film showed the presence of W, WO_3, W_5Si_3 and WC. RBS results of the sample annealed at 700 °C indicated interaction between W and SiC with the formation of a reaction zone. The GIXRD analysis indicated the presence of W_5Si_3, WO_3, SiO_2, W_2C and WC in the W–SiC reaction zone (RZ) after annealing at 700 °C. At temperatures of 800 °C to 1000 °C, the W–SiC samples did not show any new phase formation from the GIXRD patterns, while the RBS results indicate an increase in the RZ width which meant further reactions were taking place. An increase in the peak intensities of the GIXRD patterns was observed due to a change in the polycrystalline nature of the W film to a more crystalline structure. SEM micrographs of the as-deposited samples indicated that the W thin film had a uniform surface with small grains. Annealing at 700 °C and above led to the formation of large crystals. The large crystals formed were randomly orientated; it was observed that an increase in annealing temperature led to an increase in the film crystal size forming pores between crystals.

Received 6th October 2016
Accepted 16th November 2016

DOI: 10.1039/c6ra24825j

www.rsc.org/advances